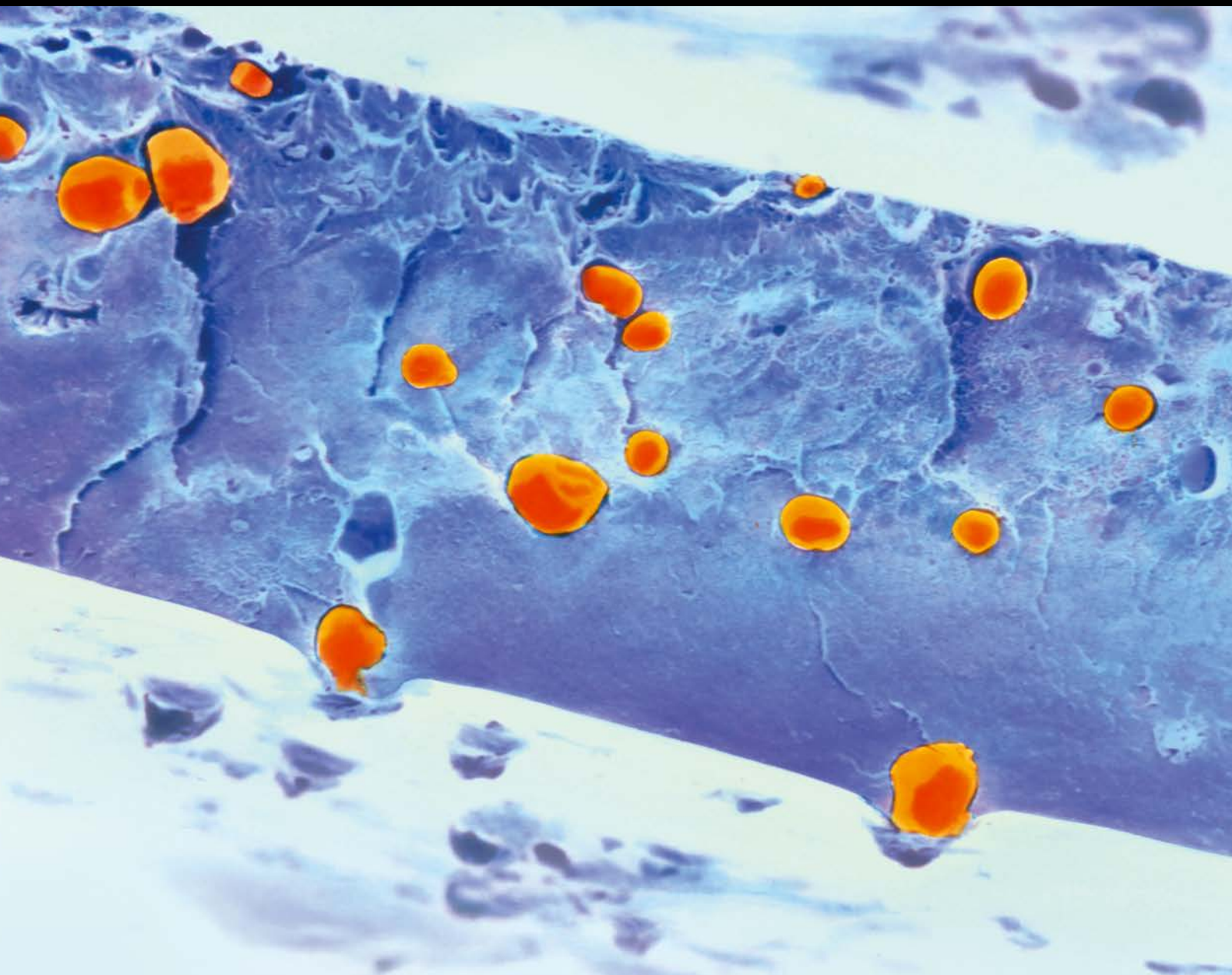


Composites and Nanocomposites Based on Renewable and Sustainable Materials

Guest Editors: Matheus Poletto, Heitor Luiz Ornaghi Júnior, P. M. Visakh, and Yoshihiko Arao





Composites and Nanocomposites Based on Renewable and Sustainable Materials

International Journal of Polymer Science

**Composites and Nanocomposites Based on
Renewable and Sustainable Materials**

Guest Editors: Matheus Poletto, Heitor Luiz Ornaghi Júnior,
P. M. Visakh, and Yoshihiko Arao



Copyright © 2016 Hindawi Publishing Corporation. All rights reserved.

This is a special issue published in "International Journal of Polymer Science." All articles are open access articles distributed under the Creative Commons Attribution License, which permits unrestricted use, distribution, and reproduction in any medium, provided the original work is properly cited.

Editorial Board

Domenico Acierno, Italy
Sharif Ahmad, India
Mats R. Andersson, Australia
Luc Averous, France
Massimiliano Barletta, Italy
Christopher Batich, USA
Giuseppe Battaglia, UK
Marc Behl, Germany
Laurent Billon, France
David G. Bucknall, USA
Andrea Camposeo, Italy
Wen Shyang Chow, Malaysia
J. deClaville Christiansen, Denmark
Yoshiki Chujo, Japan
Angel Concheiro, Spain
Marek Cypryk, Poland
Li Ming Dai, USA
Yulin Deng, USA
Maria Laura Di Lorenzo, Italy
Eliane Espuche, France
Antonio Facchetti, USA
M. Fernández-García, Spain
Benny D. Freeman, USA
Jean-François Gérard, France
Peng He, USA
Jan-Chan Huang, USA
Wei Huang, China
Nabil Ibrahim, Egypt
Tadashi Inoue, Japan
Avraam I. Isayev, USA
Koji Ishizu, Japan
Patric Jannasch, Sweden
Nobuhiro Kawatsuki, Japan
J.M. Kenny, Italy
M. A. Khan, Bangladesh
Ruhul A. Khan, Canada
Saad Khan, USA
Jui-Yang Lai, Taiwan
Jose Ramon Leiza, Spain
Guiping Ma, China
Evangelos Manias, USA
Ulrich Maschke, France
Jani Matisons, Australia
Geoffrey R. Mitchell, UK
Subrata Mondal, India
Christian Nielsen, UK
Toribio F. Otero, Spain
Qinmin Pan, Canada
Alessandro Pegoretti, Italy
Önder Pekcan, Turkey
Zhonghua Peng, USA
Beng T. Poh, Malaysia
Antje Potthast, Austria
Debora Puglia, Italy
Miriam Rafailovich, USA
Arthur J. Ragauskas, USA
Subramaniam Ramesh, Malaysia
B. Luis Rivas, Chile
J. Rodriguez-Hernandez, Spain
H. Roghani-Mamaqani, Iran
Pietro Russo, Italy
Mehdi Salami-Kalajahi, Iran
Erol Sancaktar, USA
A. P. Schenning, Netherlands
M. Schnabelrauch, Germany
Shu Seki, Japan
Vitor Sencadas, Australia
Robert A. Shanks, Australia
Mikhail Shtilman, Russia
B. Siddaramaiah, India
Dennis W. Smith Jr., USA
Atsushi Sudo, Japan
Kohji Tashiro, Japan
Hideto Tsuji, Japan
Masaki Tsuji, Japan
Stefano Turri, Italy
Hiroshi Uyama, Japan
Cornelia Vasile, Romania
Alenka Vesel, Slovenia
Y. S. Vygodskii, Russia
De-Yi Wang, Spain
Qinglin Wu, USA
Frederik Wurm, Germany
Huining Xiao, Canada
Yiqi Yang, USA
Long Yu, Australia
Philippe Zinck, France

Contents

Composites and Nanocomposites Based on Renewable and Sustainable Materials

Matheus Poletto, Heitor Luiz Ornaghi Júnior, P. M. Visakh, and Yoshihiko Arao
Volume 2016, Article ID 6475874, 2 pages

Effect of Reinforcement of Hydrophobic Grade Banana (*Musa ornata*) Bark Fiber on the Physicomechanical Properties of Isotactic Polypropylene

Md. Mamunur Rashid, Sabrin A. Samad, M. A. Gafur, Md. Rakibul Qadir,
and A. M. Sarwaruddin Chowdhury
Volume 2016, Article ID 9017956, 8 pages

Effect of Wood Fillers on the Viscoelastic and Thermophysical Properties of HDPE-Wood Composite

M. Tazi, M. S. Sukiman, F. Erchiqui, A. Imad, and T. Kanit
Volume 2016, Article ID 9032525, 6 pages

Preparation of Nanofibers with Renewable Polymers and Their Application in Wound Dressing

Ying Zhao, Yihui Qiu, Huanhuan Wang, Yu Chen, Shaohua Jin, and Shuseng Chen
Volume 2016, Article ID 4672839, 17 pages

Utilization of Waste Clay from Boron Production in Bituminous Geosynthetic Barrier (GBR-B) Production as Landfill Liner

Müfide Banar, Yücel Güney, Aysun Özkan, Zerrin Günkaya, Eren Bayrakçı, and Derya Ulutaş
Volume 2016, Article ID 1648920, 8 pages

Influence of Fiber Content on Mechanical and Morphological Properties of Woven Kenaf Reinforced PVB Film Produced Using a Hot Press Technique

Suhad D. Salman, Z. Leman, M. T. H. Sultan, M. R. Ishak, and F. Cardona
Volume 2016, Article ID 7828451, 11 pages

A Facile Approach to Evaluate Thermal Insulation Performance of Paper Cups

Yudi Kuang, Gang Chen, and Zhiqiang Fang
Volume 2015, Article ID 367962, 8 pages

Dynamics Analysis of the Melt Conveying Process in a Novel Extruder

Zan Huang
Volume 2015, Article ID 714356, 9 pages

An Investigation of the Effect of Chitosan on Isothermal Crystallization, Thermal Decomposition, and Melt Index of Biodegradable Poly(L-lactic acid)

Yan-Hua Cai and Li-Sha Zhao
Volume 2015, Article ID 296380, 5 pages

Editorial

Composites and Nanocomposites Based on Renewable and Sustainable Materials

Matheus Poletto,¹ Heitor Luiz Ornaghi Júnior,² P. M. Visakh,³ and Yoshihiko Arao⁴

¹*Centro de Ciências Exatas, da Natureza e Tecnologia, Universidade de Caxias do Sul, 95700-000 Caxias do Sul, RS, Brazil*

²*Programa de Pós-Graduação em Engenharia e Ciências dos Materiais (PGMAT), Universidade de Caxias do Sul, 95070-560 Caxias do Sul, RS, Brazil*

³*Tomsk Polytechnic University, Tomsk 634050, Russia*

⁴*Tokyo Institute of Technology, Tokyo 152-8550, Japan*

Correspondence should be addressed to Matheus Poletto; matheus.poletto@hotmail.com

Received 11 May 2016; Accepted 12 May 2016

Copyright © 2016 Matheus Poletto et al. This is an open access article distributed under the Creative Commons Attribution License, which permits unrestricted use, distribution, and reproduction in any medium, provided the original work is properly cited.

Renewable and sustainable materials are of great concern in scientific research and industry. These materials include biomass as industrial and agricultural residues and energy crops. The utilization of such materials as reinforcement or to improve specific properties in composite or nanocomposites materials is an excellent alternative. Among the advantages which can be cited are the strong ecological appeal, low cost, and higher specific mechanical properties.

Topics include the effect of the chemical treatment on the physicochemical properties of commercial polypropylene, preparation of nanofibers with renewable polymers and their application in wound dressing, use of waste clay from boron production as landfill liner, use of wood fillers in thermoplastic matrix, and thermal insulation of paper cups.

The effects of reinforcement of the treated and untreated banana bark fiber on the physicochemical properties of isotactic polypropylene were verified, and the water absorption, mechanical properties, and hardness, among other properties, were improved up to treatment. Another study includes the effect of fiber content on mechanical and morphological properties of woven kenaf reinforced PVB film produced using a hot press technique. In this study, the authors produced six different types of laminated composites and their mechanical properties were compared. The authors constated improvement of the mechanical characteristics up to 40% kenaf content ratio.

In a review study regarding preparation of nanofibers with renewable polymers and their application in wound

dressing, the authors constated that the preparation methods as well as the components influenced their overall properties.

Wood fibers also were used as reinforcement in HDPE composites. The rheological and the thermomechanical properties of composites vary according to wood filler content and temperature.

A facile approach to evaluate the thermal insulation performance of paper cups was realized by establishing a novel evaluation that includes a characterization parameter and a measurement apparatus, where the value of the temperature factor is proportional to the thickness of paper samples.

Dynamic analysis of the melt conveying process in a novel extruder as studied and the researcher concluded that the polymer melt conveying process in the vane extruder is completely different from the process in conventional screw extruders; the pressure within the chamber is influenced by the location and volume within the chamber and the dynamics of melt conveyance in a vane chamber depend mostly on pressure to overcome viscous forces.

The effect of the chitosan on isothermal crystallization, thermal decomposition, and melt index of PLLA polymer was studied. The authors concluded that chitosan acts as a nucleating agent for PLLA, affecting the initial degradation temperature and leading to higher values of melt flow index up to 3% of chitosan.

Finally, boron production waste clay was used to develop a geosynthetic barrier that can be used as an innovative impermeable liner on solid waste landfills. In this study,

waste clay generated during boron derivatives production was mixed with bitumen, bentonite, and waste tire and the mixtures were used to cover up reinforcement materials (nonwoven polyester and glass fleece). The samples were compared to commercial geomembranes and three samples were used to apply hydraulic conductivity test. Microscopy and mechanical and conductivity tests were performed and satisfactory results were found. The study allows the production of lower cost geomembranes while leading up to utilizing waste clay of 900,000 tons/year generated at boron enterprises in Turkey.

Matheus Poletto
Heitor Luiz Ornaghi Júnior
P. M. Visakh
Yoshihiko Arao

Research Article

Effect of Reinforcement of Hydrophobic Grade Banana (*Musa ornata*) Bark Fiber on the Physicomechanical Properties of Isotactic Polypropylene

Md. Mamunur Rashid,¹ Sabrin A. Samad,¹ M. A. Gafur,²
Md. Rakibul Qadir,² and A. M. Sarwaruddin Chowdhury¹

¹Department of Applied Chemistry and Chemical Engineering, Faculty of Engineering and Technology,
University of Dhaka, Dhaka 1000, Bangladesh

²Pilot Plant and Process Development Center (PP & PDC), Bangladesh Council of Scientific and Industrial Research,
Dhaka 1205, Bangladesh

Correspondence should be addressed to Sabrin A. Samad; sabrinsamad@duet.ac.bd

Received 28 December 2015; Revised 15 March 2016; Accepted 4 April 2016

Academic Editor: Matheus Poletto

Copyright © 2016 Md. Mamunur Rashid et al. This is an open access article distributed under the Creative Commons Attribution License, which permits unrestricted use, distribution, and reproduction in any medium, provided the original work is properly cited.

This research studied the physicomechanical as well as morphological properties of alkali treated (NaOH and KMnO₄) and untreated banana bark fiber (BBF) reinforced polypropylene composites. A detailed structural and morphological characterization was performed using Fourier transform infrared spectroscopy (FTIR), scanning electron microscopy (SEM), and mechanical properties testing (tensile strength, flexural strength, and microhardness). Chemical treatments improved the hydrophobic property of the fiber and it is found to be better for KMnO₄ treatment. Composites with 0, 5, 10, and 15 wt.% loadings were then compared for water uptake studies and revealed that KMnO₄ treated fiber composites absorb less water compared to others. KMnO₄ treatment with 15% fiber loading improved the tensile strength, flexural strength, and microhardness of the composites compared to raw and NaOH treated fiber loadings. TGA analysis also shows onset temperature at 400~500°C that is associated with the decomposition of the banana fibers constituents including lignin, cellulose, and hemicelluloses which suggests better thermomechanical stability. All of the values suggest that 15% KMnO₄ treated banana bark fiber (BBF)/PP composites were found to be better than those of the raw and NaOH treated ones.

1. Introduction

In recent years, the use of composite materials has increased too manyfold. The reason behind that is their versatile use, ease of preparation, eco-friendly system, improved mechanical and usable properties, and low cost. One of widely used composite materials is composed of polymeric matrix. These polymer matrixes are often reinforced with synthetic (glass fiber, carbon, and aramid) and natural fibers (sisal, jute, flax, etc.). These polymer matrix composites (PMCs) are not only used in industries, automobiles, ships, and structural applications but also proved to be advantageous for their high strength to weight ratio, ease to fabricate, complex shapes, low cost, and good resistance to corrosion and marine fouling [1, 2]. Synthetic fiber based composites

are less prone to degradation because of their high molecular mass and hydrophobic character. Natural fiber reinforced composites show few drawbacks like low strength, poor interfacial bonding, and moisture uptake compared to artificial fiber reinforced composites. Natural fibers are particularly sensitive to moisture because fiber/matrix interface is critical zone for composite long-term performance [3]. Chemical treatment is an essential processing parameter to reduce hydrophilic nature of the fibers and thus improves adhesion with the matrix. Pretreatments of fiber change its structure and surface morphology. Hydrophilic hydroxyl groups are removed from the fiber by the action of different chemicals. Significant improvements in the mechanical properties of the composites are reported by using different chemical treatments (NaOH, KMnO₄, etc.) to achieve a good adhesion

between fiber and matrix [4]. After these treatments of fibers, removal of hemicelluloses, pectin, lignin, and wax and increases in roughness of fibers were observed [4] in addition to mechanical interlocking [5]. Chemically treated fiber reinforced composites show significant improvement in mechanical properties [6]. Studies have shown that NaOH treated coir fiber had better mechanical property than sodium lauryl sulphate (SLS) treated coir fiber. In both cases the fiber was reinforced with epoxy resin [7]. Results have shown that NaOH treated sisal fiber reinforced composites showed improved tensile and flexural strength compared to untreated sisal fiber reinforced composites [8]. Permanganate treatment on natural fibers is conducted by potassium permanganate (KMnO_4) in acetone solution. This treatment enhances chemical interlocking at the interface and provides better adhesion with the matrix (Akash et al. [9]). It also reacts with the lignin (hydrophilic AOH groups) constituents and separates from the fiber cell wall which causes reduction of hydrophilic nature of the fiber [10].

In Bangladesh, banana is abundantly cultivated. Banana fiber can be easily obtained from the pseudostem after the fruits and leaves are utilized and also the bark of the plant itself. Like other natural fibers such as jute, sisal, and hemp, banana fibers have also been used as a reinforcing material. Venkateshwaran et al. [11–13] studied the mechanical properties of tensile and flexural strength and impact and water absorption tests were carried out using banana/epoxy composite material. The effect of alkali and SLS (sodium lauryl sulphate) treatment on banana/kenaf hybrid composites and woven hybrid composites was also studied.

Current research activities have shifted towards the development of “cost-performance” rather than “high-performance” thermoplastic composites. Since cost-effectiveness depends also on raw material cost, most composite systems that are considered as an attractive candidate for this “cost-performance” market are based on E-glass fibers and resins such as polypropylene (PP), polyamide-6,6 (PA-6,6), poly(ethylene terephthalate) (PET), or poly(butylene terephthalate) (PBT) [14]. Among these PP offers a number of favorable characteristics as matrix material for high volume applications of composite materials. It exhibits many beneficial properties such as low price, high toughness, low density, relatively high thermal stability, good (di) electrical properties, and chemical resistance [15]. Moreover, PP can easily be processed and recycled and is available in a large number of grades. Considering all these facts, we aimed to prepare a composite based on PP which is reinforced by chemically treated banana fiber. The aim of chemical treatment is to improve the hydrophobic character of the fiber and to afford a better reinforcement in between the fiber and hydrophobic matrix.

2. Materials and Methods

2.1. Preparation of Banana Fiber. Banana fibers were collected from the bark of banana plant of species *Musa ornata* (Sagor Kala) from Curzon Hall area. The fibers were about 30 cm long. When banana plants got matured, the bark of the plant was cut down into small pieces and separated

layers were tied up in bundles. The bundles were put under fresh water in two separate buckets for twenty days. Then compost fertilizer was mixed with the water and bundles were kept for five more days. When rotten, the barks were taken out of the bucket and washed thoroughly with water several times and dried in open air without exposure to sunlight. The removal of impurities such as dirty materials and gummy substances was carried out by immersing dry fibers in a solution of 6.5 g detergent per liter of water at 70–75°C for 30 min in a beaker. Fiber-to-solution ratio was 1:50 (by weight). They were washed thoroughly with distilled water to remove impurities and dried in an oven at 50°C for 20 min before drying in open air for 24 hrs and stored in a desiccator.

2.2. Removal of Moisture from Treated and Untreated Banana Fiber. Treated and untreated banana fibers were kept at 50°C for three hours in the oven for the removal of moisture. This was done for better sample preparation and removal of undesirable bubble in the composite. Raw BBF, 0.05% KMnO_4 treated BBF, and 7.5% NaOH treated BBF were used to prepare BBF/PP composites in different composition.

2.3. Removal of Moisture from Polypropylene. Commercial polypropylene used for the preparation of composite was isotactic and had an intermediate level of crystallinity between that of low-density polyethylene (LDPE) and that of high-density polyethylene (HDPE). The commercial isotactic PP had a melting point that ranges from 160 to 166°C. It was dried by desiccating the polymer in the furnace operated electrically at 80°C for 3 hours, for better sample preparation. Desiccating is the process of preservation by removing all water and liquids from the substance. Moisture removal of polymer was needed to make sure that the final sample was free from undesirable bubble.

2.4. Composite Pellets Preparation. PP and BBF powder were proportionately, gradually, and simultaneously poured into the hopper of an extruder set at a temperature of 170°C. The mixture then came into the contact of header and rotating shaft, where PP melted and the speed of the shaft helped to squeeze out the mixture through nozzle. Shaft speed was kept moderate to prevent the running out of the mixture. Mixing was the major part for the extrusion. If the mixing of fiber and matrix is not done homogeneously, the quality of the products obtained would be very poor. Noodles obtained through nozzles then chopped into small pellets, which were favorable for further extrusion. This process was repeated at least three times for uniform mixing.

2.5. Composite Sheet Preparation. Beads of BBF/PP composites made by chopping the extruder's nozzle discharge were taken into a mold prepared before by polishing with very fine emery paper, acetone washing, and spraying mold releaser. Then 20 g of pellet was taken into a mold placed between the two steel plates of weber-pressure hydraulic press (hot press) to make composite sheet. The temperature of the hot press was set at 170°C while the initial pressure was set at 350 KN.

TABLE 1: Composition of different composites.

Composites	Composition (wt.%)	
	PP (wt.%)	Banana fiber (wt.%)
C1	100	0
C2	95	5
C3	90	10
C4	85	15



FIGURE 1: Pellets of BBF/PP composites.

It took around 30 minutes to reach the set temperature. After reaching the set temperature, the melt was held for about 5 minutes at 100 KN pressure. Then the sheet was cooled down to below 40°C (Figures 1 and 2 and Table 1).

3. Results and Discussions

3.1. Physical Properties of Raw and Treated BBF/PP Composites. From Figure 3, it is observed that the highest value of water absorption is for 15% raw BBF/PP composites and water absorption increases with the increase of percentage of raw fiber addition. Fiber is the hydrophilic part while PP is the hydrophobic part of the composite. That is why the hydrophilicity of the composite increases with the increase of fiber percentage in the composite. The same property is also found for NaOH and KMnO_4 treated fibers. It is also found that raw BBF/PP composites absorb more water than treated BBF/PP composites. Sodium hydroxide treatment removes the hydrogen bonding in the network structure of the fibers cellulose, increasing fibers surface roughness [16]. It is due to the fact that chemical treatment causes loss of hemicellulose, lignin, and pectin of the fiber, decreasing the hydrophilicity and increasing the surface tension and roughness of the fiber, ensuring proper adhesion between matrix and fiber, and making the composite less penetrable to water [17].

3.2. Mechanical Properties of Raw and Treated BBF/PP Composites

3.2.1. Ultimate Tensile Strength (UTS) of Raw and Treated BBF/PP Composites. Tensile specimen was prepared according to ASTM D638-98. The test speed was 1 mm/min while the number of test specimens examined is 6. It is observed that UTS increases with fiber treatment and with the increase of percentage of fiber addition [16]. Chemical treatment of fiber reduces incompatibility between hydrophilic fiber and



FIGURE 2: BBF/PP composites in pressed form.

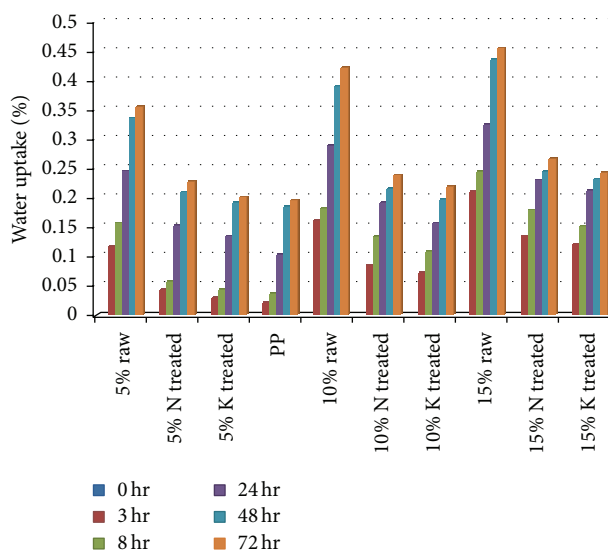


FIGURE 3: Water uptake for treated and untreated BBF/PP composites for time interval 0~72 hr.

hydrophobic PP by removing waxes and other noncellulosic substances, which brings about poor adhesion between fiber and matrix, producing rough surfaces and creating strong adhesion between matrix and fiber. With the increase of fiber addition, surface area between fiber and matrix was increased, strengthening the fiber-matrix adhesion [18]. The value of UTS for 15% KMnO_4 treated BBF/PP composite is 35.72 MPa, which is the highest. It justifies the vigor of permanganate treatment producing the rougher surface of fiber. Thus it produces better adhesion between fiber and matrix (Figure 4).

It is also observed that NaOH treated BBF/PP composites have less tensile strength with respect to KMnO_4 treated BBF/PP composites, indicating the efficiency of KMnO_4 treatment over NaOH treatment. Permanganate treatment brings about the formation of cellulose radical through Mn^{3+} ion formation. The highly reactive Mn^{3+} is responsible for initiating permanganate induced grafting [19]. However, mechanical interlocking in permanganate treatment, between the rougher fiber and the matrix, is a predominant interfacial bonding mechanism compared to that of the chemical bonding [20].

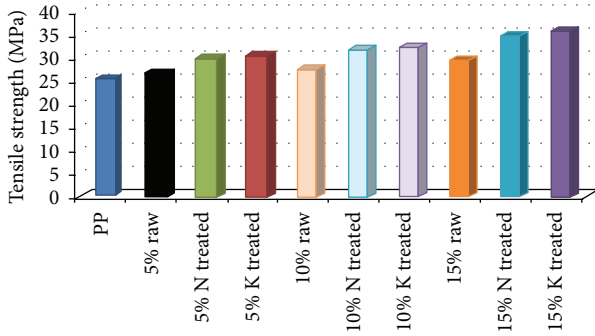


FIGURE 4: The ultimate tensile strength (UTS) of different percentages of raw and treated BBF/PP composites.

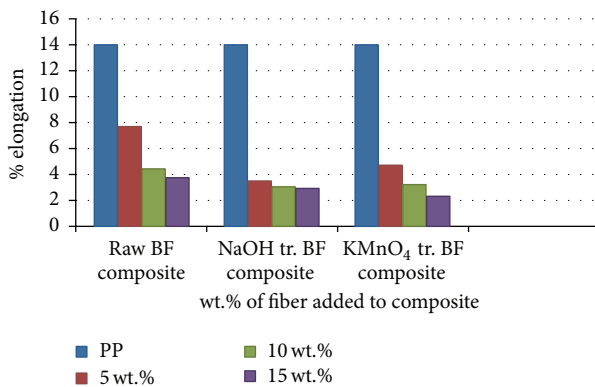


FIGURE 5: Comparison of % elongation of raw and treated BBF/PP composites.

3.2.2. Percentage Elongation of Raw and Treated BBF/PP Composites. Figure 5 shows the comparison of percentage elongation of raw and treated BBF/PP composites. It is observed that treated fiber composites have less percentage elongation than that of raw fiber reinforced composite. Chemical treatment removes lignin, hemicellulose, and other materials from the fiber. Thus roughness of the fiber surface and adhesion between matrix and fiber increased. Increased adhesion decreases ductility or increases hardness of the composites. That is why chemical treatment eventually results in less % elongation in composites. Also NaOH treated fiber composite has comparatively more elongation than that of KMnO₄ treated fiber composite. This is due to the more adhesion between fiber and matrix in KMnO₄ treated fiber composite. As KMnO₄ treatment is more vigorous than NaOH treatment, KMnO₄ treatment removes more fiber surface material and makes the surface rougher, resulting in increased adhesion. With the increase of fiber addition, adhesion between fiber and matrix also increases because of the increase of rough surface area. So % elongation decreases with fiber addition.

3.2.3. Flexural Strength of Raw and Treated BF/PP Composites. Figure 6 shows comparison of flexural strength of various percentage raw and treated BBF/PP composites. It is observed that the highest flexural strength (50 MPa) is for KMnO₄ treated 15 wt.% BBF/PP composites and the lowest flexural

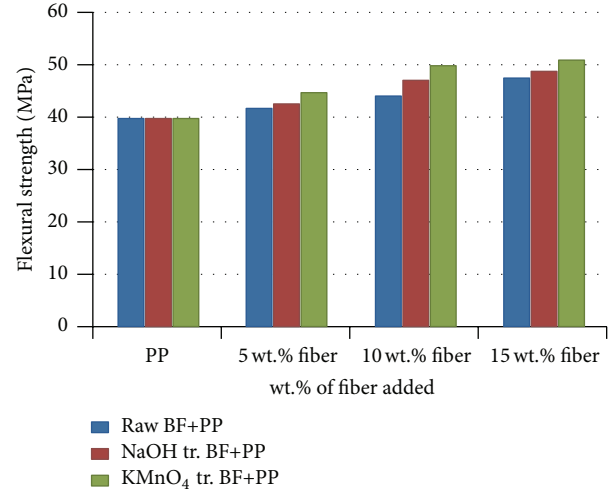


FIGURE 6: Comparison of flexural strength of different BBF/PP composites.

strength is for PP (40 MPa). Flexural strength increases with the increase of percentage of fiber addition. Goriparthi et al. [21] attributed to the fiber surface modification by both permanganate and mercerization chemical treatments for the increase of flexural strength. Because both chemical treatment and fiber content increase the adhesion forces between fiber and matrix, the highest value explains the vigor of KMnO₄ treatment.

3.3. TG Analysis of BF/PP Composites. Thermal analysis is an important and very useful method to characterize any material such as thermoplastic or thermosetting polymer matrix and also to determine the influence of natural fibers addition into the polymers [22]. Thermal analysis is used as an analytical method in understanding the structural property relationship and thermal stability of composite materials, such as the incompatibility between fibers and polymer matrixes. The majority of natural fibers have low degradation temperatures (200°C) as a function of cellulose and lignin which make them inadequate for processing temperatures above 200°C [23]. In Figure 7, S4 (red line) represents TG analysis of KMnO₄ treated 15 wt.% BF/PP composite, S1 (green line) untreated 15 wt.% BF/PP composite, and S2 (blue line) NaOH treated 15 wt.% BF/PP composite. From Figure 7, it is observable that initial drop in weight is normally attributed to the release of absorbed moisture or the vaporization of water related to the humidity from the surface of fibers. The interaction between hydrogen bonds allowed the thermal energy to be distributed over many bonds and is a major source of stability in cellulose [24]. This was correlated with the dehydration of the banana fiber. After the first constant stage, a sloping decrease in weight occurred until the onset temperature reached at 400~500°C. This sloping decrease can be associated with the decomposition of the banana fibers constituents including lignin, cellulose, and hemicelluloses. The higher onset temperature means the higher crystallinity and stability [25]. So from the figure it is

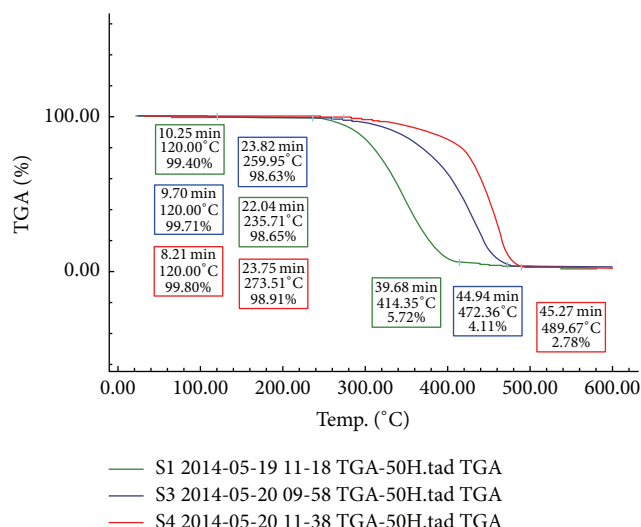


FIGURE 7: TGA analysis for different BBF/PP composites. Thermal analysis result, Center for Advanced Research in Sciences, University of Dhaka.

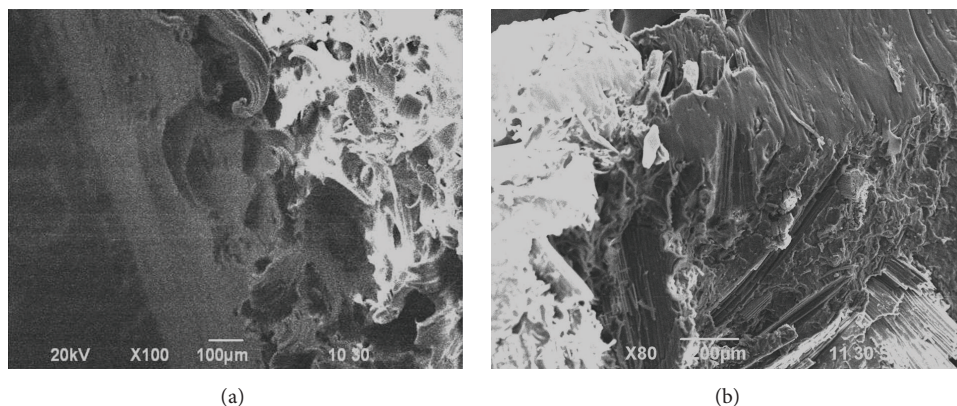


FIGURE 8: SEM images of tensile fractured surfaces of (a) NaOH treated composites and (b) untreated composites.

clear that KMnO_4 treated 15 wt.% BF/PP composite has the highest crystallinity and thermal stability. The lowest water absorption by this composite also justifies the fact.

3.4. SEM Analysis of BBF/PP Composites. SEM images of tensile fractured surfaces of untreated and NaOH treated composites are shown in Figure 8. The fractured surface of untreated banana fiber composite exhibits a large number of pullouts, indicating poor fiber-matrix adhesion. It can also be observed from Figure 8(b) that no matrix is adhered to the surface of pulled out fiber, indicating the incompatibility between matrix and fiber. On the other hand, NaOH treated composite exhibits a fiber breakage rather than pullout that indicates a strong interfacial bonding between the fiber and matrix, which in turn results in the transfer of stress between the fiber and the matrix [21].

3.5. FTIR Analysis. Figure 9(a) shows the FTIR spectrum of PP. From the figure, C-H asymmetric stretching band at 2929 cm^{-1} and C-H asymmetric deformation band at 1454 cm^{-1} for CH_2 and CH_3 group, respectively, and C-C

absorption band at $1200\sim 1000\text{ cm}^{-1}$ for carbon chain are observed. Figure 9(b) shows the FTIR spectrum of 15% raw BBF/PP composite. From the figure, it can be noted that there is an absorption peak at 3340 cm^{-1} indicating O-H stretching absorption band. Here, C-H asymmetric stretching band at 2927 cm^{-1} and C-H asymmetric deformation band at 1452 cm^{-1} for CH_2 and CH_3 group, respectively, C=C stretching band at 1641 cm^{-1} , C-O absorption band at 1226 cm^{-1} for ether group and C-O absorption band at 1035 cm^{-1} for primary hydroxyl group, and C-C absorption band at $1200\sim 1000\text{ cm}^{-1}$ for carbon chain are observed.

Figures 10(a) and 10(b) show the FTIR spectrum of 15% treated BF/PP composites. From the figure, it can be noted that there is an absorption peak at 3307 cm^{-1} , which indicates O-H stretching absorption band. Here, C-H asymmetric stretching band at 2927 cm^{-1} and C-H asymmetric deformation band at 1450 cm^{-1} for CH_2 and CH_3 group, respectively, C=C stretching band at 1641 cm^{-1} , C-O absorption band at 1224 cm^{-1} for ether group, and C-C absorption band at $1200\sim 1000\text{ cm}^{-1}$ for carbon chain are seen. Sgriccia et al. [26]

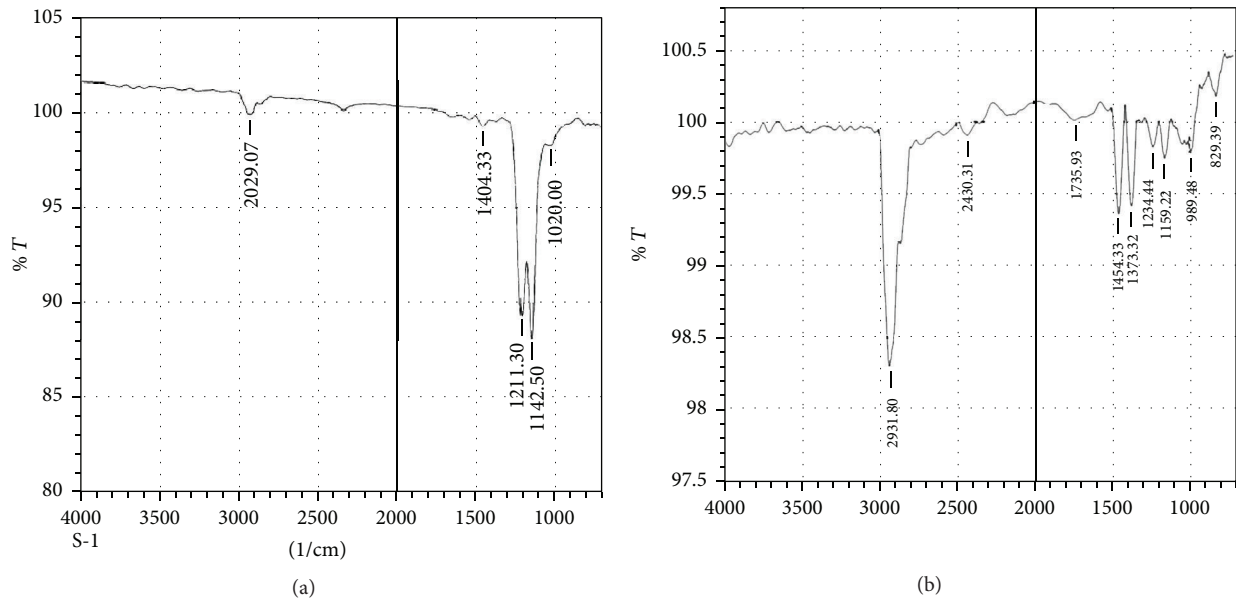


FIGURE 9: (a) FTIR spectrum of PP and (b) FTIR spectrum of 15% raw BBF/PP composite.

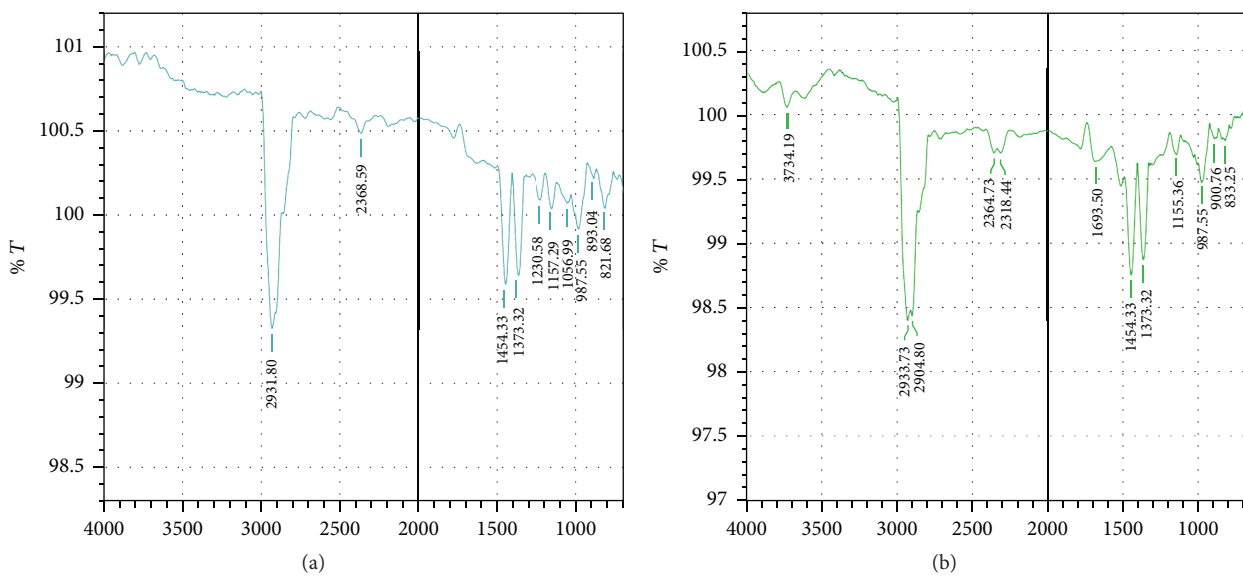


FIGURE 10: (a) FTIR spectrum of 15% NaOH treated BF/PP and (b) 15% KMnO_4 treated BBF/PP composites.

studied the effects of NaOH fiber treatment on the natural fiber surfaces using FTIR. They attributed the disappearance of C=O stretching of the acetyl group of hemicellulose to the removal of hemicellulose from the fiber surfaces. From Figure 9(b), it can be seen that 1735 cm^{-1} peak for C=O stretching of the acetyl group of hemicellulose is present in raw banana fiber [27, 28]. But from Figures 10(a) and 10(b) this is evident that this peak is disappeared from both alkali and KMnO_4 treated BBF/PP composite samples, which proves that both fiber treatments cause the removal of hemicellulose [28]. Again, 1234 cm^{-1} peak for C=O stretching of the acetyl group of lignin is not present in the KMnO_4 treated BBF/PP composite sample (Figure 10(b)), which means that KMnO_4 treatment removes lignin from the fiber.

But this peak is reduced to 1230 cm^{-1} and is less intense in case of alkali treated BBF/PP composite sample, which means that alkali treatment partially removed lignin from the fiber [28].

4. Conclusions

In this study, we have prepared composites using treated and untreated banana fibers with commercial PP as a matrix. The water uptake studies reveal that 5% KMnO_4 treated fiber composites absorb less water compared to others. The mechanical property of KMnO_4 treated composite appears to be better in terms of ultimate tensile strength (25 MPa), flexural strength (50 MPa), and microhardness. TGA analysis

shows onset temperature at 400~500°C that can be associated with the decomposition of the banana fibers constituents including lignin, cellulose, and hemicelluloses. In conclusion, chemically treated banana bark fiber (BBF) has the capability to improve the composite properties, which is attributed to better hydrophobic character accompanied with better mechanical properties as well as less water adsorption for the fiber reinforced commercial PP composite.

Competing Interests

The authors declare that they have no competing interests.

References

- [1] L. Yan, N. Chouw, and K. Jayaraman, "Flax fibre and its composites—a review," *Composites Part B: Engineering*, vol. 56, pp. 296–317, 2014.
- [2] I. Pillin, A. Kervoelen, A. Bourmaud, J. Goimard, N. Montrelay, and C. Baley, "Could oleaginous flax fibers be used as reinforcement for polymers?" *Industrial Crops and Products*, vol. 34, no. 3, pp. 1556–1563, 2011.
- [3] A. Le Duigou, P. Davies, and C. Baley, "Exploring durability of interfaces in flax fibre/epoxy micro-composites," *Composites Part A: Applied Science and Manufacturing*, vol. 48, no. 1, pp. 121–128, 2013.
- [4] M. M. Kabir, H. Wang, K. T. Lau, and F. Cardona, "Chemical treatments on plant-based natural fibre reinforced polymer composites: an overview," *Composites Part B: Engineering*, vol. 43, no. 7, pp. 2883–2892, 2012.
- [5] Y. Li, K. L. Pickering, and R. L. Farrell, "Analysis of green hemp fibre reinforced composites using bag retting and white rot fungal treatments," *Industrial Crops and Products*, vol. 29, no. 2-3, pp. 420–426, 2009.
- [6] D. Sedan, C. Pagnoux, A. Smith, and T. Chotard, "Mechanical properties of hemp fibre reinforced cement: influence of the fibre/matrix interaction," *Journal of the European Ceramic Society*, vol. 28, no. 1, pp. 183–192, 2008.
- [7] A. Karthikeyan, K. Balamurugan, and A. Kalpana, "The new approach to improve the impact property of coconut fiber reinforced epoxy composites using sodium lauryl sulfate treatment," *Journal of Scientific & Industrial Research*, vol. 72, no. 2, pp. 132–136, 2013.
- [8] P. Noorunnisa Khanam, H. P. S. Abdul Khalil, G. Ramachandra Reddy, and S. Venkata Naidu, "Tensile, flexural and chemical resistance properties of sisal fibre reinforced polymer composites: effect of fibre surface treatment," *Journal of Polymers and the Environment*, vol. 19, no. 1, pp. 115–119, 2011.
- [9] V. G. Akash, K. V. SreenivasRao, C. B. Prasad, and Prabilsonkhadka, "Comparative evaluation of mechanical and water absorption properties of pure epoxy resin, coir fiber/epoxy resin and hemp fiber/epoxy resin composite," *International Journal of Applied Engineering Research*, vol. 10, no. 55, 2015.
- [10] X. Li, L. G. Tabil, and S. Panigrahi, "Chemical treatments of natural fiber for use in natural fiber-reinforced composites: a review," *Journal of Polymers and the Environment*, vol. 15, no. 1, pp. 25–33, 2007.
- [11] N. Venkateshwaran, A. ElayaPerumal, and M. Jagatheeshwaran, "Effect of fiber length and fiber content on mechanical properties of banana fiber/epoxy composite," *Journal of Reinforced Plastics and Composites*, vol. 30, no. 19, pp. 1621–1627, 2011.
- [12] N. Venkateshwaran, A. ElayaPerumal, A. Alavudeen, and M. Thiruchitrambalam, "Mechanical and water absorption behaviour of banana/sisal reinforced hybrid composites," *Materials and Design*, vol. 32, no. 7, pp. 4017–4021, 2011.
- [13] N. Venkateshwaran and A. Elayaperumal, "Banana fiber reinforced polymer composites—a review," *Journal of Reinforced Plastics and Composites*, vol. 29, no. 15, pp. 2387–2396, 2010.
- [14] S. K. Garkhail, *Composites based on natural fibres and thermoplastic matrices [Ph.D. dissertation]*, University of London, London, UK, 2002.
- [15] O. Faruk, A. K. Bledzki, H.-P. Fink, and M. Sain, "Progress report on natural fiber reinforced composites," *Macromolecular Materials and Engineering*, vol. 299, no. 1, pp. 9–26, 2014.
- [16] B.-H. Lee, H.-J. Kim, and W.-R. Yu, "Fabrication of long and discontinuous natural fiber reinforced polypropylene biocomposites and their mechanical properties," *Fibers and Polymers*, vol. 10, no. 1, pp. 83–90, 2009.
- [17] O. Faruk, A. K. Bledzki, H.-P. Fink, and M. Sain, "Biocomposites reinforced with natural fibers: 2000–2010," *Progress in Polymer Science*, vol. 37, no. 11, pp. 1552–1596, 2012.
- [18] H. Ku, H. Wang, N. Pattarachaiyakooop, and M. Trada, "A review on the tensile properties of natural fiber reinforced polymer composites," *Composites Part B: Engineering*, vol. 42, no. 4, pp. 856–873, 2011.
- [19] M. A. Khan, M. M. Hassan, R. Taslima, and A. I. Mustafa, "Role of pretreatment with potassium permanganate and urea on mechanical and degradable properties of photo cured coir fiber with 1, 6 hexanediol diacrylate," *Journal of Applied Polymer Science*, vol. 100, pp. 4361–4368, 2006.
- [20] Y. Li, C. Hu, and Y. Yu, "Interfacial studies of sisal fiber reinforced high density polyethylene (HDPE) composites," *Composites Part A: Applied Science and Manufacturing*, vol. 39, no. 4, pp. 570–578, 2008.
- [21] B. K. Goriparthi, K. N. S. Suman, and N. Mohan Rao, "Effect of fiber surface treatments on mechanical and abrasive wear performance of polylactide/jute composites," *Composites Part A: Applied Science and Manufacturing*, vol. 43, no. 10, pp. 1800–1808, 2012.
- [22] S. M. Luz, J. Del Tio, G. J. M. Rocha, A. R. Gonçalves, and A. P. Del'Arco Jr., "Cellulose and cellulignin from sugarcane bagasse reinforced polypropylene composites: effect of acetylation on mechanical and thermal properties," *Composites Part A: Applied Science and Manufacturing*, vol. 39, no. 9, pp. 1362–1369, 2008.
- [23] M. Pracella, D. Chionna, I. Anguillesi, Z. Kulinski, and E. Piorkowska, "Functionalization, compatibilization and properties of polypropylene composites with Hemp fibres," *Composites Science and Technology*, vol. 66, no. 13, pp. 2218–2230, 2006.
- [24] A. K. Bledzki, A. A. Mamun, A. Jaszkievicz, and K. Erdmann, "Polypropylene composites with enzyme modified abaca fibre," *Composites Science and Technology*, vol. 70, no. 5, pp. 854–860, 2010.
- [25] M. P. Sepe, "Thermal analysis of polymers," *Rapra Review Reports*, vol. 8, no. 11, p. 17, 1997, Report 95.
- [26] N. Sgriccia, M. C. Hawley, and M. Misra, "Characterization of natural fiber surfaces and natural fiber composites," *Composites Part A: Applied Science and Manufacturing*, vol. 39, no. 10, pp. 1632–1637, 2008.
- [27] J. Biagiotti, D. Puglia, L. Torre et al., "A systematic investigation on the influence of the chemical treatment of natural fibers on

the properties of their polymer matrix composites," *Polymer Composites*, vol. 25, no. 5, pp. 470–479, 2004.

- [28] W. Liu, A. K. Mohanty, L. T. Drzal, P. Askel, and M. Misra, "Effects of alkali treatment on the structure, morphology and thermal properties of native grass fibers as reinforcements for polymer matrix composites," *Journal of Materials Science*, vol. 39, no. 3, pp. 1051–1054, 2004.

Research Article

Effect of Wood Fillers on the Viscoelastic and Thermophysical Properties of HDPE-Wood Composite

M. Tazi,¹ M. S. Sukiman,² F. Erchiqui,^{1,3} A. Imad,² and T. Kanit²

¹Department of Applied Science, University of Quebec in Chicoutimi, Chicoutimi, QC, Canada G7H 2B1

²Laboratoire de Mécanique de Lille, Université de Lille 1, Villeneuve d'Ascq Cedex, France

³Laboratory of Plasturgy and Nanotechnology, University of Quebec in Abitibi-Témiscamingue, Rouyn-Noranda, QC, Canada J9X 6V6

Correspondence should be addressed to F. Erchiqui; fouad.erchiqui@uqat.ca

Received 4 November 2015; Accepted 3 February 2016

Academic Editor: Matheus Poletto

Copyright © 2016 M. Tazi et al. This is an open access article distributed under the Creative Commons Attribution License, which permits unrestricted use, distribution, and reproduction in any medium, provided the original work is properly cited.

Wood polymer composites (WPC) have well proven their applicability in several fields of the plasturgy sector, due to their aesthetics and low maintenance costs. However, for plasturgy applications, the characterization of viscoelastic behavior and thermomechanical and thermophysical properties of WPC with the temperature and wood filler contents is essential. Therefore, the processability of polymer composites made up with different percentage of wood particles needs a better understanding of materials behaviors in accordance with temperature and wood particles contents. To this end, a numerical analysis of the viscoelastic, mechanical, and thermophysical properties of composite composed of high density polyethylene (HDPE) reinforced with soft wood particles is evaluated.

1. Introduction

Nowadays, due to the environmental and economic concerns, many research activities are directed towards the development of new composites based on thermoplastic matrices with plants (or their residues) reinforcement [1]. Reinforcement of composites with natural fillers has several advantages in comparison to mineral fillers including lower density, being inexpensive, and being nonabrasive. In fact, high cellulose component of natural fillers makes them easily biodegradable and recyclable. Also, cellulose fillers possess a crystalline structure which plays a positive role in the composite reinforcement. As a consequence many researchers are interested in the development of new techniques for extraction and modification of cellulose fillers from bioresources [2–4].

In addition, cellulose has a reactive functionality that can react with coupling agents thus enhancing adhesion between the fiber and matrix [5]. Studies have also shown that the mechanical properties of composites are highly depending on the interaction between the thermoplastic matrix and

distribution of loaded fillers [6]. While this interaction is well established, the loading force will be transferred from matrix to fillers more effectively.

On the other hand, the majority of modeling and simulating work of these biocomposites for their processing assumes constant thermal parameters of the materials, such as density and heat conductivity, or they do not take into account the special temperature dependency of the specific heat due to melting process. This is because the temperature dependence of these material parameters for biocomposites is not understood sufficiently so far. Since the rheological and deformation behaviors are strongly connected with the thermal behavior, it became obvious that these issues affect directly the accuracy of any simulation or modeling result.

In this regard, this work attempts to investigate, for thermoforming application, the process ability of composites made up of wood and a matrix of thermoplastic for six different proportions of wood fillers. To this end, a numerical analysis of the viscoelastic, thermomechanical, and thermophysical properties of composite composed of high density



FIGURE 1: Pellets (a) and compression molded samples (b) of wood polymer composites.

TABLE 1: Average geometrical dimensions of fillers.

Area (mm ²)	Long axis (mm)	Short axis (mm)	Shape ratio (L/D)
0.1154	0.574	0.302	1.97

polyethylene (HDPE) reinforced with soft wood particles is evaluated.

2. Materials and Methods

2.1. Materials. The sawdust used in this study was supplied by Tembec sawmill located in Béarn (QC, Canada). It consists of 65% of white spruce (*Picea glauca*), 20% of black spruce (*Picea mariana*), and 15% of balsam fir (*Abies balsamea*). The particle size analysis of the sawdust is performed on more than 5000 particles using the apparatus FQA (Fiber Quality Analyser, Optest Equipment, Hawkesbury, Ontario). Table 1 shows the average geometry of sawdust. Wood flour was sieved to a diameter less than 700 microns ($\phi < 0.7$ mm). The polymer matrix is a high density polyethylene (Sclair A59), with the melting temperature of 138°C and density of 980 kg/m³. The coupling agent is Fusabond 226 from Dupont, which is a polyethylene grafted with maleic anhydride (melting temperature 120°C, melt flow index (MFI) of 1.5 g/10 min, under condition 190°C, 2.16 kg). The used amount of coupling agent is 3% of total weight of composite. This amount is well known to improve the homogeneity of the mixture ensuring better distribution of fibers in the polymer matrix [7, 8]. The sieved sawdust was previously dried under temperature of 105°C for 24 hours and stored in polyethylene bags. The residual moisture content in wood used for samples preparation is estimated by a second drying of 120°C for 24 h. The wood humidity amount calculated from the mass of sawdust before and after drying was found less than 3% wt.

2.2. Methods. The composite samples were prepared using a twin-screw counter-mixer (Haake Rheometrix with roller

rotors) with angular speed of 90 rpm at the temperature of 170°C. In fact, this temperature is lower than wood fibers degradation temperature (200°C) [9]. To prepare the composite material, first of all, Sclair A59 (HDPE polymer) and Fusabond (coupling agent) were mixed for 2 minutes in order to insure complete melting of the materials. Then, sawdust was added to the mixture and blended for 5 minutes. Six different sawdust proportions were investigated including 0 wt%, 20 wt%, 30 wt%, 40 wt%, 50 wt%, and 60 wt% and the total mass of composite in mixing chamber is 148 g. In the next step, flat disc samples were prepared by compression molding using a hot press at the temperature of 150°C (above melting temperature of the polymer, 138°C) with aluminum mold plates. In order to make sure the mixture is softened properly, a preload was first applied for two minutes. This preload is also beneficial for removing possible accumulated air in the material. Then, loading on the material was continued up to 8 MPa for 4 minutes to give the final circular shape of the samples with 20 mm diameter and 4 mm thickness (Figure 1).

3. Viscoelastic Characterization of Biocomposites

3.1. Constitutive Equation. The material deformation mechanisms that occur in plasturgy can be classified into two types: linear material response and nonlinearities due to large deformations. The linear properties refer to elastic modulus, viscosity, and deformation memory while the nonlinear part refers to damping due to large deformations.

Integral type viscoelastic models relate the true stress to strain history. These models are more appropriate for representing polymers at the semisolid or molten state. The Lodge model [10] has been developed for representing the viscoelastic deformation of viscoelastic polymers. For example, it can be used for the thermoforming of semisolid materials [1] or injection for molten state [10].

To handle the behavior of isotropic thermoplastic composite, we apply the Lodge constitutive model [10]. For this

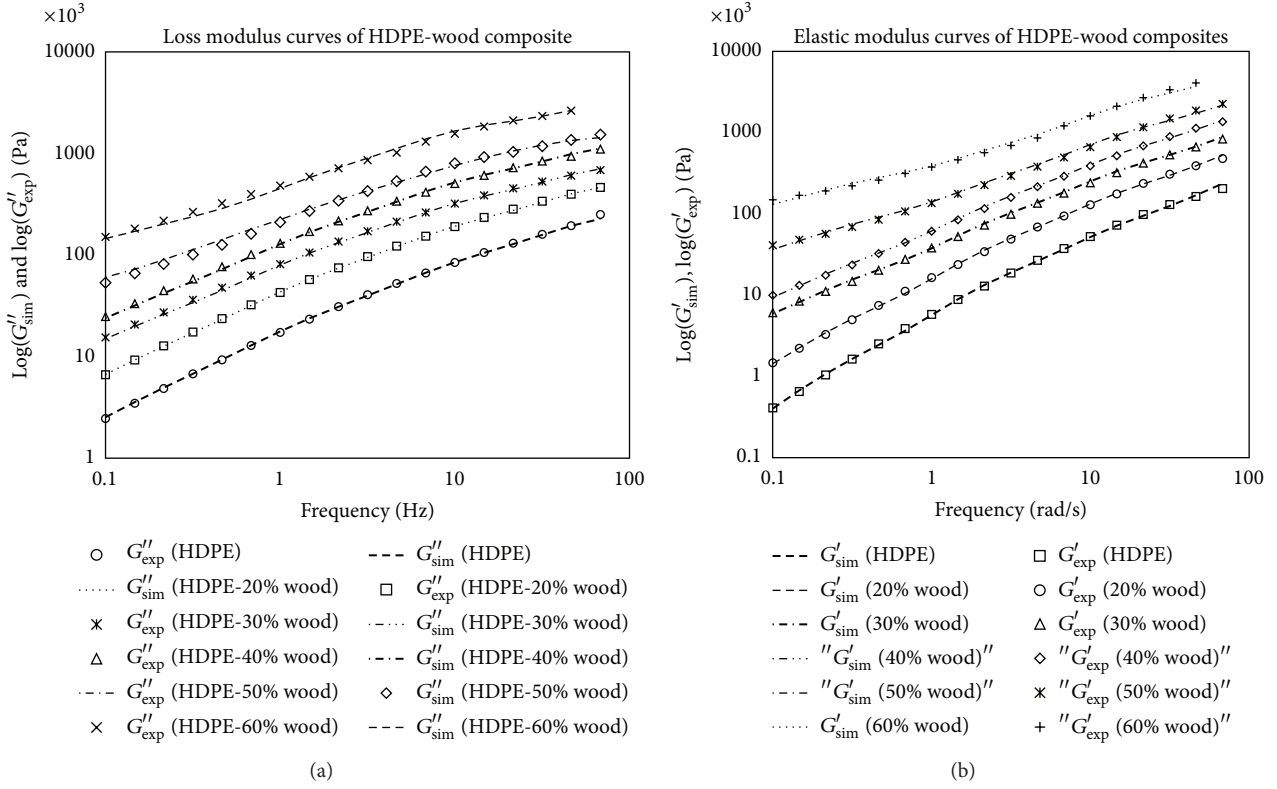


FIGURE 2: Dynamic modulus (loss modulus (a) and elastic modulus (b)) of WPC composites with different concentration of wood fillers at $T = 170^\circ\text{C}$.

model, the Cauchy stress tensor $\sigma(\mathbf{t})$ is related, at time \mathbf{t} , to the history of the Finger deformation tensor $\mathbf{B}(\tau, \mathbf{t})$ by

$$\sigma(\mathbf{t}) = -p(\mathbf{t}) \mathbf{I} + \int_0^{\mathbf{t}} \sum_k \frac{g_k}{\tau_k} e^{-(\mathbf{t}-\tau)/\tau_k} \frac{\partial \mathbf{B}(\tau, \mathbf{t})}{\partial \tau} d\tau, \quad (1)$$

where the Finger tensor \mathbf{B} is related to the right Cauchy-Green deformation tensor \mathbf{C} :

$$\mathbf{B} = \mathbf{C}^{-1} = (\mathbf{F}^T \mathbf{F})^{-1}. \quad (2)$$

\mathbf{F} is the deformation gradient tensor, p is the hydrostatic pressure, and g_k and τ_k represent, respectively, the stiffness moduli and the relaxation time. The dependency of these models on temperature is accounted for by using the WLF function [11].

3.2. Characterization Techniques. The determination of material constants requires the use of different characterization techniques. The linear properties can be obtained from small amplitude oscillatory shear test [12, 13]. This technique is used to determine the storage and loss moduli of the six composites (Figure 2). Data were collected at different flours percentage, in the Sclair A59 matrix, of 0%, 20%, 30%, 40%, 50%, and 60%. As shown, good superposition is obtained. The dynamic moduli curves for six composites have very different shapes but shifted in frequency.

From the dynamic data, the discrete relaxation spectra for six composites were determined employing a pattern search method which minimizes the objective function, F , defined:

$$F = \sum_{i=1}^N \left[\frac{G'_{i,\text{exp}} - G'_{i,\text{fit}}}{G'_{i,\text{exp}}} \right]^2 + \left[\frac{G''_{i,\text{exp}} - G''_{i,\text{fit}}}{G''_{i,\text{exp}}} \right]^2, \quad (3)$$

where N is the number of data points, $(G'_{i,\text{exp}}, G''_{i,\text{exp}})$ is available from the dynamic experiments, and $(G'_{i,\text{fit}}, G''_{i,\text{fit}})$ denotes the best fit values on the basis of equations:

$$G'(\omega) = \sum_{i=1}^N \frac{g_i \lambda_i^2 \omega^2}{1 + \lambda_i^2 \omega^2}, \quad (4)$$

$$G''(\omega) = \sum_{i=1}^N \frac{g_i \lambda_i \omega}{1 + \lambda_i^2 \omega^2}.$$

The low-frequency behavior is dominated by the long relaxation times and the high-frequency response is controlled by the short relaxation times.

This representation makes it possible to describe the linear viscoelastic behavior over a wide range of time values by means of only a few constants. The relaxation strengths g_k , which represent the contribution to rigidity associated with relaxation times τ_k , are listed in Table 2.

TABLE 2: Relaxation spectrum at 170°C for WPC.

% wood fillers	0 wt%	20 wt%	30 wt%	40 wt%	50 wt%	60 wt%
τ_k , sec	g_k , MPa					
0.001	0.181	0.3314	0.4649	0.6811	1.1246	1.1286
0.01	0.0635	0.1219	0.1769	0.2605	0.4343	0.4987
0.1	0.0298	0.0655	0.1083	0.1696	0.2596	0.4685
1	0.011	0.0302	0.0566	0.1029	0.1249	0.3276
10	0.0033	0.015	0.0344	0.061	0.1166	0.3178

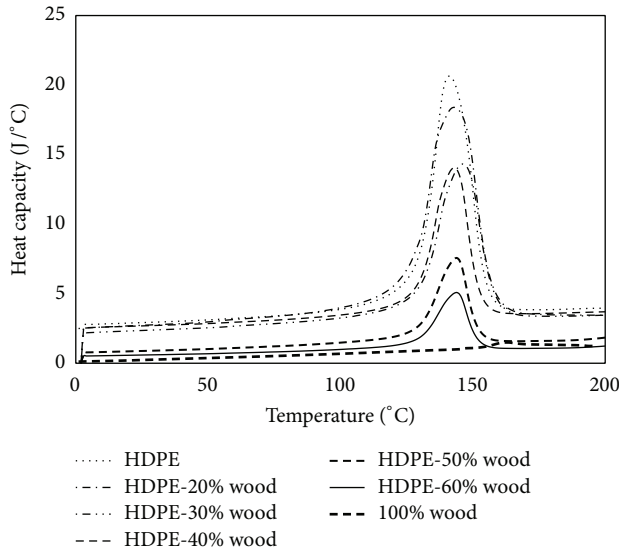


FIGURE 3: Change of heat capacity of HDPE-wood composite as function of temperature.

4. Measurement of Heat Capacity and Specific Volume as Functions of Fillers Contents and Temperature

4.1. Heat Capacity. Data curves of DSC analyses were used to evaluate the heat capacity of biocomposites. In Figure 3 we show the variation of specific heat capacity of the biocomposites with different fillers content as a function of temperature. We noticed that, during the melting phase, the variation of this parameter (ΔC_p) of HDPE-wood composites decreased compared to the matrix, for polyethylene is estimated to value 14.36 J/g·°C and for HDPE-60% wood fillers are equal to 6.7 J/g·°C as shown in Figure 3. It could be interpreted in the ways that the wood fillers act as a hindrance of molecular chains mobility close to melting temperature. These results are similar to those reported in many studies on natural fillers polymers composites. Bendahou and coauthors have investigated the effect of filler content and coupling agent on physical properties of short palm tree fibers polyolefin composites [13]. They report a slight increase of melting temperature independently of the percentage of natural fillers and also a considerable improvement in the structural arrangement of the polymers when the concentration of reinforcements increases. According to the authors the natural

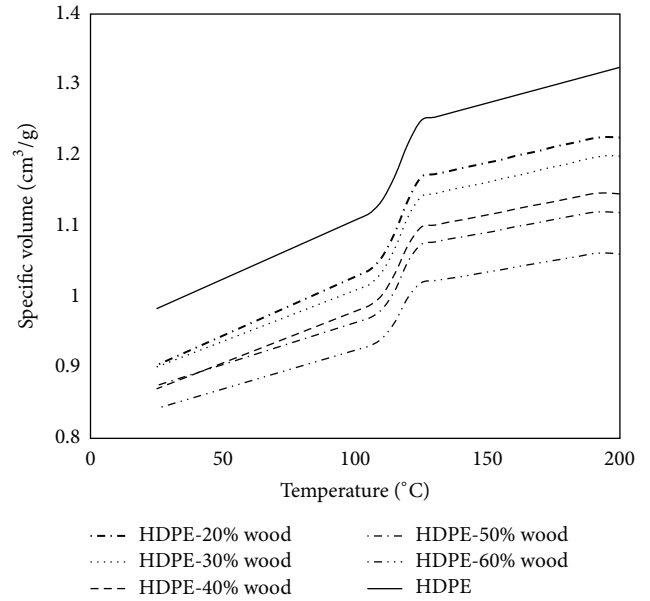


FIGURE 4: Specific volume variation as a function of filler contents.

fibers in the polymers act as nucleation site promoting a high degree of crystallinity of the polymer chains around the fibers.

4.2. Specific Volume. High temperature gradient accumulated in biocomposite during shaping process leads to a high residual stresses. This residual stress results generally in geometric instability of material. Specific volume changes of the biocomposites can be used as an index to prevent geometric instability through the processing. Also numerical simulation of composite behavior, based on temperature, requires an accurate description of specific volume changes of biocomposite as a function of temperature. In this regard, we study the variation of specific volume changes as function of temperature and filler content. It is visible from Figure 4 that the specific volume increases with the temperature and decreases while the wood fillers increase. The maximum change takes place during the melting phase of polymer at a transition temperature range of about 100 up to 130°C. This is mainly due to crystallinity effects at this stage. Also, in cases of composites with high contents, the density of wood particles per unit volume increases and the level of interaction between wood particles became also important.

TABLE 3: Linear regression of specific capacity according to the temperature and wood fillers.

Composites	$C_p - C_{p_0} = a \cdot T$ $0 < T < 80^\circ\text{C}$			$C_p - C_{p_1} = \frac{A}{\omega\sqrt{\pi/2}} \cdot \exp^{-2(T-T_m)^2/(\omega)^2}$ $81^\circ\text{C} < T < 200^\circ\text{C}$				
	C_{p_0}	$a \cdot 10^4$	R^2	C_{p_1}	T_m	A	ω	R^2
HDPE	2.73	89	98	4.02	138.80	283.5	13.53	0.99
HDPE-20% wood	2.45	116	98	3.81	140.98	315.5	16.79	0.98
HDPE-30% wood	2.52	77	99	3.43	141.72	205.6	14.97	0.98
HDPE-40% wood	2.16	93	99	3.64	138.64	161.9	12.40	0.98
HDPE-50% wood	0.75	62	99	1.64	139.06	83.76	11.58	0.97
HDPE-60% wood	0.50	42	99	1.10	139.06	56.19	11.58	0.97

TABLE 4: Linear regression of specific volume according to the temperature and wood fillers.

Composites	$\vartheta = A_2 + \frac{(A_1 - A_2)}{1 + \exp^{(T-T_0)/dT}}$ $20 < T < 130$					$\vartheta - \vartheta_0 = a \cdot T$ $131 < T < 200$		
	A_1	A_2	T_0	dT	R^2	ϑ_0	$a \cdot 10^4$	R^2
HDPE	0.97	80	302	31	0.98	1.12	10.10	0.99
HDPE-20% wood	0.89	79	302	31	0.98	1.06	8.05	0.99
HDPE-30% wood	0.89	61	284	29	0.98	1.04	8.11	0.98
HDPE-40% wood	0.85	62	303	32	0.98	1.01	6.92	0.98
HDPE-50% wood	0.86	79	292	28	0.98	0.99	6.53	0.98
HDPE-60% wood	0.83	65	300	29	0.98	0.94	1.91	0.98

4.3. *Mathematical Representation of Thermophysical Properties.* For the purpose of processing modeling and numerical simulation, it is essential to have mathematical expressions of thermophysical properties of polymer based composites. Hence, in order to have analytical representations of heat capacity and specific volume based on the temperature and wood filler content, some obtained experimental data were used. In this case, based on a regression analysis the temperature region was divided into two different regions (inside and outside of the transition zone). The equations in the tables represent the best estimates of the measured experimental data. The values of the required regression parameters are listed in Table 3 for heat capacity and in Table 4 for specific volume.

5. Conclusion

Wood polymer composites (WPC) have well proven their applicability in several fields of the platurgy sector, due to their aesthetics and low maintenance costs. However, for platurgy applications, the processability of polymer composites made up with different percentage of wood particles needs a better understanding of materials behaviors in accordance with temperature and wood particles contents. In this regard, we attempt in this work to perform a characterization of viscoelastic, rheological, and thermophysical properties of WPC.

Our results indicate that the rheological and the thermo-mechanical properties of composites vary according to wood fillers content and temperature. Composites behavior became

more elastic than viscous while wood particles percentage increases.

Also, thermophysical properties of composites (specific heat capacity and specific volume) change as function of temperature and filler content. The maximum variations take place during the melting phase of polymer. A mathematical representation of the variation of thermophysical parameters according to temperature and wood fillers is performed. This allowed us to predict the thermophysical behavior of composite at temperatures and wood fillers where it is difficult to measure experimentally.

Competing Interests

The authors declare that they have no competing interests.

References

- [1] F. Erchiqui, F. Godard, A. Gakwaya, A. Koubaa, M. Vincent, and H. Kaddami, "Engineering investigations on the potentiality of the thermoformability of HDPE charged by wood flours in the thermoforming part," *Polymer Engineering and Science*, vol. 49, no. 8, pp. 1594–1602, 2009.
- [2] A. Bendahou, Y. Habibi, H. Kaddami, and A. Dufresne, "Physico-chemical characterization of palm from *Phoenix Dactylifera*-L, preparation of cellulose whiskers and natural rubber-based nanocomposites," *Journal of Biobased Materials and Bioenergy*, vol. 3, no. 1, pp. 81–90, 2009.
- [3] A. K. Bledzki and O. Faruk, "Wood fibre reinforced polypropylene composites: effect of fibre geometry and coupling agent on

- physico-mechanical properties,” *Applied Composite Materials*, vol. 10, no. 6, pp. 365–379, 2003.
- [4] H. Kaddami, A. Dufresne, B. Khelifi et al., “Short palm tree fibers—thermoset matrices composites,” *Composites Part A: Applied Science and Manufacturing*, vol. 37, no. 9, pp. 1413–1422, 2006.
- [5] O. Faruk, A. K. Bledzki, H.-P. Fink, and M. Sain, “Biocomposites reinforced with natural fibers: 2000–2010,” *Progress in Polymer Science*, vol. 37, no. 11, pp. 1552–1596, 2012.
- [6] A. K. Bledzki, S. Reihmane, and J. Gassan, “Thermoplastics reinforced with wood fillers: a literature review,” *Polymer-Plastics Technology and Engineering*, vol. 37, no. 4, pp. 451–468, 1998.
- [7] T. J. Keener, R. K. Stuart, and T. K. Brown, “Maleated coupling agents for natural fibre composites,” *Composites Part A: Applied Science and Manufacturing*, vol. 35, no. 3, pp. 357–362, 2004.
- [8] N. Sombatsompop, C. Yotinwattanakumtorn, and C. Thongpin, “Influence of type and concentration of maleic anhydride grafted polypropylene and impact modifiers on mechanical properties of PP/wood sawdust composites,” *Journal of Applied Polymer Science*, vol. 97, no. 2, pp. 475–484, 2005.
- [9] C. Burgstaller, “Processing of thermal sensitive materials—a case study for wood plastic composites,” *Monatshefte für Chemie-Chemical Monthly*, vol. 138, no. 4, pp. 343–346, 2007.
- [10] A. S. Lodge, *Elastic Liquids*, Academic Press, New York, NY, USA, 1964.
- [11] M. L. Williams, R. F. Landel, and J. D. Ferry, “The temperature dependence of relaxation mechanisms in amorphous polymers and other glass-forming liquids,” *Journal of the American Chemical Society*, vol. 77, no. 14, pp. 3701–3707, 1955.
- [12] F. Erchiqui, F. Godard, A. Koukba, M. Vincent, and H. Kaddami, “Investigation of relaxation properties and potentiality of the thermoformability of HDPE charged by wood flours,” *Journal of Reinforced Plastics and Composites*, vol. 28, no. 10, pp. 1153–1168, 2009.
- [13] A. Bendahou, H. Kaddami, H. Sautereau, M. Raihane, F. Erchiqui, and A. Dufresne, “Short palm tree fibers polyolefin composites: effect of filler content and coupling agent on physical properties,” *Macromolecular Materials and Engineering*, vol. 293, no. 2, pp. 140–148, 2008.

Review Article

Preparation of Nanofibers with Renewable Polymers and Their Application in Wound Dressing

Ying Zhao, Yihui Qiu, Huanhuan Wang, Yu Chen, Shaohua Jin, and Shuseng Chen

School of Material Science and Engineering, Beijing Institute of Technology, Beijing 100081, China

Correspondence should be addressed to Yu Chen; cylsy@163.com

Received 11 December 2015; Accepted 17 February 2016

Academic Editor: Matheus Poletto

Copyright © 2016 Ying Zhao et al. This is an open access article distributed under the Creative Commons Attribution License, which permits unrestricted use, distribution, and reproduction in any medium, provided the original work is properly cited.

Renewable polymers have attracted considerable attentions in the last two decades, predominantly due to their environmentally friendly properties, renewability, good biocompatibility, biodegradability, bioactivity, and modifiability. The nanofibers prepared from the renewable polymers can combine the excellent properties of the renewable polymer and nanofiber, such as high specific surface area, high porosity, excellent performances in cell adhesion, migration, proliferation, differentiation, and the analogous physical properties of extracellular matrix. They have been widely used in the fields of wound dressing to promote the wound healing, hemostasis, skin regeneration, and treatment of diabetic ulcers. In the present review, the different methods to prepare the nanofibers from the renewable polymers were introduced. Then the recent progress on preparation and properties of the nanofibers from different renewable polymers or their composites were reviewed; the application of them in the fields of wound dressing was emphasized.

1. Introduction

Renewable polymers, including the polymers directly extracted from biomass and proteins, for example, starch, chitosan, cellulose, alginate, gelatin, and collagen [1], have attracted considerable attentions in the last two decades, predominantly due to their environmentally friendly properties, renewability, good biocompatibility, biodegradability, bioactivity, and modifiability [2]. The nanofibers prepared from the renewable polymers can combine the excellent properties of the renewable polymer and nanofiber [3], such as high specific surface area, high porosity, excellent performances in cell adhesion, migration, proliferation, differentiation, and the analogous physical properties of extracellular matrix (ECM). They have been widely used in the fields of wound healing, hemostasis, skin regeneration, and treatment of diabetic ulcers. In the present review, we will focus on the preparation, composition, and properties of nanofibers prepared with renewable polymers and their applications in the wound dressing. The research progress and development directions were also discussed.

2. Methods for the Preparation of Nanofibers with Renewable Polymers

As nanofibers are becoming increasingly important, the high throughput preparation of high quality nanofibers has drawn remarkable attentions. Currently, electrospinning is the most widely used method for the preparation of nanofibers. Other methods including Bubbfil spinning, centrifugal spinning, and freeze-drying have also been reported for their potential applications in the biological field.

2.1. Electrospinning. Electrospinning is the most commonly used method for the fabrication of nanofibers due to its simplicity, adaptability, cost-efficiency, and versatility [4].

In a typical electrospinning process, a high voltage is applied to a liquid polymer, leading to the ejection of a continuous jet strand from the spinneret towards a grounded collector. The surface tension of the polymer droplet is overcome by the applied electric field. The droplet then elongates to form a cone known as “Taylor cone” and then is extruded from the

cone to form a fiber jet. The solvent in the jets is evaporated as the fiber jets travel through the atmosphere and solid polymer fibers are deposited on the metal collector as nonwoven web [4].

Based on the preparation process of the polymer, the electrospinning process can be classified into two groups including solution electrospinning and melt electrospinning. Solution electrospinning is limited mainly by its low productivity, extra solvent extraction process, and requirement of toxic solvent. Yet it is much more thoroughly reviewed than melt electrospinning by researchers due to more concerns on melt electrospinning, such as difficulties inherent in the finer fiber formation, higher viscosity of polymer melts, and electrical discharge issues associated with the application of high voltage [5]. Thus, several setups including multijets from single needle, multijets from multineedle, and needleless systems have been proposed for solution electrospinning to increase its productivity.

2.1.1. Multijets from Single Needle Electrospinning. For single needle electrospinning (SNE) process, a single jet is initiated from the Taylor cone formed by the application of electric field. Li et al. prepared poly(lactic acid) (PLA)/chitosan core-shell structure nanofibers from a homogeneous solution using SNE and found that this method was simpler and more effective in producing core-shell structures from homogeneous solutions than other methods [6]. Ayaz et al. successfully prepared composite nanofibers with SNE and coaxial (double needle) electrospinning and compared their performances. The polymer matrix and filler were mixed before being infused into the single needle for SNE. Therefore, the filler was uniformly distributed in the whole nanofiber. In contrast, polymer matrix and filler were infused separately into two nozzles axially centered to each other for coaxial electrospinning, which restricted the filler in the center of nanofiber. In addition, the average diameter of the nanofibers prepared by SNE is smaller than that of the nanofibers prepared by coaxial electrospinning. However, nanofibers prepared through SNE showed lower breaking elongation than those prepared by the coaxial method [7].

2.1.2. Multijets from Multineedle Electrospinning. As discussed above, SNE provides very low throughput productivity [8]. Multineedle electrospinning (MNE) system is a simple way to improve the productivity and a simple technique to fabricate composite fibers from the polymers that cannot be easily dissolved in common solvents. However, the needle configuration, number of needles, and needle gauge need to be optimized for the MNE design. For example, needles can be arranged in one- or two-dimensional configuration. However, charged jets could interfere with each other and restrain jets injected from the spinneret, leading to low production efficiency [9, 10]. The interference between the charged jets can be resolved by several methods.

Nuryantini et al. prepared PVA/chitosan nanofiber membranes using an MNE system with a drum collector. Compared with conventional electrospinning setups, MNE setup can significantly improve the throughput while maintaining the uniformity of the size and thickness of the stacked

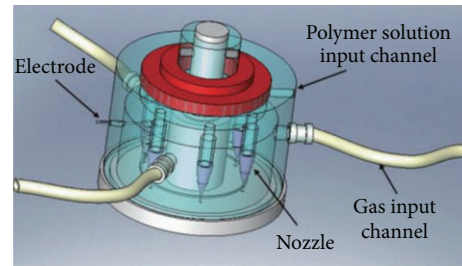


FIGURE 1: Setup of MNE spinneret assisted with sheath gas [9].

nanofibers [11]. Yu et al. fabricated nanofibers using a novel MNE setup with assistant sheath gas as shown in Figure 1 [9]. The assistant sheath gas introduced to the spinneret improved the stretching process of the charged jet and realized multijet injection. During the electrospinning, assistant gas was pumped into the chamber through gas input channels, which were uniformly distributed and thus contributed to each spinneret evenly. Sheath gas at a pressure of 50 kPa decreased the average diameter of the nanofibers from 600 nm to 472.8 nm and decreased the diameter distribution region from 249 nm to 188 nm. The assistant sheath gas also promoted the stability of the electrospinning and the uniformity of the nanofibers due to its ability to reduce the required voltage for jet injection and jet surface charge density [9].

2.1.3. Multijets from Needleless Electrospinning. MNE system usually needs a big space and optimization of the relative distance between needles to avert strong charge repulsions between the jets. Therefore, needleless electrospinning has been developed and widely used due to its notable ability to increase the production of nanofibers. For the needleless electrospinning, an electric field is applied on a large area, producing numerous polymeric jets from free liquid surface [5, 8].

Sasithorn and Martinová prepared silk nanofibers by both needle electrospinning and needleless electrospinning and found that the mass production rate of needleless electrospinning was much higher than that of needle electrospinning. In addition, the production rate of needleless electrospinning could be increased significantly with the increase of solution concentration and applied voltage. However, nanofibers produced by needle electrospinning were much smaller and had a narrow diameter distribution [12].

Wang et al. prepared uniform nanofibers using a needleless electrospinning system with a rotating spiral wire coil as the spinneret (Figure 2). The polymer solution was charged with a high voltage and loaded onto the coil surface by slowly rotating the coil at 40 rpm. They found the production of nanofiber was improved by increasing the length (D) and diameter (ϕ) of the coil or decreasing the spiral distance (d) and the diameter (ϕ_w) of the wire. However, these factors showed no significant effect on the average diameter of the nanofibers. Compared with the needle electrospinning, the needleless electrospinning with coil spinneret showed better performance, such as producing thinner nanofibers and higher productivity [13].

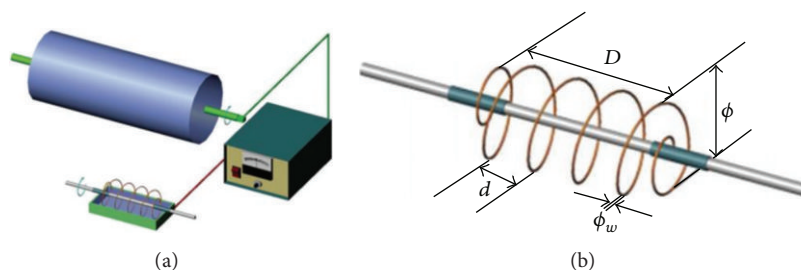


FIGURE 2: (a) Schematics of spiral coil electrospinning setup; (b) magnified view of the coil [13].

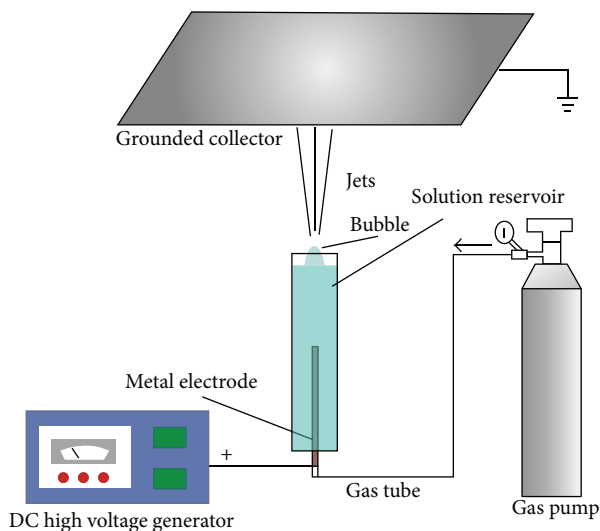


FIGURE 3: Bubble electrospinning setup for tunable bubble size [14].

2.2. Bubbfil Spinning. It is known that the increases in the molecular weight and viscosity of polymers lead to higher surface tension of their Taylor cone, which cannot be used to fabricate nanofibers by the conventional electrospinning methods. Therefore, higher electrostatic force is required for the electrospinning to fabricate desired nanofibers [14]. Other drawbacks of electrospinning including low productivity and uncontrollability of the spinning process call for the development of other technologies [15].

Bubbfil spinning including bubble electrospinning and blown bubble spinning is one of main newly developed methods for the preparation of nanofibers.

2.2.1. Bubble Electrospinning. Bubble electrospinning has attracted considerable attention due to its high throughput. Unlike conventional electrospinning, bubble electrospinning uses electrostatic force rather than Taylor cone to overcome the surface tension of a polymer bubble [16, 17]. The electrospinnability of bubble electrospinning depends geometrically on the sizes of the obtained bubbles, which avoid using high voltages and thus make it the best candidate in the green production. Figure 3 shows a typical bubble electrospinning setup.

In a typical bubble electrospinning process, bubbles are formed on the surface of a polymer solution by a controllable

syringe pump as the gas pump slowly turned on. The number of the bubbles is reduced with the decrease of the tube diameter. Multiple jets are then ejected from the bubbles to the grounded collector when the applied voltage surpasses a critical value. The fluid jets are usually solidified into fibers in less than 0.001 seconds [5, 14].

Jiang et al. mass-produced nanofibers with an improved microbubble electrospinning system where a pyramid-shaped copper spinneret was used as the generator. They found that the increase of bubble size from $29.6 \pm 8.2 \mu\text{m}$ to $152.7 \pm 22.7 \mu\text{m}$ led to an increase in the average diameter of nanofibers from 139 ± 39 to 165 ± 26 nm. The microbubble electrospinning produced nanofibers with average diameter of 147 ± 28 nm with the bubble sizes of $59.9 \pm 10.8 \mu\text{m}$, which are similar to those produced by the conventional electrospinning with the same processing parameters. The throughput of microbubble electrospinning reached 8.9 g/h, which was much higher than that of the conventional electrospinning (5.2 g/h) [18].

2.2.2. Blown Bubble Spinning. Blown bubble spinning produces nanofibers using blowing air and has been used commercially as a one-step process to convert polymer resin directly into a nonwoven mat of fibers. Figure 4 shows an experimental setup of blown bubble spinning.

Blown bubble spinning process is very much similar to bubble electrospinning except that it uses blowing air instead of electronic force to produce fine fibers [19]. However, a weak electronic field can significantly improve the performance of the blown bubble spinning, which actually turns into an electrostatic-field-assisted blown bubble spinning (Figure 5). It can also be called as air-jet assisted bubble electrospinning, depending on which one is the major functional force [14].

Li et al. prepared silk fibroin through blown bubble spinning and found that the direction of blowing air, both perpendicular (setup I in Figure 6(a)) and parallel (setup II in Figure 6(b)) to the ejected direction of broken polymer bubble, could affect the morphology, structure, and arrangement of the produced fibers. For example, random oriented nanofibers with an average diameter of 524.25 ± 142.41 nm were formed through setup I and well organized fiber bundles were obtained with setup II [16].

2.3. Centrifugal Spinning. Centrifugal spinning, also called rotary spinning or rotational jet spinning, has been well developed. Since no high voltage is required by the centrifugal

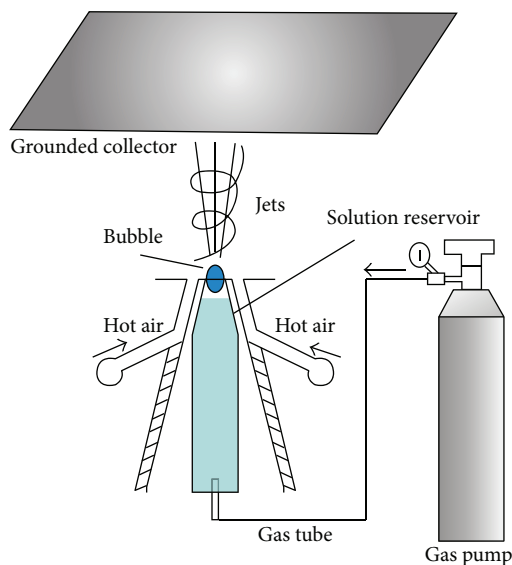


FIGURE 4: Blown bubble spinning (the only acting force is blowing air) [14].

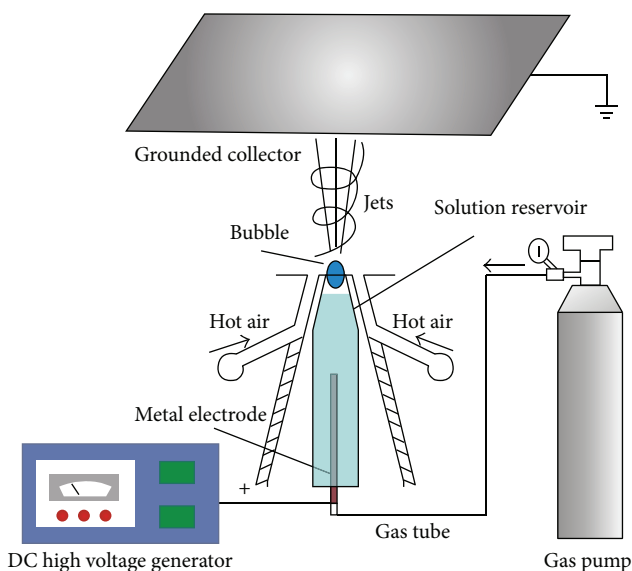


FIGURE 5: Air-jet assisted bubble electrospinning or electrostatic-field-assisted blown bubble spinning [14].

spinning, the system can alleviate safety-related concerns. In addition, centrifugal spinning can remarkably improve the production efficiency by increasing the rotational speed, allowing the fast and large-scale fabrication of nanofibers. Compared with the electrospinning process, it also allows nanofiber fabrication from the polymers at much higher concentrations, which decreases the use of solvent and lowers the production cost [20].

During a typical spinning process, a polymer solution is introduced into a highly rotating spinneret and then ejected as jets at a high rotating speed which is used to overcome the surface tension. The jets are then deposited on the collectors to form dried nanofibers as the solvent evaporated during

the stretching process. Figure 7 shows a typical setup for centrifugal spinning [20].

Hammami et al. prepared nanoscale fibers using centrifugal force spinning and found that centrifugal force spinning also required certain chain overlap or entanglement. However, needles with smaller inner diameters were used for the centrifugal force spinning, which significantly improved the spinnability of the nanofiber [21].

Erickson et al. fabricated highly aligned chitosan/polycaprolactone (PCL) nanofibers via centrifugal electrospinning system. Compared with those produced by the conventional electrospinning, the nanofibers produced by centrifugal electrospinning showed more uniform diameters and were aligned vertically. The diameter distribution of the nanofibers produced by centrifugal electrospinning was from 100 nm to 275 nm, which was much narrower than that of the nanofibers produced by the conventional electrospinning (25–450 nm) [22].

2.4. Freeze-Drying. Freeze-drying (FD) can fabricate porous structures with controllable sizes directly from polymers, such as chitin, without structure-directing additives or pre-treatments needed, which cannot be achieved by other techniques, such as self-assembly and electrospinning [23]. In addition, no high temperature and further leaching step are required for the freeze-drying process [24]. Therefore, it has drawn increasing attention in the fabrication of nanofibers. Starting with solution, emulsion, or dispersion, freezing leads the solute or solids to be excluded by ice front in the interstitial spaces between ice crystals. Then porous structures are created by the following sublimation [23].

Ma et al. prepared chitosan (CS)/sodium hyaluronate (SH) polyelectrolyte complex (PEC) fibers by FD method. The SEM images indicate that the equimolar ratio of CS to SH benefits the formation most. The *in vitro* tests indicate that the freeze-dried fibers have no cytotoxicity and good compatibility, which are essential for its application in aqueous systems, especially for biological and environmental applications [25].

Wu and Meredith prepared nondirectional and aperiodic chitin nanofibers (CNFs) by FD method. The prepared structures successfully mimicked the size and interconnectivity of white beetle structure with improved porosity. In all, the fine and porous structure can be realized by more facile water-based FD method [23].

3. Renewable Polymers for the Preparation of Nanofibers

3.1. Chitosan. Chitosan (CS) is a natural cationic polyelectrolyte copolymer that can be obtained by the deacetylation of its parent polymer chitin, a naturally occurring source derived from the exoskeleton of insects, crustaceans, and certain fungi. The abundance as a renewable resource and excellent properties, such as hemostasis, biodegradability, biocompatibility, nontoxicity, and chelation with metals, render chitosan suitable for biomedical applications. Moreover, chitosan has also shown good performances in inhibiting the growth of a wide variety of yeasts, fungi, and bacteria as

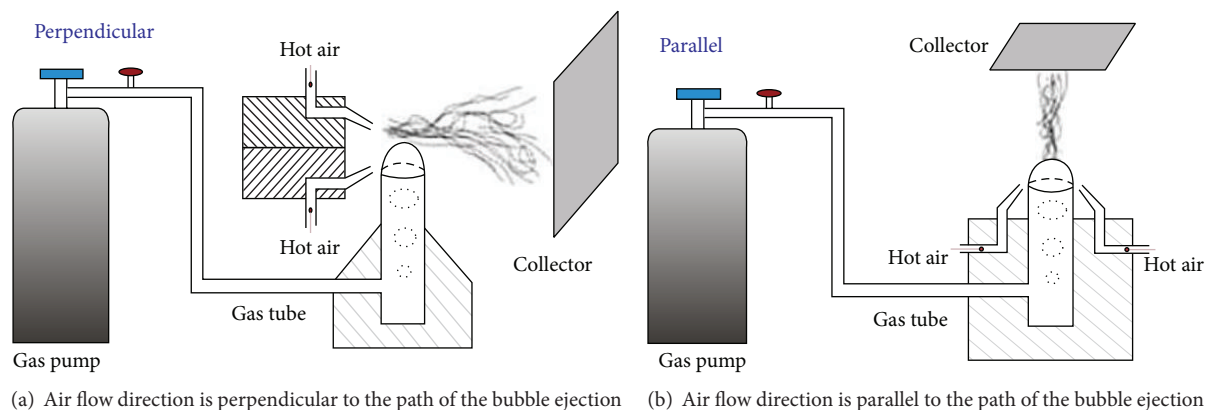


FIGURE 6: The schematic of the experimental setup of two airflow directions: (a) perpendicular flow and (b) parallel flow [16].

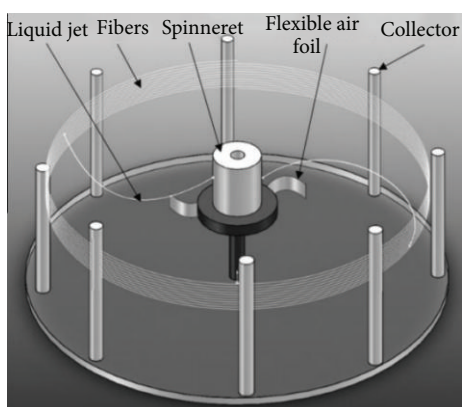


FIGURE 7: Setup of centrifugal spinning [20].

well as gas and aroma barrier properties in dry condition. All these positive features of chitosan have provided ample opportunities for further development in biomedical and other industrial fields [26–28].

It has been reported that pure chitosan fibers can be produced in nonaqueous solvents. For example, electrospinning of pure chitosan was successfully achieved in trifluoroacetic acid (TFA) by Ohkawa et al. [29]. Sencadas et al. improved the homogeneity of the nanofibers by adding dichloromethane to the chitosan/TFA mixtures and systematically studied the processing parameters to set the ground for a reproducible way to obtain chitosan nanofibers for specific applications [30].

However, electrospinning individual chitosan from its aqueous solution remains a challenge. First, the rigid D-glucosamine repeat unit, high crystallinity, and ability to form strong hydrogen bond of chitosan make it difficult to be dissolved in most solvents. In addition, its polycationic property also leads to high viscosity, which hinders the formation of sufficient chain entanglements and results in the formation of nanobeads rather than nanofibers [26, 31]. However, the solvents for the spinning of the pure chitosan are environmentally harmful [32]. The electrospinning for chitosan can only be achieved at concentrations in the range between 2%

and 8% (wt/v). This urges us to develop new versatile methods for the electrospinning of chitosan at higher concentrations to ensure the mechanical stability and retain the bioactivity of its nanofiber products [33].

Therefore, special attention needs to be paid to improving the spinnability of chitosan. Attempts have been made by blending chitosan with synthesized polymers, such as polyethylene oxide (PEO), polyvinyl alcohol (PVA), and PLA, and renewable polymers such as gelatin, alginate, and silk fibroin and nanoparticles to improve the mechanical strength, antibacterial activity, and antiadhesive properties towards bacteria of its nanofibers [31, 34].

PVA is a typical nontoxic and water-soluble synthesized polymer with high biocompatibility and hydrophilicity. More importantly, PVA has good mechanical properties [35]. Liu et al. explored the preparation of PVA/chitosan hydrogel nanofibers by solution blowing method with ethylene glycol diglycidyl ether (EGDE) as cross-linker at various concentrations (as shown in Figure 8) and found that CS/PVA hydrogel nanofiber mats possessed the properties of both hydrogel and nanofiber mats. In addition to the similar excellent exudate absorption property to that of hydrogel films, hydrogel nanofiber mats allowed gaseous exchange, which decreased with the increase of its cross-linking degree (DCL). Moreover, CS/PVA hydrogel nanofiber mats demonstrated good antibacterial rates of over 81% against *E. coli*, which was not significantly affected by DCL. The findings suggest that the CS/PVA nanofiber hydrogel is a promising material for wound dressing [36].

Compared with synthetic polymers, natural polymers have better biocompatibility and lower immunogenicity. Sericin is one of the biodegradable and biocompatible natural polymers with good antioxidant, moisture absorption, and antibacterial and UV resistance properties and has been widely used in cosmetics and fabrics. Zhao et al. prepared chitosan/sericin composite nanofibers by blending binatural polymers and electrospinning to enhance their biological performance. The nanofibers had diameters ranging from 240 nm to 380 nm and continuous and uniform diameter distribution. Bioassays indicated that these novel composite nanofibers showed noncytotoxicity and remarkably

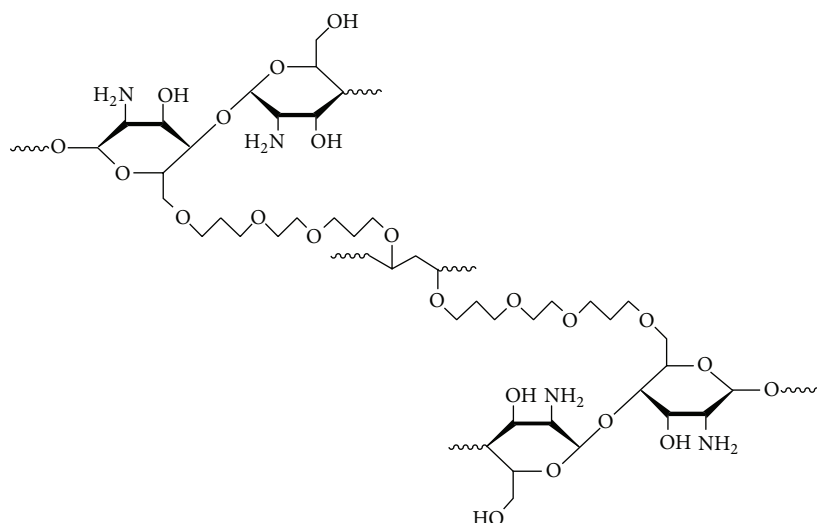


FIGURE 8: The structure of CS/PVA hydrogel nanofibers cross-linked by EGDE.

enhanced cell proliferation and antibacterial activities against both Gram-negative bacteria *Escherichia coli* and Gram-positive bacteria *Bacillus subtilis* [34].

Ag nanoparticles (Ag-NPs) have shown superior antibacterial properties. Ag-NPs can attach to cells to interrupt their permeability and intermembrane exchange. In addition, Ag-NPs have no adverse effects on viable cells and cause no significant microbial resistance. Therefore, Ag-NPs have been widely used as additives to various materials and in wound dressings against microbial contaminations [35, 37]. Abdelgawad et al. successfully prepared chitosan/PVA/Ag-NPs nanofiber mats with chitosan as capping polymer at high concentrations and glucose as reducing agent for antimicrobial applications. Ag-NPs were able to improve the electrospinnability of the blend, reduce the diameter of fibers, and more importantly enhance the antibacterial performances of the electrospun fibers, which made them viable to wound dressing [37].

3.2. Cellulose. Cellulose is one of the most abundant biodegradable materials and can be extracted from different natural sources, such as wood and cotton pulps, via chemical and/or physical methods [38].

Bacterial cellulose (BC) is natural cellulose synthesized by acetobacter xylinum [38] and has high biocompatibility and transparency, nontoxicity, and excellent mechanical strength. Moreover, BC fibers have a very high surface area per unit mass, which, combining with its high hydrophilicity, leads to a very high liquid loading capacity. Thus, BC has been applied in various fields [39]. Costa et al. carried out electrospinning of acetylated BC nanofiber mats to produce artificial symmetric nanoporous structures. The SEM images revealed that nanopores were more uniformly distributed throughout the electrospun nanofiber mat than those casted with BC mats. In addition, the electrospinning of modified BC nanofibers was easier than that of unmodified BC nanofibers, which could be explained by the dissolution mechanism of cellulose in DMA/LiCl solvent system [40].

However, BC shows poor antibacterial, antioxidant, and conducting and magnetic properties, which limits its application in biomedical and electronic fields [41]. One of the solutions is to blend BC with other substances to promote its properties. Carbon nanotubes (CNTs) have been of great interest in various fields since their discovery. They are promising fillers for polymer matrices to prepare CNTs-reinforced composite materials because of their extraordinarily high aspect ratio, elastic modulus, and high axial strength. Chen et al. prepared multiwalled CNTs-embedded BC nanofibers (MWCNTs/BC nanofibers) by electrospinning. The TGA analysis showed that the initial temperature of degradation followed the increasing order of BC < electrospun BC nanofibers < electrospun MWCNTs/BC nanofibers, which was attributed to the crystalline polymorph transformation and orientation as well as the embedded MWCNTs. In addition, the mechanical properties including tensile strength and Young's modulus and electrical conductivity of the products were significantly enhanced due to the well-dispersed and aligned MWCNTs. The finding indicates that MWCNTs/BC nanofibers may be potentially used in medical, mechanical, and electrical fields [42].

Cellulose acetate (CA) is a derivative of cellulose and has good stability and solubility in organic solvent. It can also selectively absorb low-level organic compounds and toxins. However, CA has poor mechanical properties [43]. Khalf et al. fabricated a CA/polycaprolactone (PCL) core-sheath nanostructure by coaxial electrospinning to promote its mechanical and biological properties. The preparation process is shown in Figure 9. Their results indicate that the loading of PCL was able to improve the elastic elongation of CA solid and hollow fibers. Cell attachment test suggested that the nontoxicity and higher cell attachment performance of CA nanofibers blended with PCL were attributed to its higher surface area per volume ratio [44].

3.3. Alginate. Alginate is a natural linear polysaccharide copolymer and can be obtained from brown sea weed.

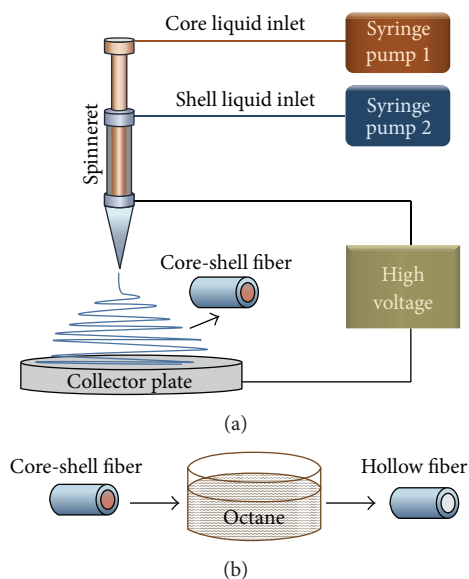


FIGURE 9: The preparation process of CA/PCL core-sheath nanostructures [44].

Sodium alginate (SA) has been well studied on its biomedical applications due to its superior properties including biocompatibility, biodegradability, nontoxicity, hydrophilicity, and low cost. Unlike chitosan, alginate is highly soluble in water [45].

To improve the structural integrity of the prepared nanofibers, alginate-based materials are usually cross-linked with divalent ions, such as calcium and barium. In addition, double cross-linking with glutaraldehyde, hexamethylene diisocyanate (HMDI), epichlorohydrin, and adipic acid (ADA) hydrazide has also been proposed (as shown in Figure 10). Unlike the non-cross-linked electrospun nanofibers, the cross-linked electrospun nanofibers are highly stable and relatively insoluble in both water and simulated body fluid [46–48].

However, pure SA nanofibers have been rarely fabricated via electrospinning. Nie et al. [49] prepared smooth and uniform alginate nanofibers by introducing glycerol as a cosolvent and simply adjusting the volume ratio between glycerol and water. Fang et al. [50] reported that pure alginate had been successfully electrospun by introducing Ca^{2+} cations to SA aqueous solutions. They demonstrated that high intermolecular interactions and low surface tension were the critical factors to improve the electrospinnability of SA solutions.

Alginate has poor properties including low mechanical strength, high degradation rates, and processing difficulties, which are usually overcome by compositing alginate with other polymers such as PEO [51] and PVA [45]. It can be attributed to the intermolecular hydrogen bonds formed between the polymers and alginate. Surfactants, such as lecithin [52], and cosolvents have also been proposed to facilitate its processing for the preparation of nanofibers [53].

3.4. Gelatin. Gelatin (GT) is a renewable polymer obtained by the partial hydrolysis of collagen, a most abundant natural

substance in connective tissues. GT has been widely used as a bioengineering material due to its high biocompatibility, biodegradability, and low cost. GT can also prevent fluid loss, which plays an important role in wound healing [54–56]. However, the electrospun gelatin nanofibers are soluble in water and have poor mechanical strength [56, 57]. Therefore, cross-linking treatments have been adopted to increase their water resistance [13] and mechanical properties [58, 59]. The cross-linking can be realized by physical processes, such as drying, heating, γ -ray, electron beam, and UV light exposure and chemical treatments by using cross-linker, such as formaldehyde, glutaraldehyde (GA), epoxy compounds, tannic acid, carbodiimide, acyl azide, and transglutaminase [60], through dissolving gelatin in 2,2,2-trifluoroethanol [61], formic acid dope solution [62], and water-based cosolvent composed of ethyl acetate and acetic acid [63]. Among all chemicals, GA is by far the most widely used due to its high efficiency, easy accessibility, and low cost. However, glutaraldehyde at high concentrations is cytotoxic and can disrupt the electrospun fiber morphology [59, 64]. Ko et al. [60] demonstrated that the gelatin nanofibers cross-linked with 0.5% (w/v) genipin promoted cell proliferation and reduced its solubility and cytotoxicity. Lu et al. [65] fabricated gelatin nanofibers by electrospinning and compared the properties of the gelatin nanofibers cross-linked by vapor and liquid-phase GA. Their results indicated that the cross-linking by both vapor-phase and liquid-phase GA was able to improve the mechanical strength of the gelatin fibers. The cross-linking with liquid-phase GA resulted in more evenly cross-linked, close-packed, and higher tensile. The excessive cross-linking with vapor-phase GA led to membranes shrinking due to poorly cross-linked middle layers in their hierarchy structure. Therefore, a novel *in situ* cross-linking method was proposed by Slemming-Adamsen et al. [66] for the fabrication of electrospun gelatin nanofibers with 1-ethyl-3-(3-dimethylaminopropyl)-1-carbodiimide hydrochloride (EDC) and N-hydroxysuccinimide (NHS) as cross-linkers. Kwak et al. [67] prepared *Phaeodactylum tricornutum* (*P. tricornutum*) extract-loaded gelatin nanofibers via electrospinning. *P. tricornutum* is a diatom which exists in brackish and marine water worldwide. The water-soluble extracts of *P. tricornutum* have showed anti-inflammatory, analgesic, and free radical scavenging activities. The introduction of *P. tricornutum* extracts improved the conductivity of the gelatin solution and reduced the diameter of the nanofibers. Their results also confirmed the antimicrobial activity and noncytotoxicity of the *P. tricornutum*-loaded gelatin nanofibers.

Gelatin has also been used as a blend component to prepare nanofibrous membranes for tissue scaffolds, wound healing and health caring devices, and other biomedical applications. Shan et al. [68] prepared silk fibroin/gelatin (SF/GT) electrospun nanofibrous dressing loaded with astragaloside IV (AS), an effective component, to accelerate wound healing. They found that the nanofibers were able to significantly improve cell adhesion and proliferation, promote wound healing, induce proangiogenesis of partial thickness burn wound, and inhibit complications in wounds. In addition, SF significantly decreased the average diameter,

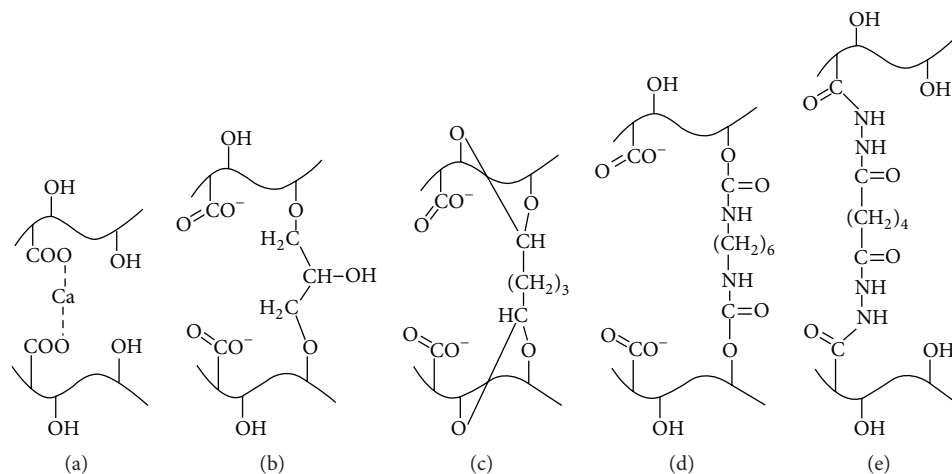


FIGURE 10: Molecular network structures formed between alginate chains in nanofibers after cross-linking with (a) CaCl_2 , (b) epichlorohydrin, (c) glutaraldehyde, (d) HMDI, and (e) ADA [46].

degradation rate, and the failure strain under high break strength of the produced nanofibers.

In addition to the general properties of a condensed polyphenol, the grape seed polyphenol (GSP) has some unique properties, such as antimicrobial activity, anti-inflammatory activity, and reducing blood sugar and fat. Han et al. [69] fabricated GSP/gelatin composite nanofibers containing Ag-NPs by electrospinning as a novel biomaterial. The process is shown in Figure 11. GSP served as the reducing agent and the stabilizing agent for silver nanoparticles. The electrospun composite nanofibers had average diameters in the range of 150–230 nm and a uniform distribution of Ag-NPs with an average diameter of 11 nm that contributed to their good antibacterial performance. Further investigation also revealed that the composite nanofibers containing silver nanoparticles had no toxicity at such concentrations. Thus, they could be potentially utilized in biomedical field as a wound dressing.

3.5. Hyaluronic Acid. Hyaluronic acid (HA) is one main glycosaminoglycan which is found in the ECM of many soft tissues of higher animals [70]. HA can decrease the formation of postsurgical adhesions due to its noncoagulant activity, modulation of fibrous tissue, barrier effect on fibrinogen, and inhibitory effect on the superoxide release from granulocytes [71]. Previous studies have demonstrated that HA nanofiber wound dressing showed better performance than the solid HA in wound healing due to its unique morphologies. However, HA solutions have high solution viscosity even at low concentrations, leading to issues in the production of consistent nanofibers [72].

Brenner et al. prepared pure HA nanofibers by electrospinning in a solvent system of aqueous ammonium hydroxide (25% NH_4OH) and DMF at pH of 11 to eliminate the solvent induced degradation effects on the biopolymer as reported in the previous studies. Continuous, cylindrical, and randomly oriented pure HA nanofibers with a diameter of 39 ± 12 nm and good biocompatibility were successfully electrospun [70].

Uppal et al. fabricated HA nanofibers by electrospinning with deionized water as a solvent and cocamidopropyl betaine as a surfactant. Based on the report of histopathologist, the sterilized HA nanofibers wound dressing showed better pathology performance than other sterilized wound dressings including solid HA, gauze with Vaseline dressing, adhesive bandage, and antibiotic wound dressing. The evaluation criteria included epithelial tissue gap, epithelial tissue detachment from the dermis, the presence of granulation tissue, and the assessment from clinic photographs based on the color of the wound and whether the wound was fully covered or not by the epithelial tissue. In addition, it showed higher air permeability than sterilized solid HA and gauze with Vaseline dressing, which contributed to the faster wound healing [72]. In all, the addition of antibiotic components could lead to better performance of HA nanofibers.

Chen et al. prepared dual functional core-sheath structured nanofibers with HA as the inner core and Ag-NPs-loaded PCL as extremal sheath by coaxial electrospinning. This design was used to control the slow release of HA from the core to mimic the biological function of HA in synovial fluid containing high concentration of HA. The sheath acted as a barrier with antimicrobial activity to prevent infection and alleviate adhesion. The results demonstrated that the core-sheath structure met the need of preventing peritendinous adhesion and postoperative infection through the slowly released HA and rapid release of Ag-NPs without exhibiting significant cytotoxicity [71].

3.6. Collagen. Collagen is the principal structural element of the native ECM in a three-dimensional network structure composed of microfibrils in a nanofiber scale. Due to a wealth of merits including biological origin, nonimmunogenicity, and excellent biocompatibility and biodegradability, collagen has been widely used as biomaterials in pharmaceutical and medical fields such as carriers for drug delivery, dressings for wound healing, and tissue engineering scaffold. Among all isoforms of collagen, the fibrillar structure of type I

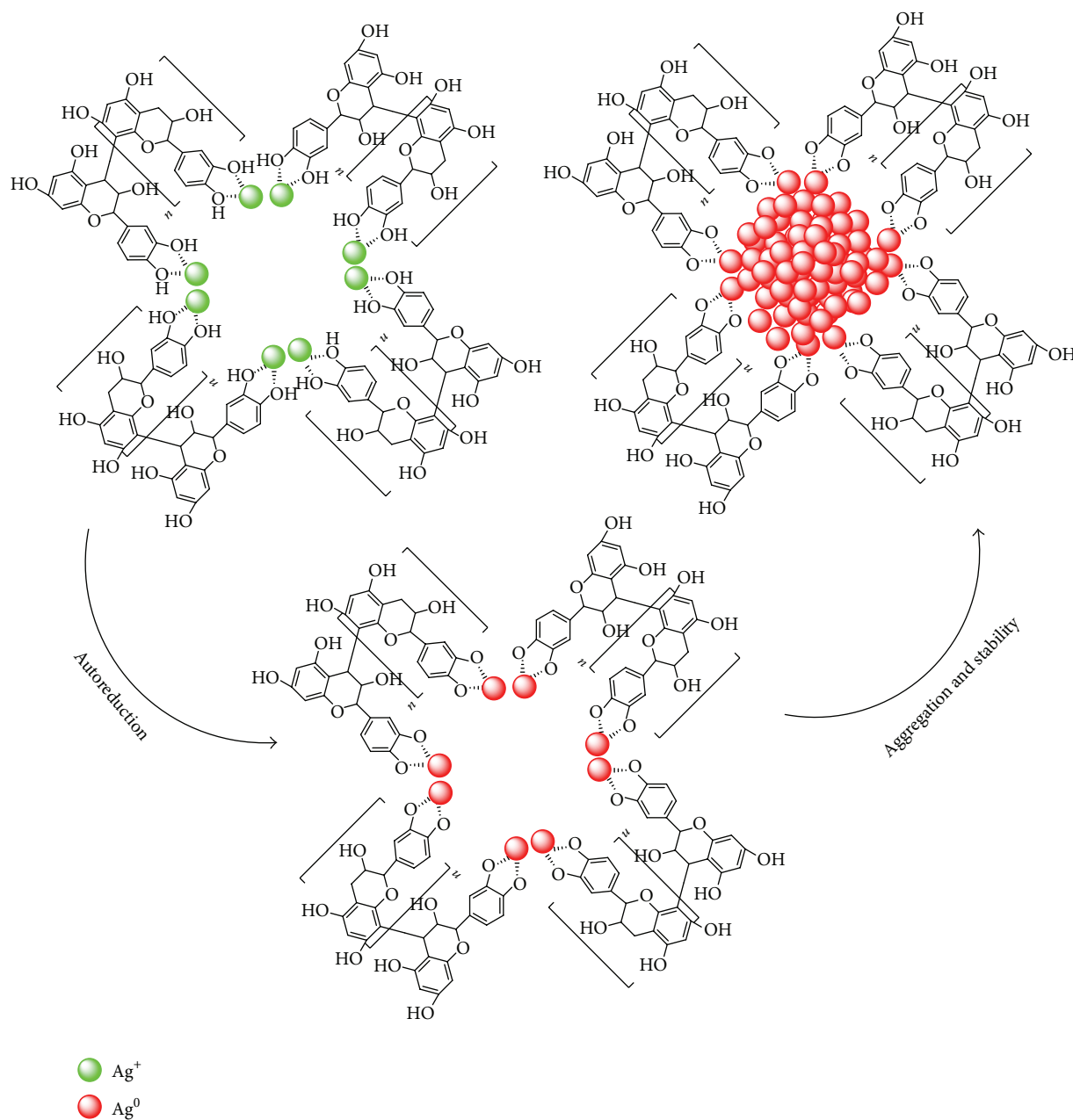


FIGURE 11: Schematic representation of the mechanism for preparing silver nanoparticles with GSP [69].

collagen has long been known for its important roles in cell attachment, proliferation, and differentiation [73, 74].

The adaptations of electrospinning to produce tissue engineering scaffolds composed of collagen nanofibers have shown that the structural properties of the electrospun collagen vary with the tissue of origin, the isoform, and the concentration of the collagen solution [75].

Collagen-composite fibrous mats have been fabricated with PEO [76], PCL [77, 78], polylactide-polyglycolide (PLGA) [75], poly(L-lactide-co- ϵ -caprolactone) (PLCL) [79], chitosan [73], hydroxyapatite [80, 81], and poly(L-lactic acid)-co-poly(ϵ -caprolactone) (P(LLA-CL)) [82]. Chen et al. [83] prepared the composite nanofibrous membrane (NFM) of

type I collagen, chitosan, and PEO by electrospinning, which was further cross-linked with GA vapor. The cross-linking increased Young's modulus of the NFMs and decreased their ultimate tensile strength, tensile strain, and water sorption capability. The NFMs showed no cytotoxicity toward the growth of 3T3 fibroblasts and demonstrated good biocompatibility *in vitro*. In addition, the NFMs showed better wound healing performances than gauze and commercial collagen sponge wound dressings. This novel electrospun matrix can also be potentially used as a wound dressing for skin regeneration. Choi et al. [78] examined the feasibility of using PCL/collagen based nanofibers as a scaffold system for implantable engineered muscle organization. Their results

showed that, in contrast to the randomly oriented nanofibers, unidirectionally oriented nanofibers could induce muscle cell alignment and myotube formation. The aligned composite nanofiber scaffolds seeded with skeletal muscle cells may be able to provide implantable functional muscle tissues. Liu et al. [84] explored the incorporation of neurotrophin (NT-3) and chondroitinase ABC (ChABC) into the electrospun collagen nanofiber for spinal cord injuries (SCI) treatment. The sustained release of NT-3 and ChABC for at least 28 days was achieved. Such biofunctional scaffolds may be found useful in SCI treatment by providing topographical and multiple biochemical cues to manipulate the growth inhibitory environment and promote axonal regeneration.

3.7. Silk Fibroin. Silk fibroin (SF) is a main component of silk. It is a type of fibrous proteins with remarkable mechanical properties produced in the form of fiber by silkworms and spiders. SF is also a promising wound dressing material due to its excellent mechanical properties, as well as its biocompatibility, controllable biodegradability, water-based processing, morphologic flexibility, and easily accessible chemical groups for functional modification. Despite its advantages, the low availability of SF limits the industrial scale production of its biomaterials. Generally, the electrospun SF fibers with desirable properties for bioengineering are prepared with SF at very high concentrations in the range of 20–40%. In addition, the highly crystalline β -sheet secondary structures result in the insolubility of SF, which limits its biomedical applications. Therefore, electrospun SF nanofibers are usually chemically treated with methanol [85], ethanol, propanol [86], and water vapor [87] to increase their stability. Strategies have been proposed to increase the viscoelasticity of SF systems by blending them with other polymers, which improves the mechanical properties while maintaining the biocompatibility of the obtained nanofibers [88–91].

Calamak et al. [92] fabricated silk fibroin nanofibers containing UV-reduced Ag-NPs by electrospinning method and posttreated the product with methanol and GA vapor. The posttreatments promoted the mechanical properties of the SF bionanotextiles. The results indicate that the methanol treatment was more effective in the crystallization transition of fibroin from random coil to β -sheet. In addition, Ag-NPs significantly decreased the diameter of the nanofibers and contributed to their antibacterial activity against Gram-positive bacteria *S. aureus* and Gram-negative bacteria *P. aeruginosa*.

Polyethylenimine (PEI) is a polycationic antimicrobial polymer with interesting ability to enter cells or permeabilize cell membranes. Çalamak et al. [90] prepared silk fibroin based antibacterial bionanotextiles and explored their application as wound dressing materials. The addition of PEI to the nanofibers decreased the average diameter of the nanofibers and increased their hydrophobicity, cell viability, and antimicrobial activity against both Gram-positive and Gram-negative bacteria. In contrast, the sulfated SF only showed antibacterial activity against *P. aeruginosa*.

Shahverdi et al. [89] fabricated silk fibroin blended with PLGA nanofibers via a dual source electrospinning setup, through which the electrospinning of SF and PLGA nanofibers could be separately optimized and achieved. They found

that the concentrations of SF and PLGA predominantly affected the formation of the bead structure in the fibers. The addition of PLGA significantly improved the mechanical properties of the nanofibers. The incorporation of SF with PLGA displayed better cell attachment, proliferation, and viability performance than pure SF nanofibers and pure PLGA nanofibers.

A novel tissue engineering scaffold of electrospun silk fibroin/nanohydroxyapatite (nHA) biocomposite was prepared by an effective calcium and phosphate (Ca-P) alternate soaking method. The cell cultivation experiments demonstrated that the silk/nHA nanocomposite scaffold could support the early stage of osteoblast adhesion and had a significant effect on the differentiation stage. Their findings suggest that this composite scaffold can be a promising biomaterial for bone tissue engineering [93].

Ki et al. [94] determined the characteristics and performance of an electrospun membrane prepared with wool keratose (WK) and SF protein for metal ion absorption. The nanofibrous membranes exhibited higher metal ion absorption capacities than the conventional fibrous filters (wool sliver and filter paper). Particularly, the WK/SF blend nanofibrous membrane showed an extraordinary performance for the absorption of metal ions. In addition, its absorption capacity remained stable after several adsorption-desorption cycles. The electrospun WK/SF nanofibrous membrane is suitable for removing and recovering heavy metal ions in water.

4. Applications of Renewable Polymer Based Fibers in Wound Dressing

Effective wound dressings are highly desired in various areas, such as promoting wound healing, hemostasis, skin regeneration, diabetic ulcers, and tissue engineering. A good wound dressing can maintain a moist environment at the interface, provide mechanical protection, prevent bacterial penetration, and allow gas-fluid exchange. In addition, it is nonadhesive to the wound and easily removed without trauma. However, the dressings used in specific fields may have their unique properties and requirements.

4.1. Promoting Wound Healing. A variety of fibers prepared with renewable materials including chitosan, fibrinogen, silk fibrin, bacterial cellulose, gelatin, and collagen and composites of these materials can promote wound healing and show antibacterial activity, good adhesion, good absorption, and nontoxicity and sufficient gas-exchange properties. The mats prepared with the fibers have unique porous structures and high surface areas, which are beneficial to cell regeneration and the wetness of the wound. In addition, the mats can protect the wound from the harmful external environments [95].

The bioactive molecules or drugs can be easily incorporated in the fibers by electrospinning to provide additional functions such as anti-inflammatory activity and tissue growth-promoting activity [96, 97]. Wu developed a composite dressing of alginate, hydroxyethyl cellulose, and growth factor and successfully applied it to the treatment of facial wounds [98].

Chitosan fibers blended with other polymers, such as PEO, PLA, PVA, and PCL, have been proved as promising candidates for wound healing dressing [99]. Huang et al. reported that chitosan/poly-L-lactic acid (PLLA) composite nanofiber prepared by electrospinning showed better performance in maintaining wettability than pure PLLA and thus accelerated wound healing [100]. Theisen et al. found that blending gelatin with PLLA led to a better performance for cell proliferation and ECM production and the cells were able to grow into tissue-like constructs [101]. Alginate might provide gelation and moist healing environment for chronic wounds, boosting their reepithelialization [102]. de Moraes and Beppu prepared a biocomposite membrane with sodium alginate and silk fibroin fibers. The incorporation of fibroin fibers enhanced the tensile strength of the fibers and resulted in the properties of a typical biomaterial for biomedical applications such as wound dressing. Its nontoxicity and flexibility also contributed to the fast wound healing [103].

4.2. Hemostasis. Timely and rapid hemostasis is very important to avoid further complications in surgical operation and emergency medical treatment. An effective hemostatic dressing should have properties such as excellent hemostasis, good biocompatibility, nontoxicity, no antigenicity, low cost, and easy processing [104].

Various renewable polymers, such as fibrinogen, fibrin, alginate, chitosan, cellulose, and gelatin, have been used in the preparation of hemostatic dressings. These materials in the form of fiber have shown excellent performances in hemostasis due to the large contact areas with blood which promotes the aggregation and adhesion of thrombocyte on the fibers. In addition, the soft and strong fiber can closely adhere to the wound and press the wound to promote hemostasis.

Zhao et al. prepared a nanofiber of fibrinogen fiber by electrospinning and applied it to hemostasis. The clinical study indicates that the dressing was able to significantly shorten bleeding time and decrease bleeding volume of splenic hemorrhage, hepatic hemorrhage, and femoral arteriovenous fistula, thus reducing mortality rate [105]. The fibrinogen forms a tough fibrin clots once it is activated by thrombin. The clot adheres to the wound and promotes hemostasis to accelerate wound healing. In addition, cross-linked fibrinogens have certain toughness and viscosity, which can prevent blood flushing and provide a physical hemostasis [106].

Fibrin is used in hemostasis due to its biocompatibility and excellent biological properties [107]. Fibrin is an initiator for the regulation of thrombosis and hemostasis. It is decomposed by fibrinogen, the major component of plasma proteins, when human body gets wounded and immediately covers the wound to accelerate the hemostasis [108]. During the healing process, fibrin can be completely degraded and absorbed by the tissue and causes no damage to the organism nearby.

Alginate is also an excellent hemostatic material. Pillai and Naieb prepared a ventral nonadhesive dressing with a soft net of pure calcium alginate, which showed an excellent hydrophilism. During the treatment, it swelled upon the absorption of exudate and formed a firm gel filled wound

without adhesion, which maintained a moist environment for the wound and promoted its healing [109]. In addition, Ca^{2+} in the alginate fibers could be transferred into the blood by exchanging with Na^+ and acted as a coagulation factor to accelerate the hemostasis.

Sibaja et al. synthesized a fiber by composing chitosan with alginate through wet extrusion and found that it was a biocompatible material with acceptable tensile properties for the inhibition of body fluids, such as blood, from flowing. The positive $-\text{NH}_3^+$ groups on the skeleton of chitosan can interact with the negative charges on the surface of the red blood cells and platelets, accelerate their aggregation, and promote the hemostasis. Studies have also shown that the incorporation of chitosan into alginate fibers can significantly enhance the tensile properties of the dressing [110].

Liu et al. prepared several novel nonwoven hemostatic dressings composed of chitosan derivatives including carboxymethyl chitosan fiber, hydroxypropyl chitosan fiber, hydroxyethyl chitosan fiber, and carboxymethyl hydroxyethyl chitosan fiber. The dressing showed good biocompatibility, excellent tensile strength, and easy processing properties and had no antigenicity. Their study also demonstrated that the dressings promoted hemostasis and wound healing by forming a colloidal solution during the swelling and dissolving. Therefore, the dressings are especially suitable in the field of *in vivo* hemostasis [111].

Dressings prepared with cellulose have been widely applied in the surgical hemostasis because they can quickly stop bleeding and have a strong affinity for water and normal saline. The dressing absorbs water from blood and is dissolved to form a gel that plugs the capillary end to increase the viscosity of the blood and decelerate blood and thus stops bleeding. The hemostasis of cellulose dressing is based on mechanical press, erythrocyte absorption, and thrombocyte aggregation. Wang et al. prepared a soluble hemostatic fiber of carboxymethyl cellulose, which showed an excellent hemostatic performance in the clinical experiments [112]. Compared with gelatin sponge, the dressing was able to more effectively control bleeding of small blood vessels during the surgery, especially the blood infiltration of wound and suture. It is believed that the carboxymethyl cellulose fiber can accelerate platelet adhesion and reduce postoperative hematoma.

Niu et al. blended gelatin with lidocaine and PVA to produce nonwoven hemostatic materials. The produced dressing had a thin and dense network structure with numerous loose gaps that increased the contact area for the blood and thus promoted thrombocytes aggregation and the formation of clot and accelerated hemostasis [113]. PVA is a high expansion material having a high degree of hydrophilicity, which makes the dressing expand quickly to partially press the wound and stanch the bleeding [114].

4.3. Skin Regeneration. Nowadays, burn healing is one of the most significant problems of modern surgery because of the high lethality and disability after the treatment for burns of large surface area. Patients with burn injuries undergo significant emotional and physical pain and trauma from the burn, dressing changes, and the related treatments during the healing process [115]. In addition, fluid loss,

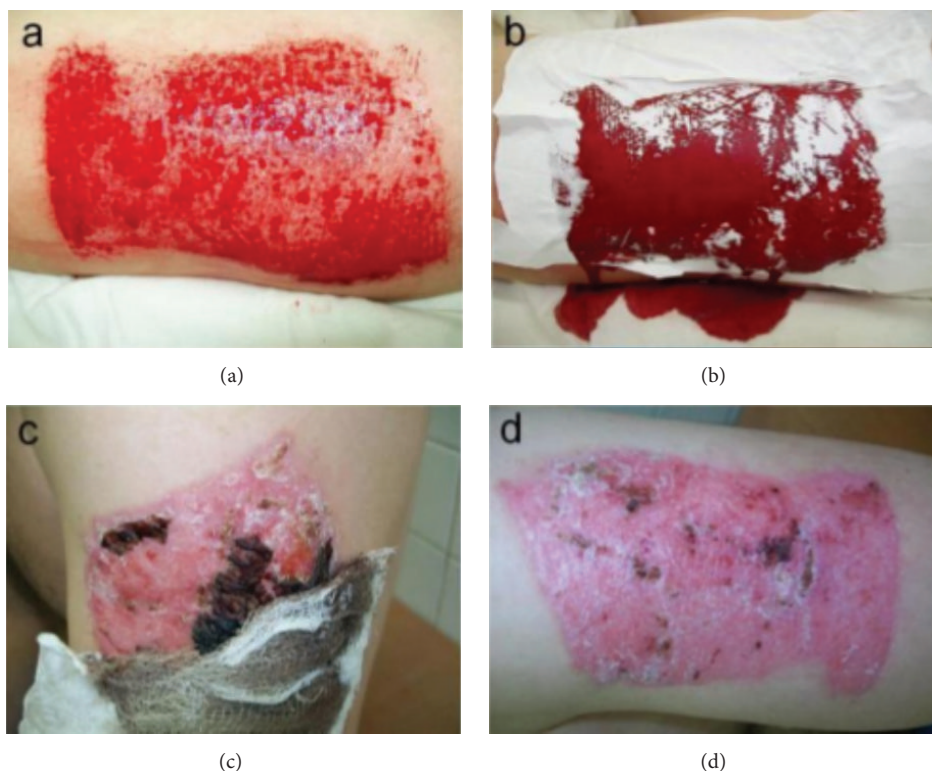


FIGURE 12: Donor wound: (a) before covering; (b) after covering; (c) 12 days after covering; and (d) 14 days after covering [121].

bacterial invasion, passive evaporative water, heat loss, and other complications can prevent wound from healing [116]. Therefore, the ideal burn dressing should have the following properties [117, 118]: (1) high exudate absorption capability, (2) ability to protect the wound from microorganisms, (3) being removable from the injured skin surface, (4) sufficient oxygen permeability, (5) high water vapor permeability, (6) nontoxicity, and (7) ability to accelerate scar formation. Covering large burned surfaces is still a challenge.

Fibrous wound dressing material is a promising candidate for skin regeneration. For example, Venugopal and Ramakrishna found that gelatin nanofibers could speed wound healing and could be used for cell transfer and skin regeneration [119]. Various blend fibers of renewable polymers, such as PEO/chitosan [120], PCL/collagen [119], PCL/gelatin [121], PLLA/chitosan [122], Zein/collagen [123], and PLLA/gelatin [124], are the dominate candidates.

The micro- and nanofibers of chitosan are an ideal candidate for burn dressing because of its high surface area to volume ratio [120]. The nanostructure of fibrous materials with small pore size functions as biological filters to effectively retain water and prevent infection from various bacteria. Kossovich et al. prepared a novel nanofiber dressing by blending chitosan with PEO through an electrospinning in glacial acetic acid. The clinical study indicates that the chitosan nanofiber dressing showed antibacterial properties and high absorption capacity and was able to effectively absorb exudate, ventilate wound, protect the wound from infection, and stimulate skin tissue regeneration. In addition, the

chitosan-based dressing showed excellent biodegradation, which avoided the mechanical damage to the wound from the wound dressing removal, reduced pain from dressing removal and change, and fastened rehabilitation [120]. Figure 12 shows that the wound dressing applied to the donor wound of transplant skin removal promoted skin regeneration by keeping a moist environment and removing the surplus of exudate without dressing change.

Venugopal et al. reported that composite fiber of collagen and PCL could support the growths of human dermal fibroblast and keratinocytes in skin engineering and the PCK film could not. They believe that cells migrated through pores in the fibers by amoeboid movement, pushing the surrounding fibers aside to expand. The dynamic architecture may provide cells with an opportunity to adjust the optimal pore diameter and grow into the scaffold. Chaisiri et al. prepared a skin tissue scaffold with composite fibers of gelatin and PCL to mimic the natural dermal ECM. The scaffold had a pore size of 40–70 micron and 98%–99% of porosity. In addition, it is biocompatible and can support cell migration and proliferation in its network [121].

4.4. Diabetic Ulcers. Diabetes mellitus is one of the most important public health problems worldwide because of its high prevalence and enormous social and economic consequences. It has been reported that there are more than 135 million diabetics in the world and the number is expected to increase to 300 million in the next 25 years [125].

Foot ulcers are a common, serious, and costly health issue for people with diabetes around the world. Two common chronic complications of diabetes mellitus including peripheral neuropathy and vascular insufficiency may lead to diabetic foot ulcers. Diabetic patients have a sharp decreased fibroblasts activity provoked by unavailability of glucose for aerobic metabolism, resulting in insufficient fibrous collagen tissue proliferation. Imbalance in these processes has been believed to be the main reason for the occurrence and persistence of this kind of disease. The wound healing process involves the interaction between various cellular groups, ECM, and growth factors, which is affected by the vascular insufficiency and severity of the lesion and infection.

Many renewable polymers, such as chitosan, alginate, cellulose, and silk, can be used to produce the dressings for the diabetic ulcers. Wang et al. developed a dressing composed of chitosan fibers, calcium alginate fibers, and chemically modified cellulose fibers and successfully used it to treat diabetic ulcers. In addition, epidermal growth factor (EGF) was incorporated into the renewable polymers to further promote the healing [126]. Schneider et al. prepared a silk mat with electrospun nanoscale silk fibers containing EGF, from which the EGF was slowly released in a time-dependent manner (25% EGF released in 170 h). Clinical study shows that the silk mat aided the healing by increasing time of wound closure by 90% by epidermal tongue, especially in chronic wounds including diabetic ulcers. Renewable polymers blended with metals can also show anti-inflammatory activity to accelerate the healing. Lázaro-Martínez reported a dressing of the blend of alginate fiber and hydrocolloid silver with excellent performances in decreasing inflammatory clinical signs and promoting healing on diabetic ulcers. The clinical study indicates that it reduced wound area with a median percentage of 47.7% and a mean percentage on the lesion of 58% at 2 weeks and 67.14% at 3 weeks. Wounds of all patients showed an obvious reduction in their size by 3-week treatment [127].

5. Conclusion

The nanofibers prepared from the renewable polymers can combine the excellent properties of the renewable polymers and nanofibers. They have become one of the most important materials used in wound dressing and attracted more and more attentions in recent years. The preparation methods, including electrospinning, bubbil spinning, centrifugal spinning, and freeze-drying, have been widely used to prepare the nanofibers from the renewable polymers. Particularly the wound dressings prepared from chitosan, cellulose, alginate, gelatin, hyaluronic acid, collagen, and silk fibroin or their composites have been widely used as the wound dressing to promote wound healing, hemostasis, skin regeneration, diabetic ulcers, tissue engineering, and so on. Many of the dressings have been used in clinic. But for many renewable polymers which originated from natural components, there are many factors which influence the structure and property of the polymers and they are hard to be controlled. Although their properties are versatile, many of the properties are less prominent. When the renewable polymers are prepared to

nanofibers and used for wound dressing, many of their properties, including antibacterial properties, hemostatic properties, biodegradability, cell adhesion and proliferation, and mechanical properties, need to be regulated by controlling the structure and properties of the nanofibers or compositing with other synthetic polymers to fit for the requirement of different wound. The above problems have become the future research keynotes for the nanofibers prepared from the renewable polymers.

Competing Interests

The authors declare that they have no competing interests.

Acknowledgments

This work was supported by the Youth Talent Plan of Beijing City, the Combination Project of Guangdong Province, and the “YangFan” Innovative Research Team Project of Guangdong Province.

References

- [1] P. Scarfato, L. Di Maio, and L. Incarnato, “Recent advances and migration issues in biodegradable polymers from renewable sources for food packaging,” *Journal of Applied Polymer Science*, vol. 132, no. 48, Article ID 42597, 2015.
- [2] L. Yu, K. Dean, and L. Li, “Polymer blends and composites from renewable resources,” *Progress in Polymer Science*, vol. 31, no. 6, pp. 576–602, 2006.
- [3] J. J. Blaker, K.-Y. Lee, and A. Bismarck, “Hierarchical composites made entirely from renewable resources,” *Journal of Biobased Materials and Bioenergy*, vol. 5, no. 1, pp. 1–16, 2011.
- [4] V. Pillay, C. Dott, Y. E. Choonara et al., “A review of the effect of processing variables on the fabrication of electrospun nanofibers for drug delivery applications,” *Journal of Nanomaterials*, vol. 2013, Article ID 789289, 22 pages, 2013.
- [5] R. Nayak, R. Padhye, I. L. Kyratzis, Y. B. Truong, and L. Arnold, “Recent advances in nanofibre fabrication techniques,” *Textile Research Journal*, vol. 82, no. 2, pp. 129–147, 2012.
- [6] Y. J. Li, F. Chen, J. Nie, and D. Z. Yang, “Electrospun poly(lactic acid)/chitosan core-shell structure nanofibers from homogeneous solution,” *Carbohydrate Polymers*, vol. 90, no. 4, pp. 1445–1451, 2012.
- [7] O. Ayaz, N. Ucar, E. Bahar et al., “Properties of composite nanofiber produced by single and coaxial nozzle method used for electrospinning technique,” *International Journal of Chemical and Biological Engineering*, vol. 6, pp. 52–56, 2012.
- [8] S. Agarwal, A. Greiner, and J. H. Wendorff, “Functional materials by electrospinning of polymers,” *Progress in Polymer Science*, vol. 38, no. 6, pp. 963–991, 2013.
- [9] Z. J. Yu, Y. H. Lin, W. W. Huang et al., “Multi spinnerets electrospinning with assistant sheath gas,” in *Proceedings of the 9th IEEE International Conference on Nano/Micro Engineered and Molecular Systems*, pp. 64–67, IEEE, Waikiki Beach, Hawaii, USA, April 2014.
- [10] I. G. Kim, J.-H. Lee, A. R. Unnithan, C.-H. Park, and C. S. Kim, “A comprehensive electric field analysis of cylinder-type multi-nozzle electrospinning system for mass production of

- nanofibers," *Journal of Industrial and Engineering Chemistry*, vol. 31, pp. 251–256, 2015.
- [11] A. Y. Nuryantini, M. M. Munir, M. P. Ekaputra, T. Suciati, and Khairurrijal, "Electrospinning of poly(vinyl alcohol)/chitosan via multi-nozzle spinneret and drum collector," *Advanced Materials Research*, vol. 896, pp. 41–44, 2014.
 - [12] N. Sasithorn and L. Martinová, "Fabrication of silk nanofibres with needle and roller electrospinning methods," *Journal of Nanomaterials*, vol. 2014, Article ID 947315, 9 pages, 2014.
 - [13] X. Wang, H. Niu, X. Wang, and T. Lin, "Needleless electrospinning of uniform nanofibers using spiral coil spinnerets," *Journal of Nanomaterials*, vol. 2012, Article ID 785920, 9 pages, 2012.
 - [14] R.-X. Chen, Y. Li, and J.-H. He, "Mini-review on Bubbfil spinning process for mass-production of nanofibers," *Revista Materia*, vol. 19, no. 4, Article ID 11560, pp. 325–344, 2014.
 - [15] J.-H. He, H.-Y. Kong, R.-R. Yang et al., "Review on fiber morphology obtained by bubble electrospinning and blown bubble spinning," *Thermal Science*, vol. 16, no. 5, pp. 1263–1279, 2012.
 - [16] Z.-B. Li, H.-Y. Liu, and H. Dou, "On air blowing direction in the blown bubble-spinning," *Revista Materia*, vol. 19, no. 4, pp. 345–349, 2014.
 - [17] J.-H. He and Y. Liu, "Control of bubble size and bubble number in bubble electrospinning," *Computers and Mathematics with Applications*, vol. 64, no. 5, pp. 1033–1035, 2012.
 - [18] G. J. Jiang, S. Zhang, Y. T. Wang, and X. H. Qin, "An improved free surface electrospinning with micro-bubble solution system for massive production of nanofibers," *Materials Letters*, vol. 144, pp. 22–25, 2015.
 - [19] H. Dou, B.-Q. Zuo, and J.-H. He, "Blown bubble-spinning for fabrication of superfine fibers," *Thermal Science*, vol. 16, no. 5, pp. 1465–1466, 2012.
 - [20] Y. Lu, Y. Li, S. Zhang et al., "Parameter study and characterization for polyacrylonitrile nanofibers fabricated via centrifugal spinning process," *European Polymer Journal*, vol. 49, no. 12, pp. 3834–3845, 2013.
 - [21] M. A. Hammami, M. Krifa, and O. Harzallah, "Centrifugal force spinning of PA6 nanofibers—processability and morphology of solution-spun fibers," *The Journal of the Textile Institute*, vol. 105, no. 6, pp. 637–647, 2014.
 - [22] A. E. Erickson, D. Edmondson, F.-C. Chang et al., "High-throughput and high-yield fabrication of uniaxially-aligned chitosan-based nanofibers by centrifugal electrospinning," *Carbohydrate Polymers*, vol. 134, Article ID 10199, pp. 467–474, 2015.
 - [23] J. Wu and J. C. Meredith, "Assembly of chitin nanofibers into porous biomimetic structures via freeze drying," *ACS Macro Letters*, vol. 3, no. 2, pp. 185–190, 2014.
 - [24] N. Salamian, S. Irani, M. Zandi, S. M. Saeed, and S. M. Atiyabi, "Cell attachment studies on electrospun nanofibrous PLGA and freeze-dried porous PLGA," *Nano Bulletin*, vol. 2, no. 1, Article ID 130103, 2013.
 - [25] G. Ma, Z. Wang, J. Chen, R. Yin, B. Chen, and J. Nie, "Freeze-dried chitosan-sodium hyaluronate polyelectrolyte complex fibers as tissue engineering scaffolds," *New Journal of Chemistry*, vol. 38, no. 3, pp. 1211–1217, 2014.
 - [26] M. Pakravan, M.-C. Heuzey, and A. Ajji, "A fundamental study of chitosan/PEO electrospinning," *Polymer*, vol. 52, no. 21, pp. 4813–4824, 2011.
 - [27] A. Sionkowska, "Current research on the blends of natural and synthetic polymers as new biomaterials: review," *Progress in Polymer Science*, vol. 36, no. 9, pp. 1254–1276, 2011.
 - [28] M. Dash, F. Chiellini, R. M. Ottenbrite, and E. Chiellini, "Chitosan—a versatile semi-synthetic polymer in biomedical applications," *Progress in Polymer Science*, vol. 36, no. 8, pp. 981–1014, 2011.
 - [29] K. Ohkawa, K.-I. Minato, G. Kumagai, S. Hayashi, and H. Yamamoto, "Chitosan nanofiber," *Biomacromolecules*, vol. 7, no. 11, pp. 3291–3294, 2006.
 - [30] V. Sencadas, D. M. Correia, A. Areias et al., "Determination of the parameters affecting electrospun chitosan fiber size distribution and morphology," *Carbohydrate Polymers*, vol. 87, no. 2, pp. 1295–1301, 2012.
 - [31] M. Z. Elsabee, H. F. Naguib, and R. E. Morsi, "Chitosan based nanofibers, review," *Materials Science and Engineering C*, vol. 32, no. 7, pp. 1711–1726, 2012.
 - [32] P. Su, C. J. Wang, X. Y. Yang et al., "Electrospinning of chitosan nanofibers: the favorable effect of metal ions," *Carbohydrate Polymers*, vol. 84, no. 1, pp. 239–246, 2011.
 - [33] A. A. Nada, R. James, N. B. Shelke et al., "A smart methodology to fabricate electrospun chitosan nanofiber matrices for regenerative engineering applications," *Polymers for Advanced Technologies*, vol. 25, no. 5, pp. 507–515, 2014.
 - [34] R. Zhao, X. Li, B. Sun et al., "Electrospun chitosan/sericin composite nanofibers with antibacterial property as potential wound dressings," *International Journal of Biological Macromolecules*, vol. 68, pp. 92–97, 2014.
 - [35] Y. H. Zhao, Y. Zhou, X. M. Wu, L. Wang, L. Xu, and S. C. Wei, "A facile method for electrospinning of Ag nanoparticles/poly(vinyl alcohol)/carboxymethyl-chitosan nanofibers," *Applied Surface Science*, vol. 258, no. 22, pp. 8867–8873, 2012.
 - [36] R. Liu, X. Xu, X. Zhuang, and B. Cheng, "Solution blowing of chitosan/PVA hydrogel nanofiber mats," *Carbohydrate Polymers*, vol. 101, no. 1, pp. 1116–1121, 2014.
 - [37] A. M. Abdelgawad, S. M. Hudson, and O. J. Rojas, "Antimicrobial wound dressing nanofiber mats from multicomponent (chitosan/silver-NPs/polyvinyl alcohol) systems," *Carbohydrate Polymers*, vol. 100, pp. 166–178, 2014.
 - [38] H. Y. Ma, C. Burger, B. S. Hsiao, and B. Chu, "Fabrication and characterization of cellulose nanofiber based thin-film nanofibrous composite membranes," *Journal of Membrane Science*, vol. 454, pp. 272–282, 2014.
 - [39] L. Fu, J. Zhang, and G. Yang, "Present status and applications of bacterial cellulose-based materials for skin tissue repair," *Carbohydrate Polymers*, vol. 92, no. 2, pp. 1432–1442, 2013.
 - [40] L. M. M. Costa, G. M. Olyveira, P. Basmaji, and L. X. Filho, "Nanopores structure in electrospun bacterial cellulose," *Journal of Biomaterials and Nanobiotechnology*, vol. 3, pp. 92–96, 2012.
 - [41] N. Shah, M. Ul-Islam, W. A. Khattak, and J. K. Park, "Overview of bacterial cellulose composites: a multipurpose advanced material," *Carbohydrate Polymers*, vol. 98, no. 2, pp. 1585–1598, 2013.
 - [42] P. Chen, Y. S. Yun, H. Bak, S. Y. Cho, and H.-J. Jin, "Multiwalled carbon nanotubes-embedded electrospun bacterial cellulose nanofibers," *Molecular Crystals and Liquid Crystals*, vol. 519, pp. 169–178, 2010.
 - [43] E. Omollo, C. Zhang, J. I. Mwasiagi, and S. Ncube, "Electrospinning cellulose acetate nanofibers and a study of their possible use in high-efficiency filtration," *Journal of Industrial Textiles*, 2014.
 - [44] A. Khalf, K. Singarapu, and S. V. Madihally, "Cellulose acetate core-shell structured electrospun fiber: fabrication and characterization," *Cellulose*, vol. 22, no. 2, pp. 1389–1400, 2015.

- [45] K. T. Shalumon, K. H. Anulekha, S. V. Nair, S. V. Nair, K. P. Chennazhi, and R. Jayakumar, "Sodium alginate/poly(vinyl alcohol)/nano ZnO composite nanofibers for antibacterial wound dressings," *International Journal of Biological Macromolecules*, vol. 49, no. 3, pp. 247–254, 2011.
- [46] N. Bhattarai and M. Zhang, "Controlled synthesis and structural stability of alginate-based nanofibers," *Nanotechnology*, vol. 18, no. 45, Article ID 455601, 2007.
- [47] S. A. Stone, P. Gosavi, T. J. Athauda, and R. R. Ozer, "In situ citric acid crosslinking of alginate/polyvinyl alcohol electrospun nanofibers," *Materials Letters*, vol. 112, pp. 32–35, 2013.
- [48] V. Leung, R. Hartwell, S. S. Elizei, H. J. Yang, A. Ghahary, and F. Ko, "Postelectrospinning modifications for alginate nanofiber-based wound dressings," *Journal of Biomedical Materials Research Part B Applied Biomaterials*, vol. 102, no. 3, pp. 508–515, 2014.
- [49] K. Y. Lee, L. Jeong, Y. O. Kang, S. J. Lee, and W. H. Park, "Electrospinning of polysaccharides for regenerative medicine," *Advanced Drug Delivery Reviews*, vol. 61, no. 12, pp. 1020–1032, 2009.
- [50] D. W. Fang, Y. Liu, S. Jiang, J. Nie, and G. P. Ma, "Effect of intermolecular interaction on electrospinning of sodium alginate," *Carbohydrate Polymers*, vol. 85, no. 1, pp. 276–279, 2011.
- [51] G. P. Ma, D. W. Fang, Y. Liu, X. D. Zhu, and J. Nie, "Electrospun sodium alginate/poly(ethylene oxide) core-shell nanofibers scaffolds potential for tissue engineering applications," *Carbohydrate Polymers*, vol. 87, no. 1, pp. 737–743, 2012.
- [52] S. A. Park, K. E. Park, and W. D. Kim, "Preparation of sodium alginate/poly(ethylene oxide) blend nanofibers with lecithin," *Macromolecular Research*, vol. 18, no. 9, pp. 891–896, 2010.
- [53] S. Safi, M. Morshed, S. A. H. Ravandi, and M. Ghiaci, "Study of electrospinning of sodium alginate, blended solutions of sodium alginate/poly(vinyl alcohol) and sodium alginate/poly(ethylene oxide)," *Journal of Applied Polymer Science*, vol. 104, no. 5, pp. 3245–3255, 2007.
- [54] V. M. Merkle, P. L. Tran, M. Hutchinson et al., "Core-shell PVA/gelatin electrospun nanofibers promote human umbilical vein endothelial cell and smooth muscle cell proliferation and migration," *Acta Biomaterialia*, vol. 27, pp. 77–87, 2015.
- [55] R.-Y. Tsai, S.-C. Hung, J.-Y. Lai, D.-M. Wang, and H.-J. Hsieh, "Electrospun chitosan-gelatin-polyvinyl alcohol hybrid nanofibrous mats: production and characterization," *Journal of the Taiwan Institute of Chemical Engineers*, vol. 45, no. 4, pp. 1975–1981, 2014.
- [56] M. Fallah, S. H. Bahrami, and R. M. Marziyeh, "Fabrication and characterization of PCL/gelatin/curcumin nanofibers and their antibacterial properties," *Journal of Industrial Textiles*, pp. 1–16, 2015.
- [57] K. Jalaja, P. R. A. Kumar, T. Dey, S. C. Kundu, and N. R. James, "Modified dextran cross-linked electrospun gelatin nanofibers for biomedical applications," *Carbohydrate Polymers*, vol. 114, pp. 467–475, 2014.
- [58] T. H. Nguyen and B. T. Lee, "Fabrication and characterization of cross-linked gelatin electro-spun nano-fibers," *Journal of Biomedical Science and Engineering*, vol. 3, no. 12, pp. 1117–1124, 2010.
- [59] Y. Z. Zhang, J. Venugopal, Z.-M. Huang, C. T. Lim, and S. Ramakrishna, "Crosslinking of the electrospun gelatin nanofibers," *Polymer*, vol. 47, no. 8, pp. 2911–2917, 2006.
- [60] J. H. Ko, H. Yin, J. An et al., "Characterization of cross-linked gelatin nanofibers through electrospinning," *Macromolecular Research*, vol. 18, no. 2, pp. 137–143, 2010.
- [61] Z.-M. Huang, Y. Z. Zhang, S. Ramakrishna, and C. T. Lim, "Electrospinning and mechanical characterization of gelatin nanofibers," *Polymer*, vol. 45, no. 15, pp. 5361–5368, 2004.
- [62] C. S. Ki, D. H. Baek, K. D. Gang, K. H. Lee, I. C. Um, and Y. H. Park, "Characterization of gelatin nanofiber prepared from gelatin-formic acid solution," *Polymer*, vol. 46, no. 14, pp. 5094–5102, 2005.
- [63] J.-H. Song, H.-E. Kim, and H.-W. Kim, "Production of electrospun gelatin nanofiber by water-based co-solvent approach," *Journal of Materials Science: Materials in Medicine*, vol. 19, no. 1, pp. 95–102, 2008.
- [64] K. Sisson, C. Zhang, M. C. Farach-Carson, D. B. Chase, and J. F. Rabolt, "Evaluation of cross-linking methods for electrospun gelatin on cell growth and viability," *Biomacromolecules*, vol. 10, no. 7, pp. 1675–1680, 2009.
- [65] W. P. Lu, M. Ma, H. T. Xu, B. Zhang, X. F. Cao, and Y. C. Guo, "Gelatin nanofibers prepared by spiral-electrospinning and cross-linked by vapor and liquid-phase glutaraldehyde," *Materials Letters*, vol. 140, pp. 1–4, 2015.
- [66] P. Slemming-Adamsen, J. Song, M. Dong, F. Besenbacher, and M. Chen, "In situ cross-linked PNIPAM/gelatin nanofibers for thermo-responsive drug release," *Macromolecular Materials and Engineering*, vol. 300, no. 12, pp. 1226–1231, 2015.
- [67] H. W. Kwak, M. J. Kang, J. H. Bae et al., "Fabrication of Phaeodactylum tricornutum extract-loaded gelatin nanofibrous mats exhibiting antimicrobial activity," *International Journal of Biological Macromolecules*, vol. 63, pp. 198–204, 2014.
- [68] Y.-H. Shan, L.-H. Peng, X. Liu, X. Chen, J. Xiong, and J.-Q. Gao, "Silk fibroin/gelatin electrospun nanofibrous dressing functionalized with astragaloside IV induces healing and anti-scar effects on burn wound," *International Journal of Pharmaceutics*, vol. 479, no. 2, pp. 291–301, 2015.
- [69] X. T. Han, Z. G. Xing, S. X. Si, Y. Y. Yao, and Q. Y. Zhang, "Electrospun grape seed polyphenols/gelatin composite fibers contained silver nanoparticles as biomaterials," *Fibers and Polymers*, vol. 15, no. 12, pp. 2572–2580, 2014.
- [70] E. K. Brenner, J. D. Schiffman, E. A. Thompson, L. J. Toth, and C. L. Schauer, "Electrospinning of hyaluronic acid nanofibers from aqueous ammonium solutions," *Carbohydrate Polymers*, vol. 87, no. 1, pp. 926–929, 2012.
- [71] C.-H. Chen, S.-H. Chen, K. T. Shalumon, and J.-P. Chen, "Dual functional core-sheath electrospun hyaluronic acid/polycaprolactone nanofibrous membranes embedded with silver nanoparticles for prevention of peritendinous adhesion," *Acta Biomaterialia*, vol. 26, pp. 225–235, 2015.
- [72] R. Uppal, G. N. Ramaswamy, C. Arnold, R. Goodband, and Y. Wang, "Hyaluronic acid nanofiber wound dressing—production, characterization, and in vivo behavior," *Journal of Biomedical Materials Research Part B: Applied Biomaterials*, vol. 97, no. 1, pp. 20–29, 2011.
- [73] Z. G. Chen, P. W. Wang, B. Wei, X. M. Mo, and F. Z. Cui, "Electrospun collagen-chitosan nanofiber: a biomimetic extracellular matrix for endothelial cell and smooth muscle cell," *Acta Biomaterialia*, vol. 6, no. 2, pp. 372–382, 2010.
- [74] K. S. Rho, L. Jeong, G. Lee et al., "Electrospinning of collagen nanofibers: effects on the behavior of normal human keratinocytes and early-stage wound healing," *Biomaterials*, vol. 27, no. 8, pp. 1452–1461, 2006.

- [75] S.-J. Liu, Y.-C. Kau, C.-Y. Chou, J.-K. Chen, R.-C. Wu, and W.-L. Yeh, "Electrospun PLGA/collagen nanofibrous membrane as early-stage wound dressing," *Journal of Membrane Science*, vol. 355, no. 1-2, pp. 53–59, 2010.
- [76] L. Huang, K. Nagapudi, P. R. Apkarian, and E. L. Chaikof, "Engineered collagen-PEO nanofibers and fabrics," *Journal of Biomaterials Science—Polymer Edition*, vol. 12, no. 9, pp. 979–993, 2001.
- [77] E. Schnell, K. Klinkhammer, S. Balzer et al., "Guidance of glial cell migration and axonal growth on electrospun nanofibers of poly- ϵ -caprolactone and a collagen/poly- ϵ -caprolactone blend," *Biomaterials*, vol. 28, no. 19, pp. 3012–3025, 2007.
- [78] J. S. Choi, S. J. Lee, G. J. Christ, A. Atala, and J. J. Yoo, "The influence of electrospun aligned poly(ϵ -caprolactone)/collagen nanofiber meshes on the formation of self-aligned skeletal muscle myotubes," *Biomaterials*, vol. 29, no. 19, pp. 2899–2906, 2008.
- [79] I. K. Kwon and T. Matsuda, "Co-electrospun nanofiber fabrics of poly (L-lactide-co- ϵ -caprolactone) with type I collagen or heparin," *Biomacromolecules*, vol. 6, no. 4, pp. 2096–2105, 2005.
- [80] J. Venugopal, S. Low, A. T. Choon, T. S. S. Kumar, and S. Ramakrishna, "Mineralization of osteoblasts with electrospun collagen/hydroxyapatite nanofibers," *Journal of Materials Science: Materials in Medicine*, vol. 19, no. 5, pp. 2039–2046, 2008.
- [81] J.-H. Song, H.-E. Kim, and H.-W. Kim, "Electrospun fibrous web of collagen-apatite precipitated nanocomposite for bone regeneration," *Journal of Materials Science: Materials in Medicine*, vol. 19, no. 8, pp. 2925–2932, 2008.
- [82] W. He, T. Yong, W. E. Teo, Z. Ma, and S. Ramakrishna, "Fabrication and endothelialization of collagen-blended biodegradable polymer nanofibers: potential vascular graft for blood vessel tissue engineering," *Tissue Engineering*, vol. 11, no. 9-10, pp. 1574–1588, 2005.
- [83] J.-P. Chen, G.-Y. Chang, and J.-K. Chen, "Electrospun collagen/chitosan nanofibrous membrane as wound dressing," *Colloids and Surfaces A: Physicochemical and Engineering Aspects*, vol. 313-314, pp. 183–188, 2008.
- [84] T. Liu, J. Xu, B. P. Chan, and S. Y. Chew, "Sustained release of neurotrophin-3 and chondroitinase ABC from electrospun collagen nanofiber scaffold for spinal cord injury repair," *Journal of Biomedical Materials Research Part A*, vol. 100, no. 1, pp. 236–242, 2011.
- [85] S. H. Kim, Y. S. Nam, T. S. Lee, and W. H. Park, "Silk fibroin nanofiber. Electrospinning, properties, and structure," *Polymer Journal*, vol. 35, no. 2, pp. 185–190, 2003.
- [86] L. Jeong, K. Y. Lee, J. W. Liu, and W. H. Park, "Time-resolved structural investigation of regenerated silk fibroin nanofibers treated with solvent vapor," *International Journal of Biological Macromolecules*, vol. 38, no. 2, pp. 140–144, 2006.
- [87] B.-M. Min, L. Jeong, K. Y. Lee, and W. H. Park, "Regenerated silk fibroin nanofibers: water vapor-induced structural changes and their effects on the behavior of normal human cells," *Macromolecular Bioscience*, vol. 6, no. 4, pp. 285–292, 2006.
- [88] L. Jeong, D. Cho, O. H. Kwon, B.-M. Min, and W. H. Park, "Cellular response of silk fibroin nanofibers containing silver nanoparticles *in vitro*," *Macromolecular Research*, vol. 22, no. 7, pp. 796–803, 2014.
- [89] S. Shahverdi, M. Hajimiri, M. A. Esfandiari et al., "Fabrication and structure analysis of poly(lactide-co-glycolic acid)/silk fibroin hybrid scaffold for wound dressing applications," *International Journal of Pharmaceutics*, vol. 473, no. 1-2, pp. 345–355, 2014.
- [90] S. Çalamak, C. Erdoğdu, M. Özalp, and K. Ulubayram, "Silk fibroin based antibacterial bionanotextiles as wound dressing materials," *Materials Science and Engineering C*, vol. 43, pp. 11–20, 2014.
- [91] J. Chutipakdeevong, U. Ruktanonchai, and P. Supaphol, "Hybrid biomimetic electrospun fibrous mats derived from poly(ϵ -caprolactone) and silk fibroin protein for wound dressing application," *Journal of Applied Polymer Science*, vol. 132, no. 11, Article ID 41653, 2015.
- [92] S. Calamak, E. A. Aksoy, C. Erdogdu, M. Sagioglu, and K. Ulubayram, "Silver nanoparticle containing silk fibroin bionanotextiles," *Journal of Nanoparticle Research*, vol. 17, no. 2, pp. 1–9, 2015.
- [93] K. Wei, Y. Li, K.-O. Kim et al., "Fabrication of nano-hydroxyapatite on electrospun silk fibroin nanofiber and their effects in osteoblastic behavior," *Journal of Biomedical Materials Research Part A*, vol. 97, no. 3, pp. 272–280, 2011.
- [94] C. S. Ki, E. H. Gang, I. C. Um, and Y. H. Park, "Nanofibrous membrane of wool keratose/silk fibroin blend for heavy metal ion adsorption," *Journal of Membrane Science*, vol. 302, no. 1-2, pp. 20–26, 2007.
- [95] C. S. Jiang and X. B. Chen, "Research process in the preparation of biomedical dressings by electrospinning," *Synthetic Fiber Industry*, vol. 35, no. 3, pp. 44–46, 2012.
- [96] T. T. T. Nguyen, C. Ghosh, S.-G. Hwang, L. D. Tran, and J. S. Park, "Characteristics of curcumin-loaded poly (lactic acid) nanofibers for wound healing," *Journal of Materials Science*, vol. 48, no. 20, pp. 7125–7133, 2013.
- [97] Y.-F. Goh, I. Shakir, and R. Hussain, "Electrospun fibers for tissue engineering, drug delivery, and wound dressing," *Journal of Materials Science*, vol. 48, no. 8, pp. 3027–3054, 2013.
- [98] T. Wu, "Absorbable composite dressing," China, CN102008740-A, CN102008740-B.
- [99] J. Fang, H. Niu, T. Lin, and X. Wang, "Applications of electrospun nanofibers," *Chinese Science Bulletin*, vol. 53, no. 15, pp. 2265–2286, 2008.
- [100] X.-F. Huang, J.-W. Jia, Z.-K. Wang, and Q.-L. Hu, "A novel chitosan-based sponge coated with self-assembled thrombin/tannic acid multilayer films as a hemostatic dressing," *Chinese Journal of Polymer Science*, vol. 33, no. 2, pp. 284–290, 2015.
- [101] C. Theisen, S. F. Winkelmann, K. Knappstein et al., "Influence of nanofibers on growth and gene expression of human tendon derived fibroblast," *BioMedical Engineering Online*, vol. 9, article 9, 2010.
- [102] M. Dubský, Š. Kubinová, J. Širc et al., "Nanofibers prepared by needleless electrospinning technology as scaffolds for wound healing," *Journal of Materials Science: Materials in Medicine*, vol. 23, no. 4, pp. 931–941, 2012.
- [103] M. A. de Moraes and M. M. Beppu, "Biocomposite membranes of sodium alginate and silk fibroin fibers for biomedical applications," *Journal of Applied Polymer Science*, vol. 130, no. 5, pp. 3451–3457, 2013.
- [104] Z. X. Zhou, X. L. Wei, J. R. Yao et al., "Evaluation of biological hemostatic dressings and gauzes in surgical wounds," *Journal of Clinical Rehabilitative Tissue Engineering Research*, vol. 14, no. 51, pp. 9635–9638, 2010.
- [105] P. Jiang, "Preparation of the PLLA from the fibrinogen and applications in the wound bleeding pig model," *Journal of Trauma and Emergency*, vol. 1, no. 4, p. 54, 2013.

- [106] X. Zhao, X. H. Cao, Y. Y. Ma et al., "Hemostatic effect of fibrin hemostatic dressing," *China Blood Transfusion*, vol. 23, no. 4, pp. 250–252, 2010.
- [107] K. Y. Baik, S. Y. Park, S. Namgung et al., "Synthetic nanowire/nanotube-based solid substrates for controlled cell growth," *Nano Convergence*, vol. 1, article 28, 2014.
- [108] T. Rajangam, H.-J. Paik, and S. S. A. An, "Development of fibrinogen microspheres as a biodegradable carrier for tissue engineering," *Biochip Journal*, vol. 5, no. 2, pp. 175–183, 2011.
- [109] R. G. Pillai and Z. A. Naieb, "Plastibell circumcision supported by a calcium-alginate fibre dressing to reduce bleeding," *Arab Journal of Urology*, vol. 13, no. 3, pp. 179–181, 2015.
- [110] B. Sibaja, E. Culbertson, P. Marshall et al., "Preparation of alginate-chitosan fibers with potential biomedical applications," *Carbohydrate Polymers*, vol. 134, pp. 598–608, 2015.
- [111] W. S. Liu, B. Q. Han, and Q. S. Gu, "Preparation method and application of the hemostasis and healing materials from the water soluble chitosan fibres," CN 200710015743.6, 2007.
- [112] H. M. Wang, J. Y. Pan, B. Yang, and K. X. Liu, "Animal test and clinical application of total soluble hemostatic fiber," *Journal of Clinical Pharmacology and Therapeutics in China*, vol. 11, no. 9, pp. s1017–s1020, 2006.
- [113] J. Z. Niu, B. P. Li, H. T. Lan, H. Wang, and K. Li, "Effect of lidocaine gelatin fiber net on the hemostatic and analgesic effect of endoscopic sinus surgery," *Chinese Journal of Primary Medicine and Pharmacy*, vol. 20, no. 12, pp. 1776–1777, 2013.
- [114] S. Liu, J. Z. Niu, H. J. Ge et al., "Clinical observation of the hemostatic effect of gelatin fiber net," *Journal of Chinese Trauma*, vol. 16, no. 3, p. 181, 2000.
- [115] D. A. Das, K. A. Grimmer, A. L. Sparnon, S. E. McRae, and B. H. Thomas, "The efficacy of playing a virtual game in modulating pain for children with a cuteburn injuries: a randomized controlled trial," *BMC Pediatrics*, vol. 5, article 1, 2005.
- [116] S. C. Sharma, M. M. Bagree, A. L. Bhat, B. B. Banga, and M. P. Singh, "Amniotic membrane is an effective burn dressing material," *The Japanese Journal of Surgery*, vol. 15, no. 2, pp. 140–143, 1985.
- [117] G. D. Mogoşanu and A. M. Grumezescu, "Natural and synthetic polymers for wounds and burns dressing," *International Journal of Pharmaceutics*, vol. 463, no. 2, pp. 127–136, 2014.
- [118] E. G. Kee, R. M. Kimble, L. Cuttle, and K. Stockton, "Comparison of three different dressings for partial thickness burns in children: study protocol for a randomised controlled trial," *Trials*, vol. 14, article 403, 8 pages, 2013.
- [119] J. Venugopal and S. Ramakrishna, "Applications of polymer nanofibers in biomedicine and biotechnology," *Applied Biochemistry and Biotechnology*, vol. 125, no. 3, pp. 147–157, 2005.
- [120] L. Y. Kossovich, Y. Salkovskiy, and I. V. Kirillova, "Electrospun chitosan nanofiber materials as burn dressing," in *Proceedings of the 6th World Congress of Biomechanics (WCB '10)*, C. T. Lim and J. C. H. Goh, Eds., vol. 31 of *IFMBE Proceedings*, pp. 1212–1214, Singapore, August 2010.
- [121] O. Chaisiri, N. Chanunpanich, and B. S. Hanpanich, "Polycaprolactone fibers gellation with gelatin ground substance: Engineered skin extracellular matrix aims for using as tissue engineering skin," in *The 15th International Conference on Biomedical Engineering: ICBME 2013, 4th to 7th December 2013, Singapore*, vol. 43 of *IFMBE Proceedings*, pp. 267–270, Springer, Berlin, Germany, 2014.
- [122] W. Hu, Z.-M. Huang, S.-Y. Meng, and C.-L. He, "Fabrication and characterization of chitosan coated braided PLLA wire using aligned electrospun fibers," *Journal of Materials Science: Materials in Medicine*, vol. 20, no. 11, pp. 2275–2284, 2009.
- [123] N. Alhusein, I. S. Blagbrough, M. L. Beeton, A. Bolhuis, and P. A. D. Bank, "Electrospun zein/PCL fibrous matrices release tetracycline in a controlled manner, killing *Staphylococcus aureus* both in biofilms and *ex vivo* on pig skin, and are compatible with human skin cells," *Pharmaceutical Research*, vol. 33, no. 1, pp. 237–246, 2016.
- [124] J.-B. Li, J. Han, and J. Ren, "Interaction of human fibroblasts with electrospun composites gelatin/PLLA, chitosan/PLLA and PLLA fibrous scaffolds," *Journal of Shanghai Jiaotong University (Science)*, vol. 17, no. 5, pp. 559–566, 2012.
- [125] J. C. Dumville, M. O. Soares, S. O'meara, and N. Cullum, "Systematic review and mixed treatment comparison: dressings to heal diabetic foot ulcers," *Diabetologia*, vol. 55, no. 7, pp. 1902–1910, 2012.
- [126] X. Wang, D. Zhang, and F. Shi, "Wound dressing useful for treating venous stasis ulcers and etc," China, WO2012092812-A1 CN102580135-A.
- [127] J. L. Lázaro-Martínez, A. Cecilia-Matilla, J. Aragón-Sánchez, E. García-Morales, Y. Garcia-Alvarez, and F. Alvaro-Afonso, "Treatment of infected diabetic foot ulcers clinical effectiveness of a dressing of alginate and hydrocolloid, with silver fiber. Analysis of results of a series of cases," *Revista de Enfermería*, vol. 36, no. 11, pp. 29–34, 2013.

Research Article

Utilization of Waste Clay from Boron Production in Bituminous Geosynthetic Barrier (GBR-B) Production as Landfill Liner

Müfide Banar,¹ Yücel Güney,² Aysun Özkan,¹ Zerrin Günkaya,¹
Eren Bayrakçı,³ and Derya Ulutaş⁴

¹Department of Environmental Engineering, Anadolu University, Iki Eylül Campus, 26555 Eskişehir, Turkey

²Anadolu University, Iki Eylül Campus, Research Institute of Earth and Space Sciences, 26555 Eskişehir, Turkey

³Department of Civil Engineering, Anadolu University, Iki Eylül Campus, 26555 Eskişehir, Turkey

⁴Department of Chemical Engineering, Anadolu University, Iki Eylül Campus, 26555 Eskişehir, Turkey

Correspondence should be addressed to Müfide Banar; mbaran@anadolu.edu.tr

Received 9 December 2015; Accepted 28 January 2016

Academic Editor: Matheus Poletto

Copyright © 2016 Müfide Banar et al. This is an open access article distributed under the Creative Commons Attribution License, which permits unrestricted use, distribution, and reproduction in any medium, provided the original work is properly cited.

Bituminous geomembranes, one type of geosynthetics, include a hot bituminous mixture with mineral filler and reinforcement. In this study, boron production waste clay (CW) was used as filler to produce a geosynthetic barrier with bentonite, waste tire, and bitumen. Bentonite and waste tires were used as auxiliary fillers and bitumen as the binder. CW/bitumen, CW/bentonite/bitumen, and CW/waste tire/bitumen mixtures were prepared by using a laboratory mixer at 100°C. Hot mixtures were extruded into strips by using a lab-scale corotating twin screw extruder ($L/D: 40$) followed by die casting (2 mm × 100 mm). Glass fleece or nonwoven polyester was used as reinforcement material and while die casting, both sides of the reinforcement materials were covered with bituminous mixture. Thickness, mass per unit area, tensile strength, elongation at yield, and hydraulic conductivity were used to characterize the geomembranes. Among all geomembranes, nonwoven polyester covered with 30% bitumen-70% boron waste clay mixture (PK-BTM30CW70) was found to be the most promising in terms of structure and mechanical behaviour. After that, consequences of its exposure to distilled water (DW), municipal solid waste landfill leachate (L-MSW), and hazardous waste landfill leachate (L-HW) were examined to use for an innovative impermeable liner on solid waste landfills.

1. Introduction

Geosynthetic barriers, also known as geomembranes, are defined as a nonporous homogeneous material, a relatively impermeable membrane, or barrier used in a geotechnical engineering application so as to control fluid migration from a man-made project, structure, or system. In the use of geomembranes as barriers to the transmission of fluids, it is important to recognize that it differs from other liner materials that are porous such as soils and concrete. The transmission of permeating species through geomembranes without holes occurs by absorption of the species in the geomembrane and diffusion through the geomembrane on a molecular basis [1]. Bituminous geomembranes (GBR-B) are mainly composed of a binder (the modified bitumen), a filler (mostly calcite mine is used industrially), and a reinforcement

(glass fleece or nonwoven polyester is preferred) as shown in Figure 1.

GBR-Bs are highly resistant to oxidation and UV rays without an antioxidant or stabilizer when compared to polymeric geomembranes (GBR-P). GBR-Ps are widely used in landfills as impermeable liner. Also the viscoelastic behavior of GBR-B allows self-repair of any defect that may occur with time such as strain, puncture, or fracture. Fillers are used in GBR-B with the intent of increasing stiffness and strength and also filling the voids in the hot mixture [2]. The filler is not only natural aggregates such as calcite, but also lime, lignin, sulfur, or ultrathin cut fiber particles which could pass number 200 (0.075 mm) sieve [3].

Turkey has 72% of the world's boron reserves and takes the first place with a reserve of 1.8 million tons. Eskişehir Eti Maden Kirka Boron Works has the largest boron reserve in

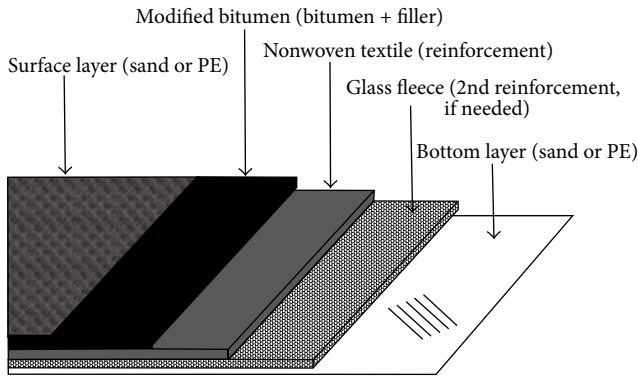


FIGURE 1: Bituminous geomembrane [1].

Turkey with 41% of the world's boron production. On the other hand, boron minerals have a strategic importance due to their wide range of uses in the manufacture of industrial products including glass, ceramic, textile, detergent, metallurgical, and fire-retardant materials. Thus, 900.000 tons of boron derivative waste are generated during 1 million-ton borax pentahydrate production [4]. Increasing amount of mining wastes, storage, stability, and safety of waste, and air, soil, and water pollution are major environmental issues [5]. Under the circumstances, developing novel products from the waste clay and investigating the utilization areas for waste clay become a necessity.

There have been studies related to utilization of the clay derivative waste and concentrated waste from boron concentrator facilities in various sectors such as cement [6–11], construction, brick and tile [12–20], and ceramic [21, 22]. Among these various studies, to our best knowledge, utilization of boron waste clay as a filler material has not been studied. Therefore, in this study, boron production waste clay (CW) was used as filler to produce a geosynthetic barrier with bentonite, waste tire (TW), and bitumen. Bentonite and waste tires were used as auxiliary fillers and bitumen was used as the binder.

2. Materials and Methods

2.1. Materials. Waste clay samples used in this study were collected from Eti Maden Kırka Boron Works in Eskisehir, Turkey. Basic geotechnical properties of the waste clay were given in Table 1. Grain-size distribution of CW consists of 1.74% sand, 20.76% silt, and 77.5% clay and the determined soil class is high plasticity clay (CH). CEC of the CW is 55 meq/100 g and this kind of high CEC values denotes that the clay is able to hold more contaminants. According to XRD, XRF, ICP-MS, and FT-IR results, dolomite is the most dominant compound in the CW followed by magnesium oxide, tincal, and quartz. The specific surface area of the CW is $5.12 \pm 0.1 \text{ m}^2/\text{g}$ by BET analysis method. The analyses methods and the details of the properties are available in our previous study [23].

Bitumen is used on the purpose to coalesce and unite the clay particles. The properties of bitumen (penetration

100/150 at 25°C, 100 g, 5 sec; softening point 39–47°C; flash point 230°C), the binder of the hot mixtures, were adopted from Turkish Petroleum Refineries Corporation (TÜPRAŞ), Turkey. Bentonite is generally used in improvement of impermeable compacted clay layers in landfills due to its high swelling potential and low hydraulic conductivity [24]. Bentonite was obtained from a bentonite plant. In this study, it is aimed at utilizing waste tires in landfill sites as a side material using boron waste clay. The particle size of the adopted waste tire samples was less than 1.18 mm. The steel free waste tire (<1.18 mm) was adopted from a tire recycling plant. Two different reinforcement materials were used, fiberglass tissue also known as glass fleece (CT) and nonwoven polyester (PK), and both were obtained from a geomembrane production plant.

2.2. Geomembrane Production. In the geomembrane production process, bitumen was firstly mixed with auxiliary fillers, bentonite or waste tire within a laboratory mixer at 100°C. After obtaining a homogenous mixture waste clay was added at certain amounts given in Table 2 and mixed for 45 minutes. In addition to geomembrane samples including bentonite or waste tire, neat samples including only CW were also prepared.

After mixing, hot mixtures were extruded into strips by using a lab-scale corotating twin screw extruder (L/D : 40) followed by die casting (2 mm × 100 mm). The temperatures of the various barrel elements were set in the ranges 100–130°C (bitumen introduction) and 38–52°C (extruder exit). Depending on the ingredients amount, the apparent fluidity of hot mixtures differed from each other. In order to obtain optimum product with stabile strip shape and no visible deformations such as puncture, tearing, or ruffle, different heating profiles were constituted for each mixture.

The extruded strips were then passed on a conveyor belt at a speed of 1 rpm. Two different reinforcement materials were used, fiberglass tissue also known as glass fleece (CT) and nonwoven polyester (PK). When the optimum profile was obtained, reinforcement material was placed on the binder mixture in strip shape and another layer of strip was placed on the reinforcement and pressed. Thus, both sides of the reinforcement material were covered with bituminous mixture (Figure 2).

2.3. Analyses Performed on GBR-B. According to the Turkish Standard of “TS EN 13493: Geosynthetic barriers-Characteristics required for use in the construction of solid waste storage and disposal sites,” thickness (TS EN 1849-1), mass per unit area (TS EN 1849-1), tensile strength (TS EN 12311-1), elongation at yield (TS EN 12311-1), and hydraulic conductivity (TS EN 14150) tests were applied to geomembranes with/without reinforcements to see the effect of reinforcements.

The tensile properties are the most critical mechanical properties of geomembranes since there are a range of tensile forces that can act on the geomembrane during installation and service. Also it is misleading to assume that if a geomembrane material has a high elongation at break, it

TABLE 1: Geotechnical properties of CW.

Water content, %	Specific weight, g/cm ³	Liquid limit, %	Plastic limit, %	Plasticity index, %	Optimum water content, %	Unconfined compressive strength, kg/cm ²	Hydraulic conductivity, m/s	Swelling potential, %
39.2	2.77	58	30	28	33	2.16	3.5×10^{-11}	10.4

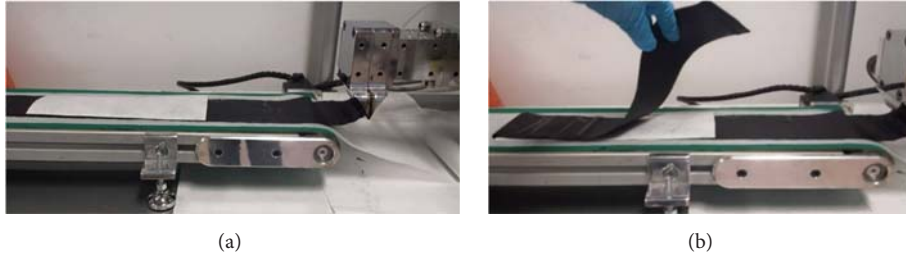


FIGURE 2: Geomembrane production with lab-scale extruder.

TABLE 2: BTM/CW, BTM/CW/BNT, and BTM/CW/TW specimens and proportions.

Specimen code	BTM, %	CW, %	BNT, %	TW, %
BTM30CW70	30	70	—	—
BTM40CW60	40	60	—	—
BTM50CW50	50	50	—	—
BTM40CW50BNT10	40	50	10	—
BTM40CW52BNT8	40	52	8	—
BTM40CW55BNT5	40	55	5	—
BTM40CW50TW10	40	50	—	10
BTM40CW52TW8	40	52	—	8
BTM40CW55TW5	40	55	—	5

BTM: bitumen; CW: waste clay; BNT: bentonite; TW: waste tire
All numbers in specimen codes represent the percentage of material at its left in the mixture.

has high survivability in service. Elongation at yield of the geomembrane should be investigated instead of elongation at break because after yield elongation point, deformation is irreversible. For instance, high density polyethylene (HDPE) has an elongation at break value of 700% but exhibits a distinct yield point at 12% strain [1]. According to the tensile and elongation properties, one of the BTM/CW, BTM/CW/BNT, and BTM/CW/TW geomembranes was selected to apply hydraulic conductivity test (Figure 3).

2.4. Exposure to Leachate. Leachate tests were applied to the most promising geomembrane sample determined by the analyses according to TS EN 13493. Geomembrane sample was exposed to distilled water (DW), municipal solid waste landfill leachate (L-MSW), and hazardous waste landfill leachate (L-HW). L-MSW was collected from a municipal solid waste landfill and L-HW was collected from İzmit Waste and Residue Treatment Incineration Recycling Co. (İZAYDAŞ). The test arrangement constituted for geomembranes exposure to leachate (Figure 4(a)) included a hydraulic conductivity test cell (Figure 4(b)) which was composed of

two parts (D : 50 mm) holding to each other by clamping for housing the geomembrane sample. In Figure 4(a), 1 bar of pressure was constantly applied on the leachate column to sustain the 1-bar fluid pressure in test cell. The plastic bottle on the bottom is placed for collecting leachate sample from the exit stream of the cell in case of any leaching occurrence. The leachate exposure test lasted for 35 days. SEM analysis was performed to examine the structural changes on the surface of geomembrane specimen due to exposure to leachates by using Phenom ProX SEM. Before the analysis, in order to prevent electrical charging, geomembrane was covered with gold for 40 seconds under the presence of Argon gas. During the analysis, 300, 500, and 1000x zoomed SEM images were obtained for each geomembrane and the appropriate 2 images in all 3 were chosen for consideration.

3. Results and Discussion

Results of thickness, mass per unit area, tensile strength, and elongation at yield analyses performed on geomembrane samples with/without reinforcement are given in Table 3. A commercial geomembrane was also tested in order to compare the results of produced geomembranes.

According to Table 3, geomembrane samples had thickness values between 2.5 and 3.7 mm. These thickness values are in the range of 2 to 5 mm given by the literature [1]. Produced samples had mass per unit area values between 3.6 and 5.4 kg/m². Geomembranes with mass per unit area above 0.5 kg/m² are considered as heavyweight membranes since this specification depends on density of the reinforcement and the filler [1].

Tensile strength of the geomembrane samples without reinforcements decreases with increasing bitumen content; in other words, tensile strength increases with increasing waste clay content.

Bentonite addition improved neither tensile strength nor elongation of geomembrane. At constant bitumen content, decreasing bentonite content and increasing waste clay



FIGURE 3: Hydraulic conductivity test arrangement.

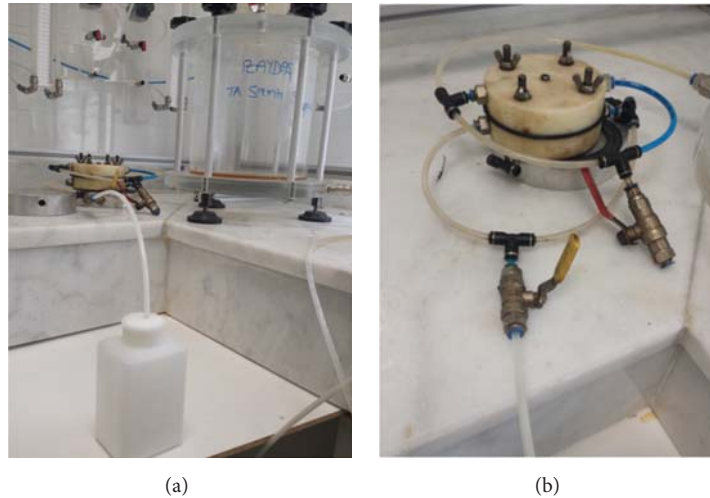


FIGURE 4: Leachate test arrangement: (a) leachate column; (b) test cell.

content affected tensile strength values of geomembrane negatively.

Waste tire addition improved tensile strength when bitumen/waste clay/waste tire mixtures were examined. At constant bitumen amount, tensile strength of the geomembrane increased with increasing waste tire amount. So with the intent of utilizing waste tires, waste tire could be used in geomembrane materials as modifier of bitumen.

Glass fleece reinforced geomembranes, in other words the CT-specimens, had relatively higher tensile strength values. However elongation values were in the range of 5–8% which was very low when compared to the commercial geomembrane.

The highest elongation belonged to PK-BTM30CW70 and PK-BTM50CW50, where nonwoven polyester reinforcement is already known to have a beneficial usage in geomembranes due to its high yield elongation. Tensile strength of PK-specimens was also higher than the commercial bituminous geomembrane. Therefore, PK (nonwoven polyester) was considered as the most appropriate reinforcement material. Since all specimens with PK had favorable tensile strength and elongation values, the one with highest waste clay content among BTM/CW, BTM/CW/BNT, and BTM/CW/TW groups was selected for hydraulic conductivity test application.

Hydraulic conductivity test was performed with PK-BTM30CW70, PK-BTM40CW55BNT5, and PK-BTM40CW55TW5. The hydraulic conductivity test results were 3.6×10^{-6} , 2.2×10^{-5} , and $1.0 \times 10^{-5} \text{ m}^3/\text{m}^2/\text{day}$, respectively, while the hydraulic conductivity of commercial geomembrane was $10^{-6} \text{ m}^3/\text{m}^2/\text{day}$. PK-BTM30CW70 had the closest value to commercial geomembranes' value; hence leachate exposure tests were performed with only that specimen.

3.1. Exposure to Leachate Results. Leachate exposure tests were carried on with PK-BTM30CW70 for 35 days. Meanwhile, leaching of any water sample through geomembrane was not observed; the outlet tubes and sample bottles were both empty at the end of the experiment. This result was a proof of considerably low hydraulic conductivity of the produced geomembrane. SEM analysis was performed on uncured geomembrane (Figure 5) and geomembrane samples exposed to DW (Figure 6), L-MSW (Figure 7), and L-HW (Figure 8).

SEM images of uncured geomembrane show a solid structure without any scratch, puncture, or gaps. Here, waste clay seems to be distributed homogeneously in the mixture and size of waste clay particles is in the range of 10–20 μm .

TABLE 3: Physical properties of all specimens and constituents.

Reinforcement state	Specimen	Thickness (mm)	Mass per unit area (kg/m ²)	Tensile force (kN)	Elongation (%)
Without reinforcement	BTM30CW70	1.4	2.2	0.0033	20
	BTM40CW60	1.3	2.0	0.0022	20
	BTM50CW50	1.2	1.8	0.0010	20
	BTM40CW50BNT10	1.4	2.3	0.0010	20
	BTM40CW52BNT8	1.4	2.5	0.0012	20
	BTM40CW55BNT5	1.5	2.7	0.0013	20
	BTM40CW50TW10	1.5	2.3	0.0029	50
	BTM40CW52TW8	1.5	2.5	0.0022	30
	BTM40CW55TW5	1.7	2.6	0.0022	32
With reinforcement					
Glass fleece	Glass fleece	0.25	0.044	0.1045	1.4
	CT-BTM30CW70	3.2	4.4	0.5152	7
	CT-BTM40CW60	2.7	4.0	0.6386	7
	CT-BTM50CW50	2.8	3.6	0.4606	7
	CT-BTM40CW50BNT10	3.0	5.4	0.5520	7
	CT-BTM40CW52BNT8	3.1	4.9	0.5735	8
	CT-BTM40CW55BNT5	3.2	4.6	0.6000	7
	CT-BTM40CW50TW10	3.2	4.6	0.3104	5
	CT-BTM40CW52TW8	3.7	5.0	0.5606	7
	CT-BTM40CW55TW5	3.6	5.2	0.4860	7
Nonwoven polyester	Nonwoven polyester	0.5	0.148	0.3885	40
	PK-BTM30CW70	3.2	4.5	0.4928	68
	PK-BTM40CW60	2.5	4.1	0.4213	57
	PK-BTM50CW50	3.0	3.7	0.4830	68
	PK-BTM40CW50BNT10	3.1	4.7	0.4061	53
	PK-BTM40CW52BNT8	3.4	5.0	0.4624	62
	PK-BTM40CW55BNT5	3.4	5.5	0.4964	67
	PK-BTM40CW50TW10	3.2	4.7	0.5088	35
	PK-BTM40CW52TW8	3.5	5.1	0.4935	59
	PK-BTM40CW55TW5	3.6	5.3	0.4986	59
Commercial geomembrane		3.2	3.6	0.4032	75

BTM: bitumen; CW: waste clay; BNT: bentonite; TW: waste tire; PK: nonwoven polyester; CT: glass fleece
 All numbers in specimen codes represent the percentage of material at its left in the mixture.

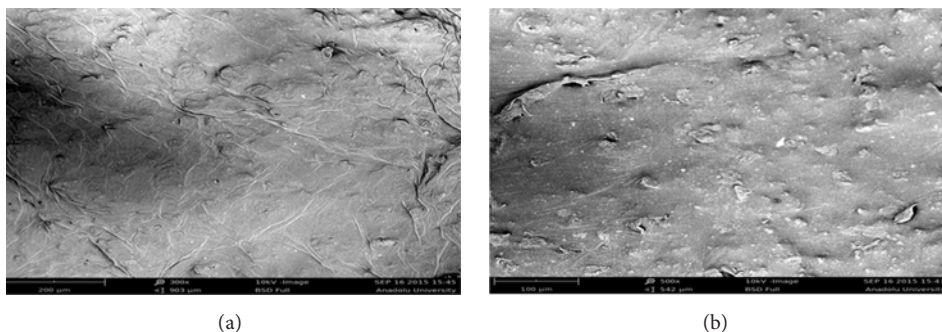


FIGURE 5: SEM images of uncured PK-BTM30CW70: (a) 300x; (b) 500x.

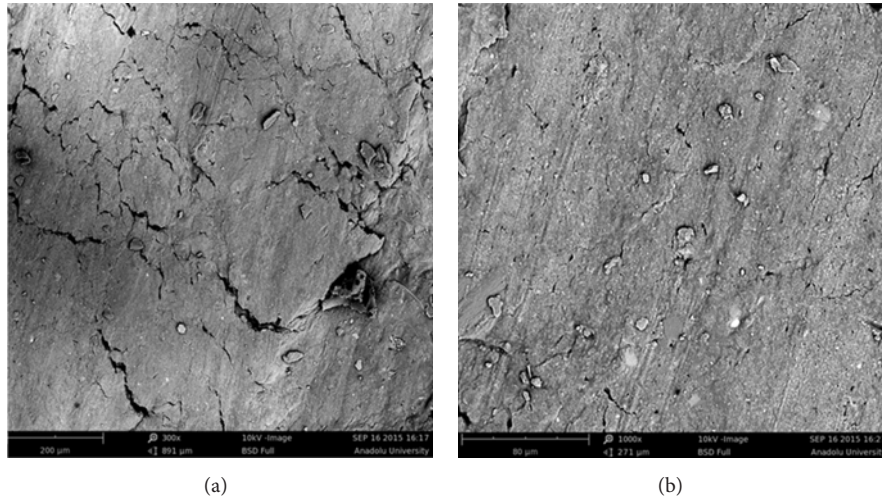


FIGURE 6: SEM images of PK-BTM30CW70 exposed to DW: (a) 300x; (b) 1000x.

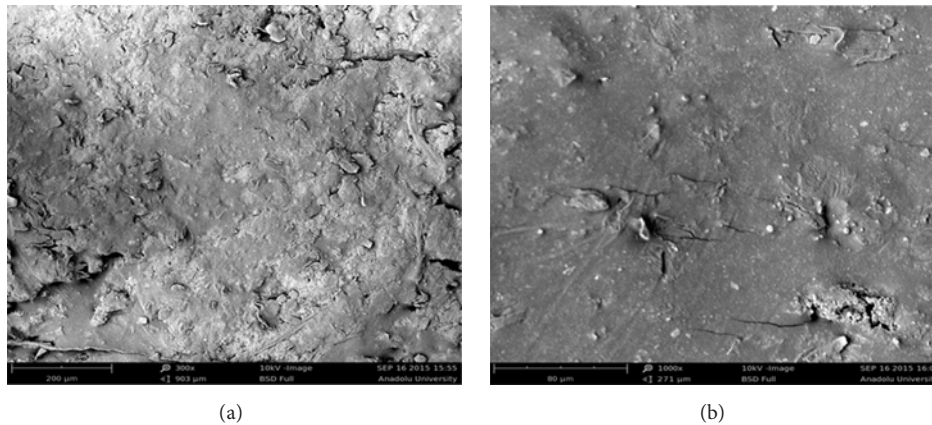


FIGURE 7: SEM images of PK-BTM30CW70 exposed to L-MSW: (a) 300x; (b) 1000x.

Geomembrane sample exposed to distilled water had some scratches with maximum length of $200\ \mu\text{m}$ and a small amount of waste clay was released from the bitumen and reached the surface. Geomembrane exposed to L-MSW had $200\ \mu\text{m}$ scratches and also fractional punctures with the length range $10\text{--}20\ \mu\text{m}$. Geomembrane exposed to L-HW had a relatively more defective image with punctures at length of $20\text{--}50\ \mu\text{m}$. Clay particles that reached surface were observed more in those images. The punctures are claimed to be a result of a certain amount of waste clay released from the bitumen when the geomembrane gets in contact with any kind of water. However those defects were limitative on the top surface of the geomembrane. Additionally, any effect on the bottom was not expected since no leaching was observed.

4. Conclusion

In this study, waste clay generated during boron derivatives production was mixed with bitumen, bentonite, and waste tire and these mixtures were used to cover up reinforcement materials (nonwoven polyester and glass fleece). Among all

produced geomembrane samples, according to thickness, mass per unit area, tensile strength, and elongation results, the samples were eliminated by comparing to a commercial geomembrane and only three samples (PK-BTM30CW70 (nonwoven polyester, 30% bitumen, 70% waste clay), PK-BTM40CW55TW5 (nonwoven polyester, 40% bitumen, 55% waste clay, and 5% waste tire), and PK-BTM40CW55B5 (nonwoven polyester, 40% bitumen, 55% waste clay, and 5% bentonite)) were used to apply hydraulic conductivity test. PK-BTM30CW70 was determined as the optimum geomembrane with the lowest hydraulic conductivity. Therefore leachate exposure tests were performed with PK-BTM30CW70 and distilled water, municipal solid waste leachate, and hazardous waste leachate. During the experiments, leaching did not occur, but SEM analysis comparison of geomembranes exposed to leachate showed increasing defectives such as scratches and punctures. Those structural defects did not affect the impermeability of geomembrane.

In terms of tensile strength, elongation, and hydraulic conductivity, boron waste clay could be used in geomembrane production instead of calcite in order to lower the cost

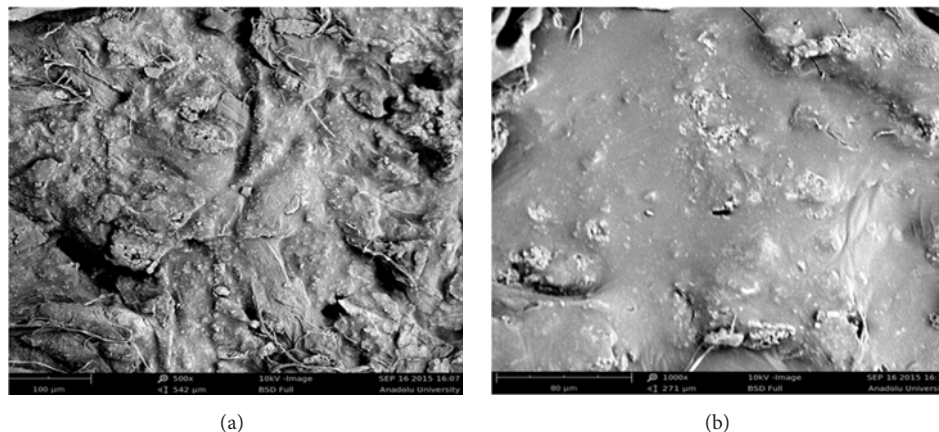


FIGURE 8: SEM images of PK-BTM30CW70 exposed to L-HW: (a) 500x; (b) 1000x.

while leading up to utilize waste clay of 900,000 tons/year generated at boron enterprises in Turkey. The optimum geomembrane produced is appropriate to use in landfills in means of the applied test results. As a conclusion, this study has an importance from the point of sustainable waste management principles with its aim to produce an innovative material by using waste materials.

Conflict of Interests

The authors declare that there is no conflict of interests regarding the publication of this paper.

Acknowledgments

This study was supported by TUBITAK (the Scientific and Technological Research Council of Turkey) under Grant no. 113Y122 and Anadolu University Scientific Research Projects Commission under Grant no. 1301F037.

References

- [1] J. Scheirs, *A Guide to Polymeric Geomembranes*, Wiley Series in Polymer Sciences, John Wiley & Sons, Hoboken, NJ, USA, 2009.
- [2] A. Geçkil, *Effect of graine tires on low temperature and elasticity behavior of bitumen and hot bitumen mixtures [M.S. thesis]*, Firat University, Elâzığ, Turkey, 2013 (Turkish).
- [3] V. Antunes, A. C. Freire, L. Quaresma, and R. Micaelo, "Influence of the geometrical and physical properties of filler in the filler-bitumen interaction," *Construction and Building Materials*, vol. 76, pp. 322–329, 2015.
- [4] "Eti Mine works general management," Boron Sector Report, Technical Report, 2010, (in Turkish).
- [5] M. Karadeniz, *Mineral Enrichment Tests Residue Environmental Effects/Precautions*, Directorate of Mineral Research and Exploration, Department of Mineral Analysis and Technology, 1996 (Turkish).
- [6] İ. Kula, A. Olgun, V. Sevinc, and Y. Erdogan, "An investigation on the use of tincal ore waste, fly ash, and coal bottom ash as Portland cement replacement materials," *Cement and Concrete Research*, vol. 32, no. 2, pp. 227–232, 2002.
- [7] M. Özdemir and N. U. Öztürk, "Utilization of clay wastes containing boron as cement additives," *Cement and Concrete Research*, vol. 33, no. 10, pp. 1659–1661, 2003.
- [8] R. Boncukçuoğlu, M. T. Yılmaz, M. M. Kocakerim, and V. Tosunoğlu, "Utilization of trommel sieve waste as an additive in Portland cement production," *Cement and Concrete Research*, vol. 32, no. 1, pp. 35–39, 2002.
- [9] Ş. Targan, Y. Erdoğan, A. Olgun, B. Zeybek, and V. Sevinç, "Utilization of clinker, bentonite and colemanite wastes in cement production," in *Proceedings of the 1st International Boron Symposium*, pp. 259–266, Kütahya, Turkey, October 2002.
- [10] M. E. Akbulut, *Examination of properties of boron waste added cement in third component conditions [M.S. thesis]*, Afyon Kocatepe University, Afyonkarahisar, Turkey, 2009 (Turkish).
- [11] A. Uğurlu, *Effect of waste generated at boron production usage with pozzolanic materials on cement production [Ph.D. thesis]*, Eskişehir Osmangazi University, Eskişehir, Turkey, 2009 (Turkish).
- [12] T. Kavas, "Use of boron waste as a fluxing agent in production of red mud brick," *Building and Environment*, vol. 41, no. 12, pp. 1779–1783, 2006.
- [13] İ. Demir and M. Orhan, "Utilization of boron waste in the production building materials," in *I. International Boron Symposium Proceedings Book*, pp. 235–239, Kütahya, Turkey, 2002.
- [14] N. Ediz and H. Yurdakul, "Utilization of waste generated at Etibor Kirka Borax Works DSM as filler in wall tile production," in *1st International Boron Symposium Proceedings Book*, pp. 246–249, Dumlupınar University, Kütahya, Turkey, 2002.
- [15] B. Karasu, G. Kaya, and H. Yurdakul, "Effect of the Etibor Kirka Borax Company's concentration and derivation wastes on the properties of wall tile body," in *Proceedings of the 1st International Boron Symposium*, pp. 224–228, Kütahya, Turkey, October 2002.
- [16] T. Kavas and G. Önce, "The usage capacity of Etibor Kirka Borax Company's wastes in the production of structural bricks as a flax material," in *Proceedings of the of the 1st International Boron Symposium*, pp. 219–223, Kütahya, Turkey, 2002.
- [17] Ö. F. Emrullahoğlu and C. B. Emrullahoğlu, "Effect of borax waste generated at Etibor Kirka on flor tile," in *I. International Boron Symposium Proceedings Book*, pp. 213–218, Kütahya, Turkey, 2004.
- [18] T. Uslu and A. I. Arol, "Use of boron waste as an additive in red bricks," *Waste Management*, vol. 24, no. 2, pp. 217–220, 2004.

- [19] S. Kurama, A. Kara, and H. Kurama, "Investigation of borax waste behaviour in tile production," *Journal of the European Ceramic Society*, vol. 27, no. 2-3, pp. 1715–1720, 2007.
- [20] T. Batar, S. Köksal, and E. Yersel, "Production of boron waste, waste paper and pearlite added plaster and its characterization," *Ekoloji*, vol. 72, pp. 45–53, 2009 (Turkish).
- [21] A. Christogerou, T. Kavas, Y. Pontikes, S. Koyas, Y. Tabak, and G. N. Angelopoulos, "Use of boron wastes in the production of heavy clay ceramics," *Ceramics International*, vol. 35, no. 1, pp. 447–452, 2009.
- [22] A. Olgun, Y. Erdogan, Y. Ayhan, and B. Zeybek, "Development of ceramic tiles from coal fly ash and tincal ore waste," *Ceramics International*, vol. 31, no. 1, pp. 153–158, 2005.
- [23] D. Ulutas, E. Bayrakci, Z. Cokaygil, A. Ozkan, Y. Guney, and M. Banar, "Geotechnical, chemical and structural characterization of waste clay from boron production," *Athens Journal of Technology Engineering*, vol. 1, no. 3, pp. 171–179, 2014.
- [24] M. H. Gleason, D. E. Daniel, and G. R. Eykholt, "Calcium and sodium bentonite for hydraulic containment applications," *Journal of Geotechnical Engineering*, vol. 123, no. 5, pp. 438–445, 1997.

Research Article

Influence of Fiber Content on Mechanical and Morphological Properties of Woven Kenaf Reinforced PVB Film Produced Using a Hot Press Technique

Suhad D. Salman,^{1,2} Z. Leman,¹ M. T. H. Sultan,³ M. R. Ishak,^{3,4} and F. Cardona³

¹Department of Mechanical and Manufacturing Engineering, Faculty of Engineering, Universiti Putra Malaysia, 43400 Serdang, Selangor, Malaysia

²Materials Engineering Department, Faculty of Engineering, Al-Mustansiriya University, Baghdad, Iraq

³Aerospace Manufacturing Research Centre (AMRC), Level 7, Tower Block, Faculty of Engineering, Universiti Putra Malaysia, 43400 Serdang, Selangor, Malaysia

⁴Laboratory of Bio-Composites Technology, Institute of Tropical Forestry and Forest Products (INTROP), Universiti Putra Malaysia (UPM), 43400 Serdang, Selangor, Malaysia

Correspondence should be addressed to Suhad D. Salman; suhaddawood2007@yahoo.com

Received 3 December 2015; Accepted 27 January 2016

Academic Editor: Heitor L. Ornaghi

Copyright © 2016 Suhad D. Salman et al. This is an open access article distributed under the Creative Commons Attribution License, which permits unrestricted use, distribution, and reproduction in any medium, provided the original work is properly cited.

This work addresses the results of experimental investigation carried out on mechanical and morphological properties of plain woven kenaf fiber reinforced PVB film which was prepared by hot press technique. The composites were prepared with various fiber contents: 0%, 10%, 20%, 30%, 40%, 50%, and 60% (by weight), with the processing parameters 165°C, 20 min, and at a pressure of 8 MPa applied on the material. Tensile, flexural, and Charpy impact properties were studied as well as morphological properties of impact fracture surface. With the increase in kenaf fibers content up to 40%, the PVB composites have shown lower tensile and flexural strength accompanied with reduction in the ultimate strain of the composite. The results showed that impact properties were affected in markedly different ways by using various kenaf contents and decrease with the increase in kenaf fiber content up to 40%; however, high impact strength was observed even with 40% kenaf fiber content. Furthermore, scanning electron microscopy for impact samples was utilised to demonstrate the different failures in the fracture surfaces for various kenaf fibers contents.

1. Introduction

Natural fiber composites are proposed to replace synthetic materials in many engineering applications due to several advantages such as renewability, less abrasiveness to equipment, biodegradability, and low weight and cost [1]. Kenaf fiber has been found to be an important source of fiber for composites due to its good properties and its contribution to environmental sustainability and eco-friendly products [2, 3].

In several studies, El-Shekeil et al. [4–6] have concentrated their efforts on the study of the natural fiber content effects on the behavior of composites. It was concluded that the fiber content strongly affects the overall properties of composites; 30% fiber loading displays the best tensile

strength, while the tensile modulus, thermal stability, hardness, and flexural strength increased with increase of fiber content, but the strain decreased. In other studies, Joseph et al. [7] and Ku et al. [8] described a remarkable increment of mechanical behaviors in the polymeric composites by increasing the natural fiber content.

Likewise, Ochi [9] and Nishino et al. [10] indicated that unidirectional kenaf/poly(lactic acid) composite at fiber loading of 70% has high tensile and flexural strength. It was concluded that the decline in tensile strength and Young's modulus increased with the increase of fiber loading with above 70 vol.%. This means fibers might not be fully saturated because of insufficient filling of the polymer amount. Similarly, Lee et al. [11] investigated the kenaf/polypropylene

composites fabricated with different fiber content, varying from 10% to 70% weight fraction with 10% increment. The results indicated that the tensile strength and modulus of kenaf/PP composites increased with increasing kenaf fiber contents, reaching a maximum value at 40%, and then decreased.

However, Hargitai et al. [12] indicated that the mechanical behaviors of the hemp/PP composites improved when the hemp fiber content increased, up to 50%, and reduced gradually at 70%. Shibata et al. [13] examined the flexural behavior of the kenaf fiber reinforced biodegradable resin composites and observed that flexural modulus increases with increase in kenaf loading irrespective of fiber orientation. This is in agreement with the findings of Liew [14] who found similar trends for oil palm fiber/polyester composites and concluded that the presence of 40% fiber content is the best. Rao et al. [15] studied experimentally the effect of banana fiber loading and other natural fibers reinforced polyester composites on mechanical behaviors of their composites.

More recently, a few attempts have been made to study the effect of processing method and polymer type relative to the physical and mechanical properties of composites based on kenaf fibers by Sharba et al. [16, 17]. From the results, it was concluded that kenaf fibers could be used as a potential reinforcing material, in order to decrease the use of synthetic fibers while taking advantage of natural resources.

However, the experimental results are different due to the properties of fibers and viscosity of matrix; therefore, the effect of fiber loading on the mechanical behavior of composites is one of the significant interests of many researchers. Even though many studies in the literature investigate the fiber loading effects on mechanical characterization, introducing new resin into the field of natural fiber composites gives more alternatives with a broad set of properties. Kenaf reinforced PVB film composites will open a new avenue for use in structural applications due to their remarkable properties, for example, in the automotive and aircraft industries. The objective of this research is to study the effect of fiber content on the mechanical performance of plain woven kenaf reinforced PVB composite.

2. Materials and Methods

To clarify the effect of fiber loading on the mechanical behavior of composites, plain woven kenaf and PVB film were utilised to fabricate the composites with different kenaf fiber loading. Plain woven kenaf was supplied by ZKK Sdn. Bhd., Malaysia, with the properties as reported in Table 1 and shown in Figure 1. PVB film (polyvinyl butyral resin) is now employed in a wide array of industrial processes and projected to ascertain a bright future for the new industry. The PVB tensile strength is ≥ 20 MPa and breaking elongation $\geq 200\%$ (manufacturer data sheet).

2.1. Fabrication of Composite Samples. The composite samples were made with 10%, 20%, 30%, 40%, 50%, and 60% kenaf fiber weight content by using a hot hydraulic press technique to reinforce PVB film. A detailed flow chart for

TABLE 1: Properties of woven kenaf [18].

Characterization	Woven kenaf
Thickness, t (mm)	2 ± 0.2
Weight (g/m^2)	890
Density (g/cm^3)	1.2
Warp density (warp/inch)	12
Weft density (weft/inch)	12
Wavelength, λ (mm)	4.2
Interyarn fabric porosity (ϵ)	0.274
Moisture content (%)	8.353
Water uptake (%)	148.86
Average breaking strength (MPa)	100.64
Average maximum strain (%)	17.3

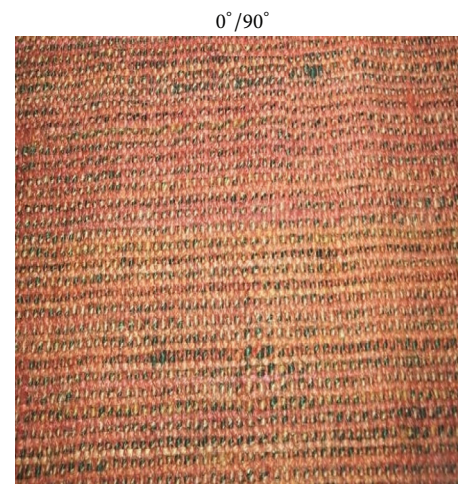


FIGURE 1: Kenaf fiber.

processing method is explained in Figure 2. Six panels with dimension 300 mm by 300 mm were fabricated and then cut by using a wheel saw machine, according to the ASTM standard of each test. For each panel, five layers of woven kenaf and six layers of PVB film are centered between two stainless-steel molds and hot plates of a compression moulding press. The hot press plates are heated to 165°C and the compression pressure is increased to 8 MPa and held constant for 15 min. Then, the platen temperature is reduced to room temperature (25°C), under pressure 8 MPa, until the temperature reaches 25°C . The panel was taken out of the compression molding frame and allowed to complete inner cure.

2.2. Mechanical Properties of Composites. The effect of fiber content on the tensile and flexural properties of woven kenaf/PVB composites was investigated in the composite laboratory of the Mechanical Department, Universiti Putra Malaysia, according to the ASTM D3039/D3039M-10 [19] and ASTM D790-10 [20]. The composites were categorized according to their fiber weight fractions (10%, 20%, 30%, 40%, and 50%). The test was carried out to determine the maximum tensile strength, maximum tensile strain, tensile

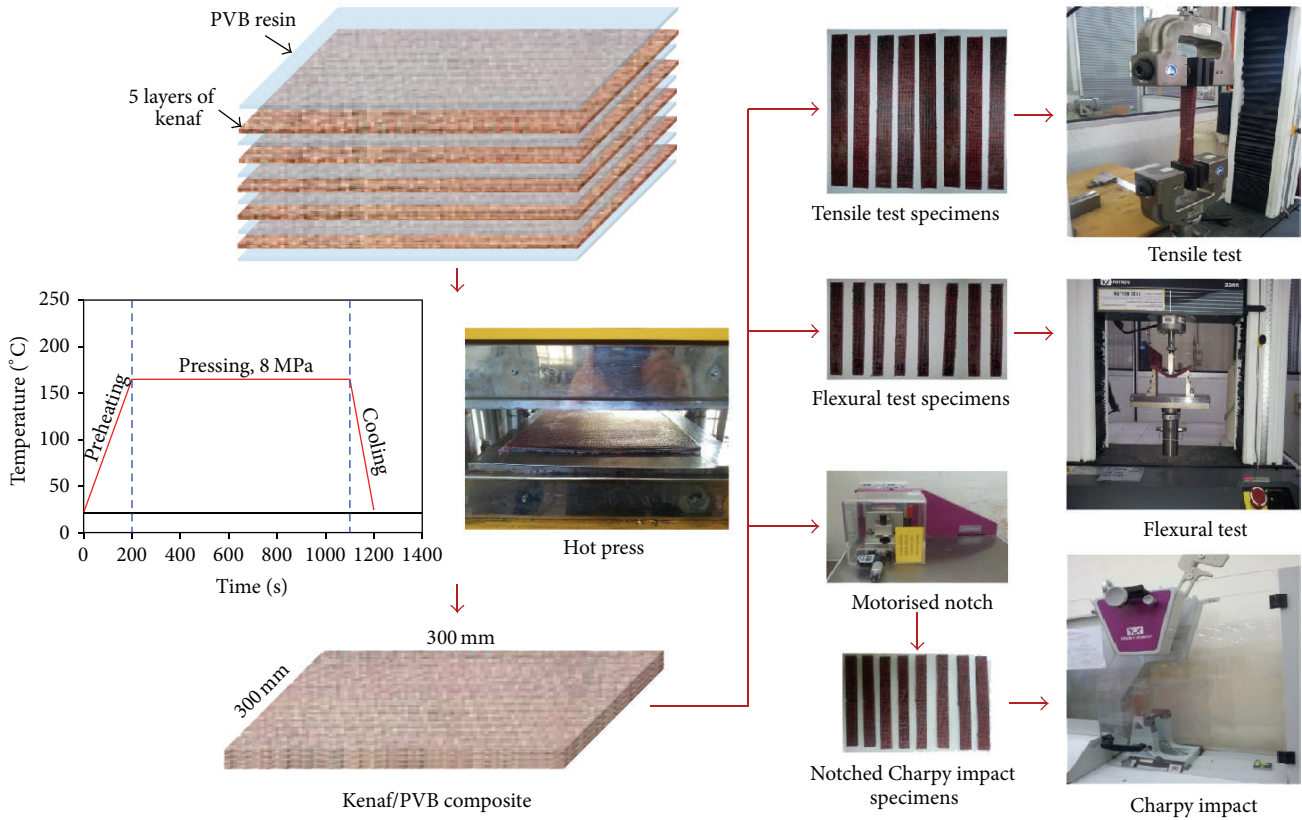


FIGURE 2: Drawing of the plain woven kenaf/PVB composite laminates by using the hot press technique and the temperature profile.

modulus, and stress-strain graphs, with crosshead speed of 1 mm/min. Tensile specimens were cut to 250 mm × 25 mm × actual thickness for each composite, rectangular sectional area flat strip (gage length of 170 mm). Four tabs plates with a dimension of 40 × 25 mm were attached to the two sides of both ends of the specimens by an adhesion agent.

The flexural tests were investigated using the three-point bending fixture with rectangular shape three-point bending specimens, 127 mm × 12.7 mm × actual thickness for each composite. The distance between the supports (span length) was calculated as per the standard, with a ratio of 16:1. The crosshead motion was calculated for each composite, according to

$$R = \frac{Z \times L^2}{6 \times d}, \quad (1)$$

where R is rate of crosshead motion (mm/min), L is support span (mm), d is depth of composite (mm), and Z is equal to 0.01.

The flexural modulus or bending modulus was calculated by drawing a tangent to the steepest initial straight-line portion of the stress-strain curve and using

$$E_b = \frac{L^3 m}{4bd^3}, \quad (2)$$

where E_b is the modulus of elasticity in bending (MPa), m is the slope of the tangent to the initial straight-line portion of

the load-deflection curve, (N/mm) of deflection, and b is the width of sample tested (mm).

Eight samples for each composite were tested and the average value of five specimen results was reported by using a universal testing machine (Instron 3365) with a capacity of 100 KN (for both tests).

The impact strength of the samples was measured using Charpy impact test machine, according to the ASTM D6110 [21]. The Charpy impact tests were conducted by using a universal testing machine, INSTRON, MECOMB, in the Laboratory of Bio-Composites Technology, Institute of Tropical Forestry and Forest Products (INTROP), Universiti Putra Malaysia. By using a wheel saw machine, the specimens were carefully cut and finished to the accurate size, 127 mm × 12.7 mm × actual thickness for different weight fraction and striking hammer energy (0.5, 2.7, 5.4, and 21.6 joules). All impact test samples were notched with the radius of curvature 0.25R mm to 2.54 mm by motorised Notchvis in the middle. Eight specimens for each composite and energy level were tested and the average value of five specimen results was reported.

2.3. Morphological Observation. The influence of the kenaf fiber content on the fractured surface of the composites after Charpy impact test was observed by using the scanning electron microscope (SEM) instrument model Hitachi 5.00 kV,

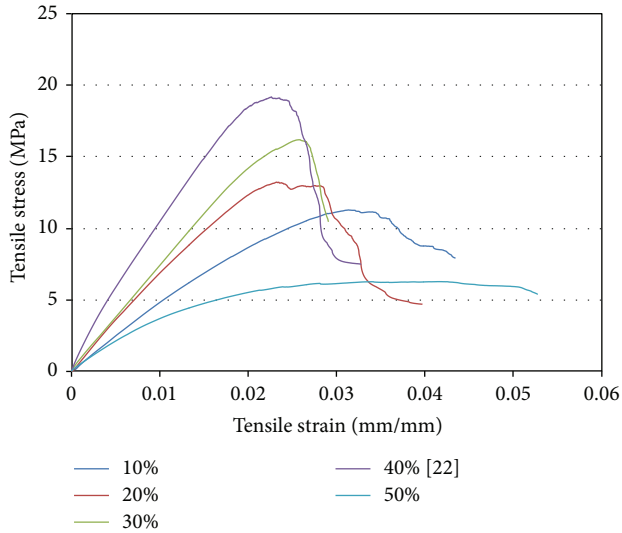


FIGURE 3: Average values of tensile stress-deformation diagram of different fiber content of kenaf/PVB composites.

after being coated with a thin layer of gold to avoid electron charge accumulation.

3. Results and Discussions

3.1. Tensile Test Results. Figure 3 shows that the stress-strain curve of kenaf/PVB film with different fiber content is linear and follows Hooke's law. It could be seen that the tensile strength increased linearly with the increase of the tensile strain and fiber content, reaching a maximum value at 50%. However, when it reaches certain stress values, nonlinear behavior is noticed, especially for the 10% and 50% fiber content. The average tensile strength is 11.28 MPa, 13.23 MPa, 16.19 MPa, 19.19 MPa, and 6.27 MPa for 10%, 20%, 30%, 40% [22], and 50% fiber content, respectively. The results indicated that failure takes place at a much lower strain rate at 30% and 40% kenaf fiber content. Meanwhile, the highest tensile strength was enhanced at 40% kenaf fiber content. The results indicated that the mechanical interlocking was sufficient to transfer the load from the PVB film to the kenaf fibers and the reinforcing effect of the kenaf fibers predominated, while at low kenaf fiber content, less fiber amount caused low load transfer capacity among the fibers, which led to accumulation of stress that occurred in the matrix which led to rapid failure of the composites. The low stress rate for 50% fiber content is attributed to two reasons. The first reason is the low tensile properties of PVB film, and the second one is the fact that the spacing between kenaf fibers becomes so small that the stress transfer between kenaf fiber and PVB resin becomes inefficient. As a result, a premature failure occurred due to increased shear stresses on all planes parallel to the axes of the fibers which led to delamination. It is stated by Kim et al. [23] that most highly polymeric materials tend to be stress rate dependent. It has been recorded that the strength of composites is influenced by several factors such as fiber content, fiber/matrix interfacial bonding, and fiber

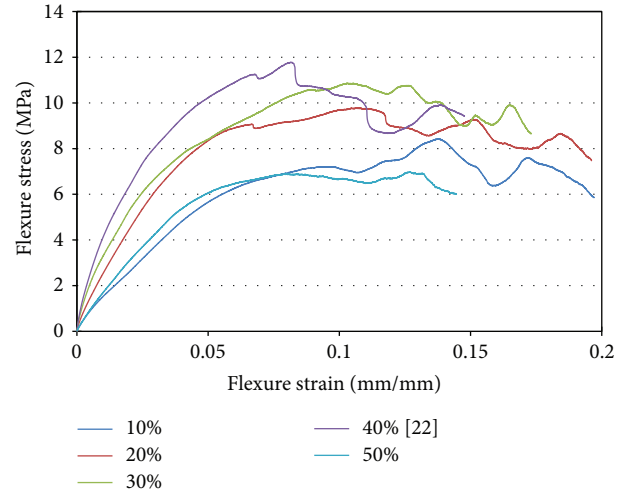


FIGURE 4: Effect of different kenaf fiber content on flexural properties of kenaf/PVB composites.

and matrix strength [24]. However, the fiber works as load carriers in the matrix, and high tensile strength depends more on effective and uniform stress distribution. Several researches have concluded that there is a practical maximum fiber content above which composite characteristics deteriorate [25, 26] and/or porosity increases highly [27]. Similar findings were also observed by Ku et al. [8], who reported that the increment of fiber loading above 40% causes the reduction in ultimate strength.

3.2. Flexural Test Results. Flexural characteristics represent the flexibility of the materials and good flexural strength indicates that the materials have brittle properties and high hardness [4]. Figure 4 shows the effect of different fiber content on the flexural properties of kenaf/PVB composites. Flexural strength behaved with a similar trend to tensile strength behavior; the 40% kenaf fiber content has the highest stress to resist deformation under flexural condition. As a result of good interfacial bonding between kenaf fiber and PVB film, the fibers are effectively participating in the stress transfer. Tensile, compression, and shear stresses caused the flexural failure that occurred at the two sides of the bending samples [28]. The average flexural strength is 8.4 MPa, 9.8 MPa, 10.8 MPa, 11.8 MPa, and 6.98 MPa for 10%, 20%, 30%, 40%, and 50% fiber content, respectively. A characteristic stepwise reduction in flexural stress was demonstrated with increasing both the strain of maximum flexural stress and up to 40% kenaf fiber content. Hence, the failure in flexural testing of the kenaf/PVB film is dominated by individual ply failure rather than any observable interlaminar failure. It can be concluded that 40% kenaf fiber content exhibited relatively high flexural strength; good kenaf fiber/PVB bonding offers an advantage over other composites. The comparatively lower flexural modulus of the 50% kenaf fiber content is due to using lower percentage of PVB film, which might lead to inefficient load transfer from fiber to matrix (weak fiber adhesion). As reported in

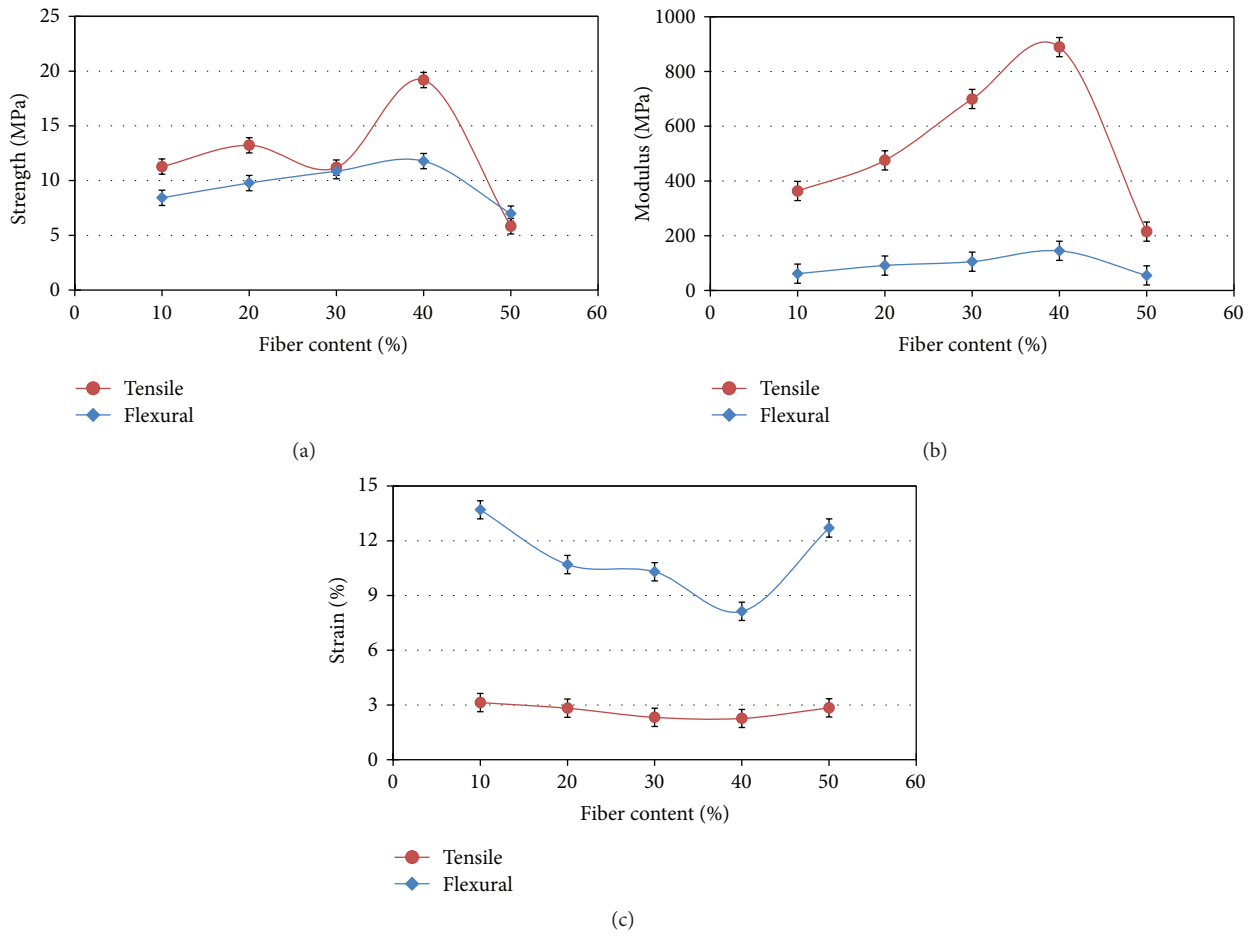


FIGURE 5: Comparison of (a) tensile and flexural strength with kenaf fiber content, (b) tensile and flexural modulus with kenaf fiber content, and (c) tensile and flexural strain with kenaf fiber content.

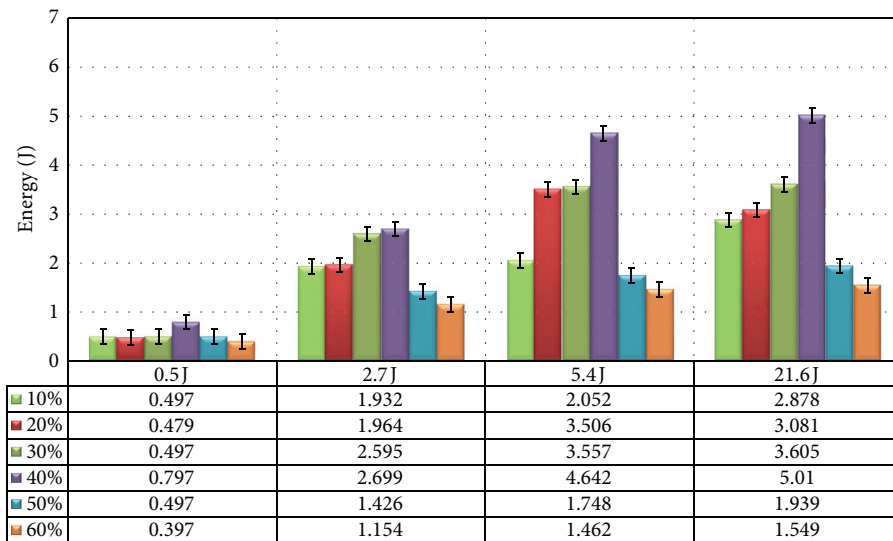


FIGURE 6: Effect of fiber content on impact energy of kenaf/PVB composites at different energy levels.

previous studies, the flexural strength increased at the 40% fibers content [13, 29], the stiffer and higher to resist any deformation.

Figures 5(a), 5(b), and 5(c) show the effects of fiber content on the average tensile and flexural strength, modulus, and strain of the kenaf fiber reinforced PVB composites, respectively. In Figure 5(a), it is noticed that the tensile and flexural strength are increasing gradually with increase in fiber content up to 40% kenaf content and then decreased. Similarly, de Albuquerque et al. [30] have reported the same trend on the Jute reinforced polyester composites. Figure 5(b) shows that the modulus increased with addition of fibers, reaching a maximum value at 40% kenaf content, and then reduced. As discussed earlier, a lower value for tensile and flexural modulus is predominantly seen for 50% kenaf content composites due to increased shear stresses on all planes parallel to the axes of the fibers. The tensile modulus is 363.5 MPa, 475.5 MPa, 699.4 MPa, 889.2 MPa, and 215.3 MPa for 10%, 20%, 30%, 40%, and 50% fiber content, respectively, while flexural modulus is 61.497 MPa, 91.4 MPa, 105.5 MPa, 144.9 MPa, and 54.98 MPa for 10%, 20%, 30%, 40%, and 50% fiber content, respectively. The tensile and flexural strain show an inverse relationship to strength and modulus. As illustrated in Figure 5(c), when kenaf fiber content was increased until 30%, failure took place at the lowest strain rate. It can be indicated that the strain is decreasing with increase in fiber content, up to 30% fiber content. The tensile strain is 3.13%, 2.82%, 2.32%, 2.26%, and 2.84% for 10%, 20%, 30%, 40%, and 50% fiber content, respectively. The value of the maximum tensile strain decreased slightly for 40%; nevertheless, flexural strain increased for 50% continuously (12.7%). In the 10% kenaf fiber content composite, insufficient fibers are mixed with large PVB matrix; thus, elongation will be high because it is high in the PVB matrix. At 30% kenaf fiber content composite, more kenaf fibers were there which could transfer stress properly along them, leading to less elongation. This prevents creating a crack propagation rate, thus causing the composite to break at a higher failure strain. Both fibers content and characteristics of individual reinforcing fibers are the main factors which have affected the variation in the modulus and failure strain of composites.

3.3. Impact Test Results. Figure 6 compares the energy absorption capability of the different kenaf fiber content under varied impact energies, 0.5 J, 2.7 J, 5.4 J, and 21.6 J, respectively. It showed the variation of the energy absorbed by the tested specimens under different energies levels. However, the Charpy impact energy of different kenaf content showed almost the same behavior when tested under the same energy level. It could be observed that there is an increase in the total energy absorption by the specimens up to 40% then a decrease was observed. The level of maximum impact energy reached for the 40% kenaf/PVB composite is the highest value at different energy levels. At low energy level, 0.5 J, there is not a significant difference in the absorbed energy that can be observed for the various kenaf fiber contents. However, when the energy level was increased, a high increment in the absorbed energy can be seen for kenaf/PVB composite

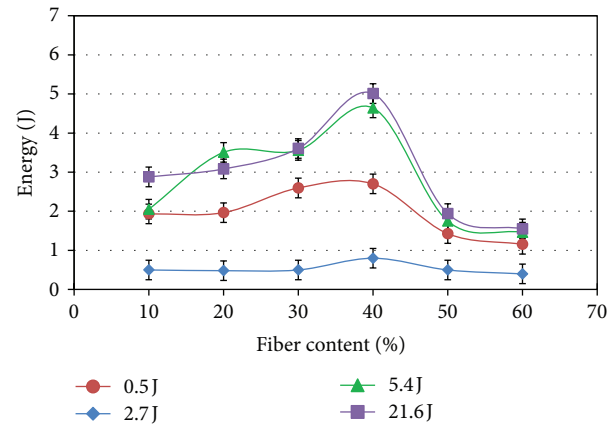


FIGURE 7: Effect of fiber content on impact energy of kenaf/PVB composites at different energy levels.

up to 40% kenaf fiber content, as shown in Figure 7. Then, the energy absorbed is decreased at 50% and 60% kenaf fiber content, at different energy levels. Due to the lower percentage of resin, both intralayer failures and delamination affect the total absorbed energy values at these kenaf fiber contents, which is found to change the failure mechanism of the composites [31]. However, the amount and the type of failure mechanism depend on the impact energy level and mechanical properties of fiber and matrix [32].

A similar finding was also observed in the average impact strength of the kenaf/PVB composites with different kenaf content and energy levels, as shown in Figure 8. It was clear that, for the composite specimens with 40% kenaf fiber content, higher values of impact strength were recorded compared with the other composites, at different energy levels. This is attributed to the fact that the increase of fiber content above 40% causes lack of energy absorbance. It could be attributed to the increase of the stiffness of the composite by increase of fiber content to reinforced thermoplastics, as reported by Joffe and Andersons [33]. Generally, it can be seen that the impact energy strongly depends on the percentage of the fiber content, especially when combining natural fibers with thermoplastics [34, 35], as shown in Figure 9. Further, low interface shear stress between natural fiber and polymer resin might contribute to the increase in the composite strength. The incorporation of lignocellulosic fibers offers an obstacle to the propagation of an initial crack at the specimen notch and then causes other cracks at the weak fiber/matrix interface to propagate longitudinally through the interface following the specimen length direction. Likewise, Wirawan et al. [36] have reported that higher absorbed impact energy resulting in corresponding higher strength of sugarcane reinforced PVC thermoplastic.

Similarly, the Charpy impact toughness seems to have the same impact energy and impact strength behaviors at different energy levels, as represented in Figures 10 and 11. It is clearly seen that the composite materials with 40% kenaf fiber content have the greatest impact toughness value, at different

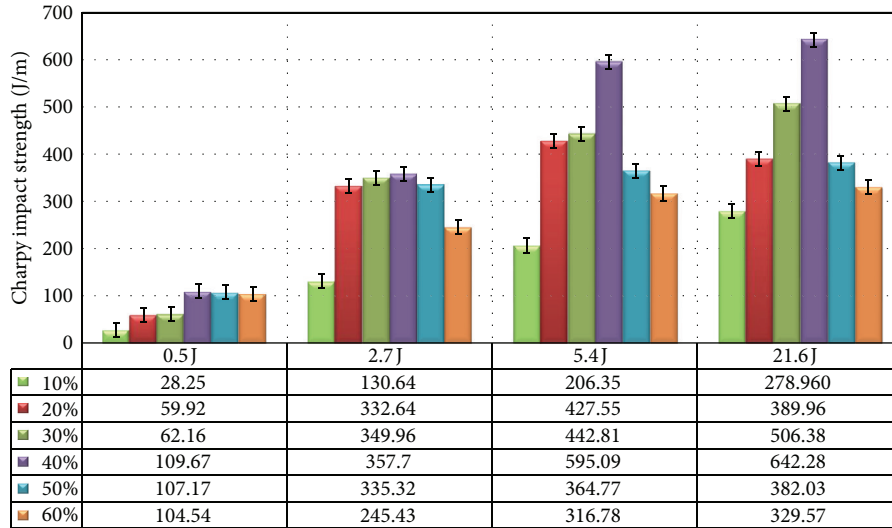


FIGURE 8: Effect of fiber content on impact strength of kenaf/PVB composites at different energy levels.

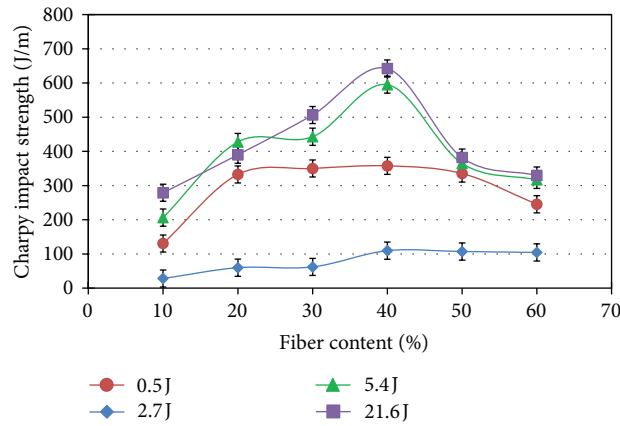


FIGURE 9: Effect of fiber content on impact strength of kenaf/PVB composites.

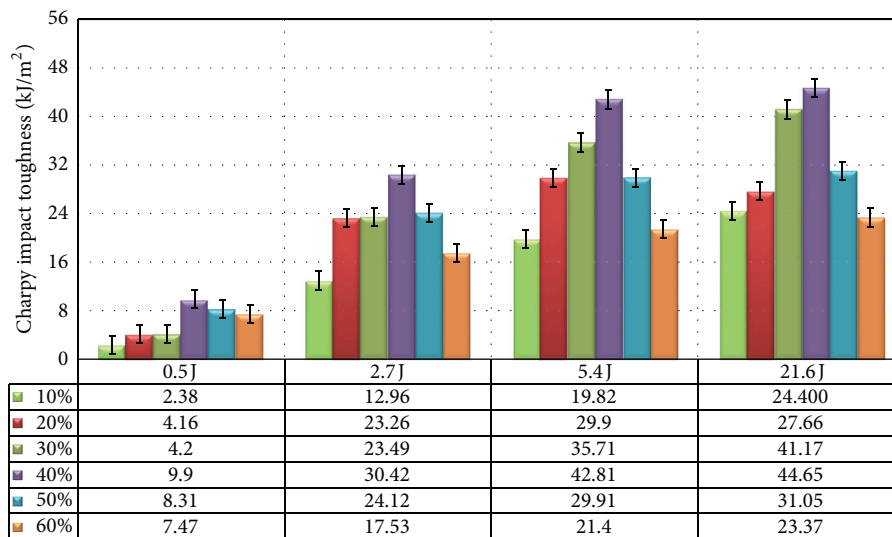


FIGURE 10: Effect of fiber content on impact toughness of kenaf/PVB composites at different energy levels.

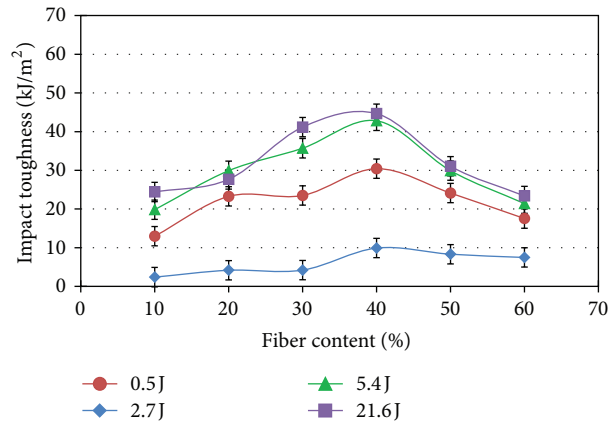


FIGURE 11: Effect of fiber content on impact toughness of kenaf/PVB composites.

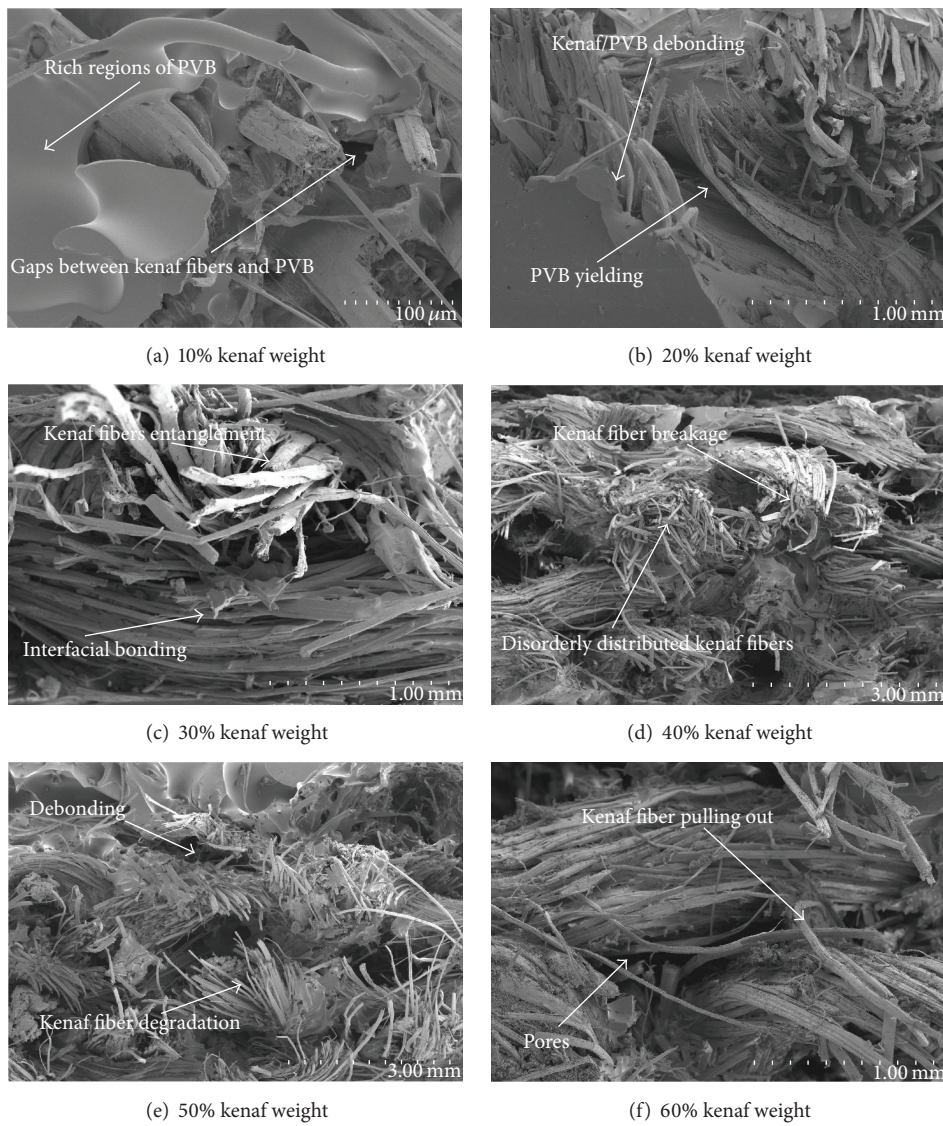


FIGURE 12: The SEM micrographs of the Charpy impact failure surfaces of kenaf/PVB film composite.

energy levels, while the average impact toughness of the other composites showed almost the same behavior when tested at low energy levels (0.5 J). As research studies have reported [28, 37], both fiber content and properties of the polymer are accountable for deciding the impact toughness of composites. This implies that both the effect of interlaminar delimitation and interfacial strength between fiber and matrix highly decide impact properties, especially in the case of weaving pattern as stated by others [38].

3.4. Morphological Properties. SEM photographs of all the impacted specimens (10%, 20%, 30%, 40%, 50%, and 60% kenaf fiber content) are shown in Figure 12. The fractured impact surface with 21.6 J energy level was selected as a representative sample for the interpretation of the degree of interfacial adhesion. It is evident that the differences in interfacial adhesion resulted in the different fracture mechanism, a combination of matrix cracking and gaps between kenaf fibers and PVB film as well as kenaf fiber breakage. These failure mechanisms agree very well with the impact damage observed by Khan et al. [39] for Jute fabric-reinforced polypropylene composite and by Dhakal et al. [40] for nonwoven hemp fiber reinforced unsaturated polyester composites.

Rich regions and matrix failure were noted in the SEM image of the 10% and 20% kenaf fiber content, as shown in Figures 12(a) and 12(b), because of the lower kenaf fiber content, attributed to poor kenaf fiber distribution, hence resulting in poor energy dissipation. In 30% and 40% kenaf fiber content, an increasing trend in impact strength was found. As a result of a strong bond at the interface, the impact damage does not propagate into the vicinity of the impacted point. This was revealed by SEM micrograph in Figures 12(c) and 12(d) which showed that the interfacial bonding between kenaf fiber and PVB film was the best among all samples, reaching the highest impact strength. However, when the kenaf fiber weight reaches beyond its threshold value, the impregnation of PVB film into the interface area is decreased and results in weak bonding between PVB film and kenaf fiber. As a result of poor kenaf fiber/PVB film adhesion, the composites could not withstand further impact loads, as noticed in the composites of 50% and 60% kenaf fiber content. Figure 12(e) shows both entanglement of kenaf fiber and kind of debonding between the kenaf fibers and PVB film, still not appearing to be to the maximum extent as shown in Figure 12(f). As a result, more shear action is observed in the interfacial zone which leads to layer-by-layer fracture of the matrix (delamination) and corroborates the observed decrease in impact strength. Also, poor wetting of the kenaf fiber surface and cohesive force between kenaf fibers may decrease with the increase in kenaf fibers content.

4. Conclusions

A new type of composite using kenaf fiber reinforced PVB film was fabricated with different fiber content, and its mechanical behavior was studied. Six types of laminated composites were fabricated and compared under tensile and

flexural and four levels of impact conditions. It was concluded that the mechanical characteristics of the kenaf/PVB composites were variously affected by the kenaf fiber loading. 40% kenaf content composite has optimized mechanical properties, followed by 30% kenaf content, while 10% and 60% kenaf content composites have shown the weakest performance. SEM examinations of impact specimens show that the kenaf fiber content played an important role in the interfacial bonding between kenaf fiber and PVB film, which affects the mechanical properties of composites.

Conflict of Interests

The authors declare that there is no conflict of interests regarding the publication of this paper.

Acknowledgments

This work is supported by UPM under GP-IPS/2014/9438714 and GP-IPB Grant, 9415402. The authors would like to express their gratitude and sincere appreciation to the Mechanical and Manufacturing Engineering Department and Aerospace Manufacturing Research Centre of the Universiti Putra Malaysia. Their appreciation and gratitude also extend to the Ministry of Higher Education & Scientific Research of Iraq and to the Material Engineering Department, College of Engineering, at the Al-Mustansiriya University for their scientific assistance and financial support.

References

- [1] D. Saravana Bavan and G. C. Mohan Kumar, "Potential use of natural fiber composite materials in India," *Journal of Reinforced Plastics and Composites*, vol. 29, no. 24, pp. 3600–3613, 2010.
- [2] S. D. Salman, Z. Leman, M. T. Sultan, M. R. Ishak, and F. Cardona, "Kenaf/synthetic and Kevlar[®]/cellulosic fiber-reinforced hybrid composites: a review," *BioResources*, vol. 10, no. 4, 2015.
- [3] S. D. Salman, Z. Leman, M. T. H. Sultan, M. R. Ishak, and F. Cardona, "Influence of resin system on the energy absorption capability and morphological properties of plain woven kenaf composites," *IOP Conference Series: Materials Science and Engineering*, vol. 100, no. 1, Article ID 012053, 2015.
- [4] Y. A. El-Shekeil, S. M. Sapuan, and M. Haron, "Optimization of processing parameters and fiber content of cocoa pod husk fiber-reinforced thermoplastic polyurethane composites by Taguchi Method," in *Applied Mechanics and Materials*, vol. 564, pp. 394–399, 2014.
- [5] Y. A. El-Shekeil, S. M. Sapuan, E. S. Zainudin, and A. Khalina, "Effect of fiber loading on the mechanical properties of kenaf fiber reinforced thermoplastic polyurethane composite," *Key Engineering Materials*, vol. 471, pp. 1058–1063, 2011.
- [6] Y. El-Shekeil, S. Sapuan, M. Jawaid, and O. Al-Shuja'a, "Influence of fiber content on mechanical, morphological and thermal properties of kenaf fibers reinforced poly(vinyl chloride)/thermoplastic polyurethane poly-blend composites," *Materials & Design*, vol. 58, pp. 130–135, 2014.
- [7] S. Joseph, M. S. Sreekala, Z. Oommen, P. Koshy, and S. Thomas, "A comparison of the mechanical properties of phenol formaldehyde composites reinforced with banana fibres and

- glass fibres," *Composites Science and Technology*, vol. 62, no. 14, pp. 1857–1868, 2002.
- [8] H. Ku, H. Wang, N. Pattarachaiyakoo, and M. Trada, "A review on the tensile properties of natural fiber reinforced polymer composites," *Composites Part B: Engineering*, vol. 42, no. 4, pp. 856–873, 2011.
- [9] S. Ochi, "Mechanical properties of kenaf fibers and kenaf/PLA composites," *Mechanics of Materials*, vol. 40, no. 4-5, pp. 446–452, 2008.
- [10] T. Nishino, K. Hirao, M. Kotera, K. Nakamae, and H. Inagaki, "Kenaf reinforced biodegradable composite," *Composites Science and Technology*, vol. 63, no. 9, pp. 1281–1286, 2003.
- [11] B.-H. Lee, H.-J. Kim, and W.-R. Yu, "Fabrication of long and discontinuous natural fiber reinforced polypropylene biocomposites and their mechanical properties," *Fibers and Polymers*, vol. 10, no. 1, pp. 83–90, 2009.
- [12] H. Hargitai, I. Rácz, and R. D. Anandjiwala, "Development of HEMP fiber reinforced polypropylene composites," *Journal of Thermoplastic Composite Materials*, vol. 21, no. 2, pp. 165–174, 2008.
- [13] S. Shibata, Y. Cao, and I. Fukumoto, "Flexural modulus of the unidirectional and random composites made from biodegradable resin and bamboo and kenaf fibres," *Composites Part A: Applied Science and Manufacturing*, vol. 39, no. 4, pp. 640–646, 2008.
- [14] S. C. Liew, *Characterization of natural fiber polymer composites for structural application [Ph.D. thesis]*, Faculty of Civil Engineering, Universiti Teknologi Malaysia, 2008.
- [15] H. R. Rao, M. A. Kumar, and G. R. Reddy, "Hybrid composites: effect of fibers on mechanical properties," *International Journal of Macromolecular Science*, vol. 1, no. 1, pp. 9–14, 2011.
- [16] M. J. Sharba, S. D. Salman, Z. Leman, M. T. H. Sultan, M. R. Ishak, and M. A. A. Hanim, "Effects of processing method, moisture content, and resin system on physical and mechanical properties of woven kenaf plant fiber composites," *BioResources*, vol. 11, no. 1, pp. 1466–1476, 2015.
- [17] M. J. Sharba, Z. Leman, M. T. Sultan, M. R. Ishak, and M. A. A. Hanim, "Effects of kenaf fiber orientation on mechanical properties and fatigue life of glass/kenaf hybrid composites," *BioResources*, vol. 11, no. 1, pp. 1448–1465, 2015.
- [18] S. D. Salman, M. J. Sharba, Z. Leman, M. T. Sultan, M. R. Ishak, and F. Cardona, "Physical, mechanical, and morphological properties of woven kenaf/polymer composites produced using a vacuum infusion technique," *International Journal of Polymer Science*, vol. 2015, Article ID 894565, 10 pages, 2015.
- [19] ASTM, "Standard test method for tensile properties of polymer matrix composite materials," ASTM D3039/D3039M-10, ASTM International, West Conshohocken, Pa, USA, 2010.
- [20] ASTM, "Standard test methods for flexural properties of unreinforced and reinforced plastics and electrical insulating materials," ASTM D790-10, ASTM International, West Conshohocken, Pa, USA, 2010.
- [21] ASTM, "Standard test method for determining the Charpy impact resistance of notched specimens of plastics," ASTM D6110-10, ASTM International, West Conshohocken, Pa, USA, 2010.
- [22] S. D. Salman, Z. Leman, M. T. H. Sultan, M. R. Ishak, and F. Cardona, "The effects of orientation on the mechanical and morphological properties of woven kenaf-reinforced poly vinyl butyral film," *BioResources*, vol. 11, no. 1, pp. 1176–1188, 2016.
- [23] W. Kim, A. Argento, E. Lee et al., "High strain-rate behavior of natural fiber-reinforced polymer composites," *Journal of Composite Materials*, vol. 46, no. 9, pp. 1051–1065, 2012.
- [24] F. M. Al-Oqla and S. M. Sapuan, "Natural fiber reinforced polymer composites in industrial applications: feasibility of date palm fibers for sustainable automotive industry," *Journal of Cleaner Production*, vol. 66, pp. 347–354, 2014.
- [25] B. Madsen, P. Hoffmeyer, and H. Lilholt, "Hemp yarn reinforced composites—II. Tensile properties," *Composites Part A: Applied Science and Manufacturing*, vol. 38, no. 10, pp. 2204–2215, 2007.
- [26] M. E. Ali, C. K. Yong, Y. C. Ching, C. H. Chuah, and N.-S. Liou, "Effect of single and double stage chemically treated kenaf fibers on mechanical properties of polyvinyl alcohol film," *BioResources*, vol. 10, no. 1, 2014.
- [27] B. Madsen, A. Thygesen, and H. Lilholt, "Plant fibre composites—porosity and stiffness," *Composites Science and Technology*, vol. 69, no. 7-8, pp. 1057–1069, 2009.
- [28] T. Huber, S. Bickerton, J. Müssig, S. Pang, and M. P. Staiger, "Flexural and impact properties of all-cellulose composite laminates," *Composites Science and Technology*, vol. 88, pp. 92–98, 2013.
- [29] S. Shibata, Y. Cao, and I. Fukumoto, "Press forming of short natural fiber-reinforced biodegradable resin: effects of fiber volume and length on flexural properties," *Polymer Testing*, vol. 24, no. 8, pp. 1005–1011, 2005.
- [30] A. C. de Albuquerque, K. Joseph, L. Hecker de Carvalho, and J. R. M. d'Almeida, "Effect of wettability and ageing conditions on the physical and mechanical properties of uniaxially oriented jute-roving-reinforced polyester composites," *Composites Science and Technology*, vol. 60, no. 6, pp. 833–844, 2000.
- [31] Z. Jiang, F. Chen, G. Wang et al., "Bamboo Bundle Corrugated Laminated Composites (BCLC). Part II. damage analysis under low velocity impact loading," *BioResources*, vol. 8, no. 1, pp. 923–932, 2013.
- [32] V. Tita, J. de Carvalho, and D. Vandepitte, "Failure analysis of low velocity impact on thin composite laminates: experimental and numerical approaches," *Composite Structures*, vol. 83, no. 4, pp. 413–428, 2008.
- [33] R. Joffe and J. Andersons, "13—Mechanical performance of thermoplastic matrix natural-fibre composites," in *Properties and Performance of Natural-Fibre Composites*, K. L. Pickering, Ed., pp. 402–459, Woodhead Publishing, 2008.
- [34] D. C. O. Nascimento, S. N. Monteiro, and L. C. Motta, "Characterization of the toughness of piassava fiber reinforced epoxy matrix composites by Izod impact test," in *Proceeding of the Characterization of Minerals, Metals & Materials-TMS Conference*, pp. 1–7, San Francisco, Calif, USA, February 2009.
- [35] Y. A. El-Shekeil, S. M. Sapuan, and M. W. Algrafi, "Effect of fiber loading on mechanical and morphological properties of cocoa pod husk fibers reinforced thermoplastic polyurethane composites," *Materials & Design*, vol. 64, pp. 330–333, 2014.
- [36] R. Wirawan, S. M. Sapuan, K. Abdan, and R. Yunus, "Tensile and impact properties of sugarcane bagasse/poly (vinyl chloride) composites," *Key Engineering Materials*, vol. 471-472, pp. 167–172, 2011.
- [37] S. Karimi, P. M. Tahir, A. Karimi, A. Dufresne, and A. Abdulkhani, "Kenaf bast cellulosic fibers hierarchy: a comprehensive approach from micro to nano," *Carbohydrate Polymers*, vol. 101, no. 1, pp. 878–885, 2014.
- [38] N. M. Aly, M. A. Saad, E. H. Sherazy, O. M. Kobesy, and A. A. Almetwally, "Impact properties of woven reinforced sandwich

composite panels for automotive applications,” *Journal of Industrial Textiles*, vol. 42, no. 3, pp. 204–218, 2013.

- [39] J. A. Khan, M. A. Khan, R. Islam, and A. Gafur, “Mechanical, thermal and interfacial properties of jute fabric-reinforced polypropylene composites: effect of potassium dichromate,” *Materials Sciences and Applications*, vol. 1, no. 6, pp. 350–357, 2010.
- [40] H. N. Dhakal, Z. Y. Zhang, N. Bennett, and P. N. B. Reis, “Low-velocity impact response of non-woven hemp fibre reinforced unsaturated polyester composites: influence of impactor geometry and impact velocity,” *Composite Structures*, vol. 94, no. 9, pp. 2756–2763, 2012.

Research Article

A Facile Approach to Evaluate Thermal Insulation Performance of Paper Cups

Yudi Kuang, Gang Chen, and Zhiqiang Fang

State Key Laboratory of Pulp and Paper Engineering, South China University of Technology, Guangzhou 510640, China

Correspondence should be addressed to Zhiqiang Fang; fangzq1230@126.com

Received 29 September 2015; Accepted 20 October 2015

Academic Editor: Matheus Poletto

Copyright © 2015 Yudi Kuang et al. This is an open access article distributed under the Creative Commons Attribution License, which permits unrestricted use, distribution, and reproduction in any medium, provided the original work is properly cited.

Paper cups are ubiquitous in daily life for serving water, soup, coffee, tea, and milk due to their convenience, biodegradability, recyclability, and sustainability. The thermal insulation performance of paper cups is of significance because they are used to supply hot food or drinks. Using an effective thermal conductivity to accurately evaluate the thermal insulation performance of paper cups is complex due to the inclusion of complicated components and a multilayer structure. Moreover, an effective thermal conductivity is unsuitable for evaluating thermal insulation performance of paper cups in the case of fluctuating temperature. In this work, we propose a facile approach to precisely analyze the thermal insulation performance of paper cups in a particular range of temperature by using an evaluation model based on the MISO (Multiple-Input Single-Output) technical theory, which includes a characterization parameter (temperature factor) and a measurement apparatus. A series of experiments was conducted according to this evaluation model, and the results show that this evaluation model enables accurate characterization of the thermal insulation performance of paper cups and provides an efficient theoretical basis for selecting paper materials for paper cups.

1. Introduction

The first modern paper cup was initially developed by Lawrence Luellen in 1907. After a hundred years of development, paper cups have become one of the life's necessities for serving hot and cold drinks; they are widely used in fast-food restaurants, coffee shops, and offices, among others, because they are inexpensive, biodegradable, and renewable and because there are environmentally friendly properties of paper [1, 2]. The consumption of paper cups in China has increased sharply in recent years. More than 25 billion paper cups were consumed in 2011, and the number will continue to increase, with an estimated future annual growth rate of 12.84%. Paper cups are sometimes used to serve hot drinks or food, and the thermal insulation performance of paper should be considered because of the possibility of serious scalding accident. However, there is a lack of uniform standards, such as national standard or industrial standard for the convenient and accurate evaluation of the thermal insulation performance of paper cups.

Heat is transferred via conduction, convection, and radiation [3], and the impact of each mode of heat transfer depends

on the application. The thermal insulation performance of paper cups is determined by the paper materials. Paper is considered to be a type of porous fibrous material with a porosity of 40%~70%. When the volume fraction of cellulose fibers is greater than 1%, heat transfer by convection is negligible because the air cells in the fiber system are too small to support convection or turbulence [4–6]. Heat transfer by radiation is a linear function of temperature cubed (T^3) according to the Rosseland approximation [7]. Hence, the radiative heat transfer is also inappreciable at the relatively low operating temperature of paper cups [8, 9]. Therefore, an effective thermal conductivity is generally used to characterize the conductive heat transfer and thermal insulation performance of paper materials.

Schuhmeister first proposed a model for the thermal conductivity of fibrous materials [10]. Many researchers have since worked on modifications of this model [11–13]. The most basic expression for defining an effective thermal conductivity in porous media was given by Bhattacharyya [14] and Bankvall [12]

$$k_{\text{eff}} = \alpha k_f + (1 - \alpha) k_g. \quad (1)$$

The above equation assumes that the conductive heat travels through both the fibers and the interstitial fluid (often air). Therefore the effective thermal conductivity was based on a weighted average of the thermal conductivity values of the fibers and the interstitial fluid. The first term in the right-hand side of (1) overpredicts the conductivity of the solid phase. The second term is expected to predict the conductivity of the fluid phase. However, there are some questions regarding this equation. The heat transfer does not occur in a parallel mode through the paper because of the random fiber system, and the thermal barrier resistance should be considered when heat flows through a number of fiber-to-fiber contact areas [15]. The impact of each parameter on the thermal insulation performance of paper was studied by computer simulation. Through this simulation, we can predict the effective thermal conductivity of the whole media [15, 16].

However, a variety of parameters such as temperature and pressure [17], moisture [18, 19], the nature of the raw materials, and the macrostructure and microstructure of the paper [20] will affect the veracity of the effective thermal conductivity [21]. Another problem with an effective thermal conductivity is that the numerical value changes with temperature. Paper cups are always used at a relatively low temperature (below 100°C) that fluctuates. Therefore, an effective thermal conductivity is unsuitable for practical applications. In this study, we proposed a facile approach to precisely analyze the thermal insulation performance of paper cups by establishing an evaluation model. For the first time, we propose a new parameter named “temperature factor,” which is a simple and convenient parameter for characterizing the thermal insulation performance of a paper cup. Moreover, an apparatus for the experiment is also designed, as shown in Section 2.

2. Model Establishment

On the basis of MISO (Multiple-Input Single-Output) technical theory [22], the equation for the effective thermal conductivity can be expressed as shown below

$$k_{\text{eff}} = f(k_f, k_g, \beta, \gamma, \dots). \quad (2)$$

This equation denotes the effective thermal conductivity as a function of the factors that influence the thermal insulation performance of paper cups. When this approach is used, only the value of k_{eff} is required to appraise the thermal insulation performance of paper cups. However, Fourier’s law states that thermal conductivity is independent of the temperature gradient but necessarily of temperature itself. The thermal conductivity is a function of temperature. That means the effective thermal conductivity was suited for evaluating the thermal conductivity of materials at a single temperature [23]. For paper cups, evaluation of the thermal insulation performance in a particular temperature range is more suitable for practical applications. Therefore, for assessing the thermal insulation performance of paper cups, this study includes the proposal of the temperature factor and the design of a corresponding apparatus for measurement

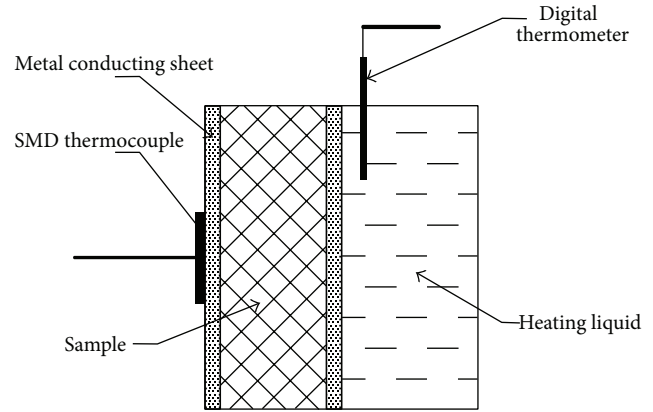


FIGURE 1: Schematic of setup for thermal insulation measurement.

of this new parameter. The temperature factor represents the thermal insulation performance of paper cups within a certain temperature interval, and the apparatus can help to quickly determine the value of the parameter.

2.1. Experimental Apparatus. To evaluate the thermal insulation performance of paper cups, an apparatus to test the temperature difference between the inside and outside of the cup wall was set up, and its structure is shown schematically in Figure 1. This apparatus was assembled based on the method used by Iioka [24], which was comprised of a heating section, a support frame, and a measuring part.

The sample is held between two heat-conducting fins to reduce the small amount of radiative heat as much as possible and to maintain stable heat transfer between the interface of the paper and the other phases. The internal surface temperature is the same as the heating liquid and is tuned by changing the heating power. A digital thermometer is utilized to monitor the in situ temperature of the liquid. A patch type thermocouple is posted on the heat-conducting metal sheet at the outside of the sample to monitor the cold side temperature. The temperature of the heating liquid is initially the ambient temperature and rises at a rate of 2°C/min. The temperatures on both sides of the sample are synchronously recorded every 5°C.

Pretreatment of paper materials is necessary to maintain a steady state heat transfer in paper media. First a 50 × 50 mm sample is cut from the cup and placed in a constant temperature humidity chamber at a temperature of 20°C and a relative humidity of 10% for 8 hours. A thin polyethylene film is then laminated onto each side of the paper to prevent moisture from penetrating the paper media. This allows the convective heat transfer on both surfaces of the paper to be neglected in the next measurement. What is more, the thermal insulation effect of the PE layer is neglected as the thickness of the laminated film is much thinner than the fibrous layer.

2.2. Establishment of the Numerical Model. Figure 2 illustrates the relationship between the hot surface temperature and the cold surface temperature of paper materials.

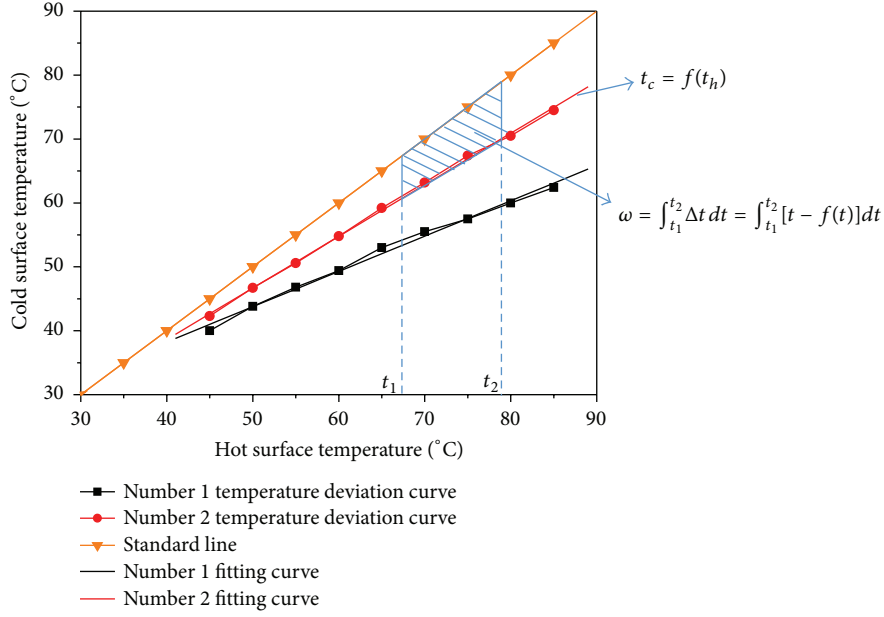


FIGURE 2: Cold surface temperature as a function of hot surface temperature for the paper cups. The area of the shaded part (the shape with the oblique lines) is ω .

The temperatures on both sides of the material will be the same when the material has no insulating effect, as in the diagonal line in Figure 2 referred to as “standard line.” The cold surface temperature-hot surface temperature curves will migrate downward from the standard line because the temperature of the cold side must be lower than that of the hot side for thermal insulation materials. These curves are labeled deviation curves and are the dot and dash curves in Figure 2 (the circle and the square symbols represent different types of paper materials). Moreover, the further the deviation from the standard line, the better the thermal insulation performance. Hence, the deviation curves are used to qualitatively analyze the thermal insulation performance of paper materials.

Furthermore, each fitting curve is obtained by curve fitting based on the original experimental data and is given by

$$t_c = f(t_h). \quad (3)$$

The area between the standard line and a fitting curve in a particular temperature interval $[t_1, t_2]$ is then used to quantitatively analyze the thermal insulation performance of the paper material in a particular temperature range, such as the shaded part (depicted with oblique lines) in Figure 2. We define the temperature factor (ω) as the area of the shaded part given by the expression

$$\omega = \int_{t_1}^{t_2} \Delta t dt = \int_{t_1}^{t_2} [t - f(t)] dt. \quad (4)$$

The higher the numerical value of ω for a paper material in the closed interval $[t_1, t_2]$, the better the thermal insulation performance of the paper cup in a particular temperature range.

TABLE 1: Data of the paper cup samples.

Number	Grammage g/m ²	Thickness mm	Structure type
1	252	0.335	I
2	280	0.333	I
3	248	0.321	I
4	537	0.672	II
5	504	0.646	II
6	479	0.820	III with air layer
7	606	0.780	III with air layer
8	282	0.512	III with foam surface
9	606	0.950	III with air layer
10	356	0.706	III with foam surface
11	299	0.361	I
12	543	0.695	II

3. Experimental

3.1. Materials. Paper cups with different structures were collected from the market and divided into three types based on the study of Iioka et al. [25–27], as shown in Figure 3. The main body of the paper cup was a single fibrous layer for structure I and a double-layer structure for structure II. Structure III was a composite structure composed of material of different natures. The structure type and basic properties of each paper sample are given in Table 1.

3.2. Heat Insulation Performance Test. All of the samples in Table 1 are pretreated and tested based on the methods mentioned in Section 2.1. The experiment was performed

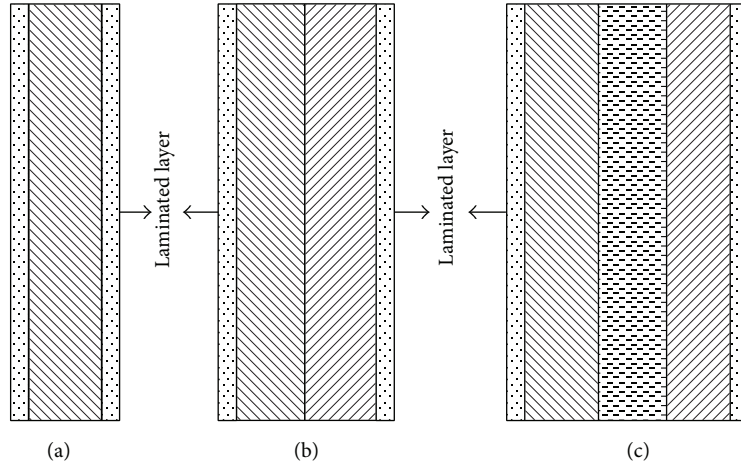


FIGURE 3: Structure type classification: (a) structure I, (b) structure II, and (c) structure III.

at 23°C and 50% RH ambient conditions. The operating environment for evaluation of the paper cups was set to be the closed interval from 70 to 85°C. The temperatures of the cold and hot surfaces were recorded synchronously for every 5°C temperature change as the liquid temperature was varied from 45 to 85°C.

4. Results and Discussion

4.1. Qualitative Analysis for Thermal Insulation Performance of Paper Cups. Figure 4(a) shows the relationship between the hot surface temperature and the cold surface temperature of each sample in Table 1. With increasing temperature of the hot surface, increases in both the cold surface temperature and the amount of deviation from the standard line were observed. Furthermore, most of these curves are approaching each other and are hard to identify. Moreover, some curves crossed or overlapped in the closed interval, as shown in the high magnification image of Figure 4(a), for instance, number 4, number 5, number 8, number 10, and number 12.

Curve fits for each deviation curve in Figure 4(a) were obtained with Origin 8 software (Figure 4(b)). The broken lines with symbols were replaced by a group of continuous lines of different colors. The phenomenon of crossing and overlapping of the curves dramatically decreased with the use of the fitting curves, although these problems still exist. The samples were ranked by approximate thermal insulation performance as below (> means better than, ≈ means similar):

$$\text{No. } 7 > 6 > 9 > 12 \approx 10 \approx 4 \approx 5 \approx 8 > 3 > 11 > 1 > 2. \quad (5)$$

The thermal insulation performance is proportional to thickness [28], and the thermal insulation performance of the air is better than that of a solid, so structure III with an air layer can effectively increase the thermal insulation performance of paper cups. In addition, the thermal insulation performances of number 7, number 6, and number

TABLE 2: Fitted curve equations, linear correlation coefficients, temperature factors, and temperature factors per unit thickness.

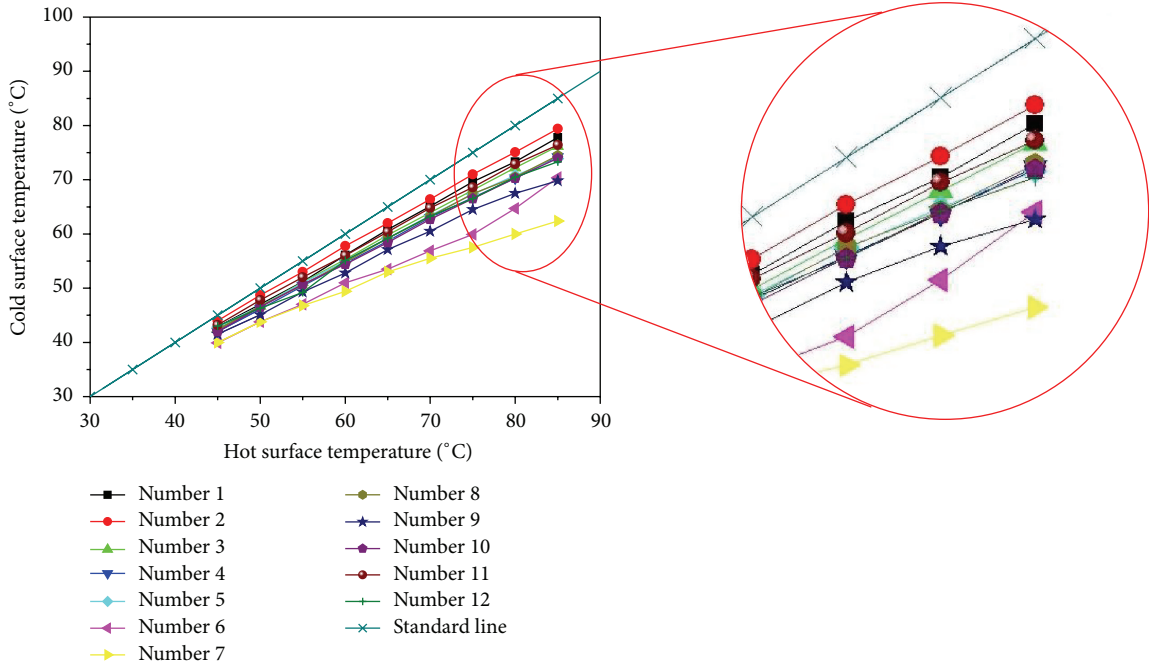
Number	Equation	R	ω °C ²	ω/b °C ² /mm
1	$y = 3.15722 + 0.881x$	0.99926	90.98	271.58
2	$y = 4.43 + 0.88467x$	0.99974	67.62	203.06
3	$y = 4.52167 + 0.84633x$	0.99979	110.82	345.23
4	$y = 5.92444 + 0.808x$	0.99911	134.33	199.90
5	$y = 7.39833 + 0.79233x$	0.99819	130.44	201.92
6	$y = 7.23556 + 0.72133x$	0.98962	215.42	262.71
7	$y = 16.14278 + 0.55233x$	0.99237	278.27	356.76
8	$y = 6.32333 + 0.80733x$	0.99874	129.13	252.21
9	$y = 9.11389 + 0.72833x$	0.99568	179.11	188.54
10	$y = 6.54056 + 0.79767x$	0.99938	137.10	194.19
11	$y = 6.045 + 0.83367x$	0.99932	102.68	284.43
12	$y = 7.22556 + 0.78867x$	0.99425	137.29	197.54

9, which all have structure III with an air layer between the fibrous layers, were better than the others. However, it was difficult to discriminate the differences in the thermal insulation performances of number 4, number 5, number 8, number 10, and number 12.

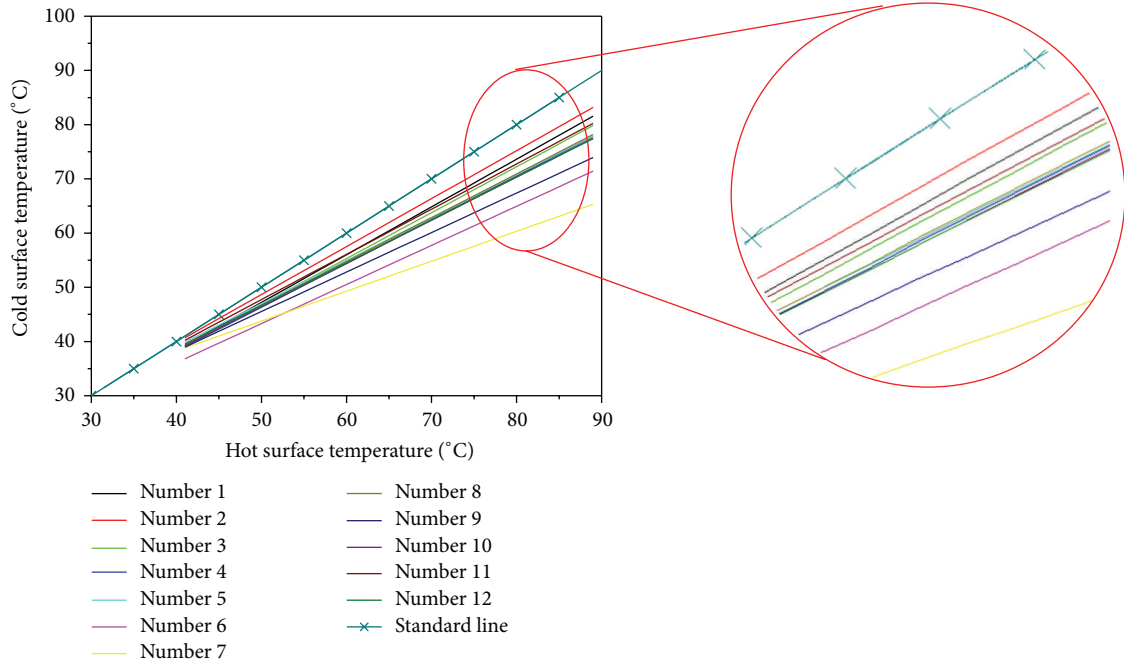
4.2. Quantitative Analysis for Thermal Insulation Performance of Paper Cups by Temperature Factor ω . The temperature factor ω was used to quantify the thermal insulation performance of paper cups. First, the fitting curves and equations were established using linear fitting. The equations and the linear correlation coefficients are shown in Table 2. The process for calculation of the temperature factor ω was as follows.

Assume that the linear regression equation for the fit to the deviation curve is

$$y = A + Cx. \quad (6)$$



(a)



(b)

FIGURE 4: (a) Cold surface temperature as a function of hot surface temperature for the paper cups. (b) The fitting curve of each deviation curve in (a).

The equation of the standard line is

$$y = x. \tag{7}$$

Subtracting (7) from (6) gives

$$y = -A + (1 - C)x. \tag{8}$$

Let $1 - C = B$. Equation (8) can then be expressed as

$$y = -A + Bx. \tag{9}$$

The temperature factor ω is calculated by

$$\omega = \int_{70}^{85} (-A + Bx) dx = 1162.5B - 15A \tag{10}$$

$$= 1162.5(1 - C) - 15A.$$

As shown in Table 2, each sample's temperature factor in the particular range $[70, 85]^{\circ}\text{C}$ was calculated from the fitted curve equations and (10).

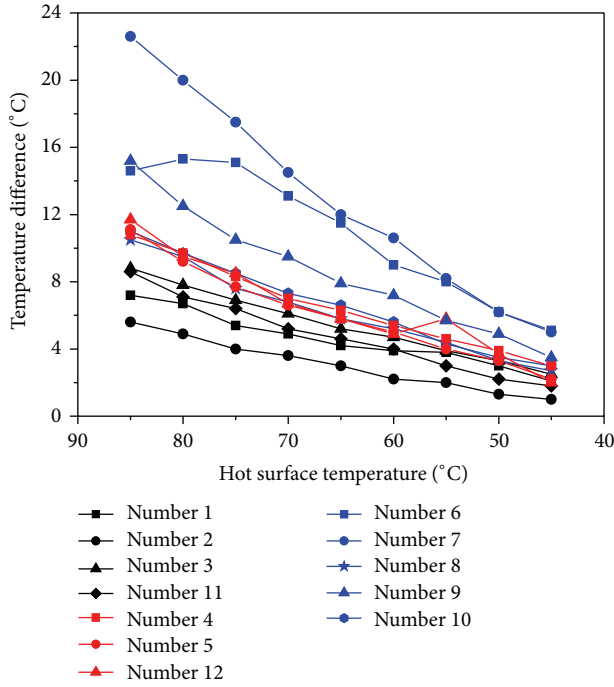


FIGURE 5: Temperature difference as a function of hot surface temperature for the paper cups.

The utilization of the temperature factor clarifies evaluation of each sample's thermal insulation performance in a particular temperature range. We can exactly and accurately rank these paper cups according to their values of ω in Table 2 as

$$\text{No. } 7 > 6 > 9 > 12 > 10 > 4 > 5 > 8 > 3 > 11 > 1 > 2. \quad (11)$$

Rank (11) is almost the same as rank (5). For paper sample numbers 12, 10, 4, 5, and 8, whose thermal insulation performances were approximately equal in rank (5), the specific heat insulation performance order can now be obtained by comparing their values of ω , which are 137.29, 137.10, 134.33, 130.44, and 129.13, respectively. Moreover, the utilization of ω could avoid difficulties associated with the possible overlapping of fitting curves as in Figure 4(b).

4.3. The Application of ω to Paper Cup Design and Selection of Paper Materials. To compare the thermal insulation performance of paper cups with different structures, we calculated the temperature difference at each measurement temperature and plotted the temperature difference curves (Figure 5). The color of each temperature difference curve corresponds to the structure of the sample: black for structure I, red for structure II, and blue for structure III, as shown in Figure 5.

Figure 5 clearly shows the change of temperature difference with the hot surface temperature. Generally, the difference at high temperature is larger than at low temperature. Furthermore, the thermal insulation performance of a sample with a higher curve is better than that of a sample with

a lower one. The order of descending thermal insulation performance of the structures is structure III, structure II, and structure I, and the corresponding ranges of temperature factors are 129.13 to 278.27, 130.44 to 137.29, and 67.62 to 110.82, respectively. The degree of tightness of the curves for samples of the same structure in Figure 5 is consistent with the width of the temperature factor interval for that structure. Hence, we can choose the best structure for paper cups according to the required thermal insulation performance (the range of ω).

In addition to the structure, another factor in the design of paper cups is the selection of paper materials. The temperature difference between the cold and hot surfaces of paper is proportional to the thickness according to Fourier's law and the equation for heat conduction through a flat single-layered wall [28]:

$$Q = -kA \frac{dt}{dx}, \quad (12)$$

$$\Delta t = t_2 - t_1 = \frac{bQ}{kA}. \quad (13)$$

Simultaneous equations (4) and (13) give

$$\omega = \int_{t_1}^{t_2} \Delta t dt = b \int_{t_1}^{t_2} \left[\frac{Q}{kA} \right] dt. \quad (14)$$

Equation (14) demonstrates that the value of the temperature factor ω is also proportional to the thickness of the paper material. Thus, the temperature factor ω per unit length in the thickness direction could be expressed as

$$\frac{\omega}{b} = \frac{1}{b} \int_{t_1}^{t_2} [t - f(t)] dt. \quad (15)$$

Equation (15) also manifests the thermal insulation performance of paper cups per unit length in the thickness direction. From the simultaneous equations (10) and (15), the thermal insulation performance of each sample per unit length in the thickness direction was obtained and given in Table 2. According to the numerical values of ω/b in Table 2, the paper materials in order of descending thermal insulation performance per unit length in the thickness direction are

$$\text{No. } 7 > 3 > 11 > 1 > 6 > 8 > 2 > 5 > 4 > 12 > 10 > 9. \quad (16)$$

Obviously, rank (16) is quite different from rank (11). A sample with better thermal insulation performance of the whole media may not be outstanding when compared on a per thickness basis. Therefore, many benefits will flow from this finding. For instance, it can be speculated that if the fiber layer of sample 4 was instead by the fiber as sample 3, it would have better thermal insulation performance than present sample 4.

In conclusion, the structure of paper cups significantly influenced the thermal insulation performance. The difference in thermal insulation performance can be attributed to a multitude of factors, such as fiber type, paper bulk, porosity,

moisture, and production process. Numerous parameters cause accurate measurement of the effective thermal conductivity to be difficult and time consuming. However, it will be more convenient to use the temperature factor ω when characterizing the thermal insulation performance of paper cups in practical applications and, of course, during the design of thermally insulating paper cups.

5. Conclusion

- (1) This work proposed a facile approach to analyze the thermal insulation performance of paper cups by establishing a novel evaluation model that includes a characterization parameter named “temperature factor” ω and a measurement apparatus.
- (2) The temperature factor is defined as $\omega = \int_{t_1}^{t_2} [t - f(t)]dt$, which is the integrated area between the standard line and the fitting curve in a particular temperature range $[t_1, t_2]$. Moreover, the value of the temperature factor is proportional to the thickness of the paper samples.
- (3) The thermal insulation performance of paper cups with different structures is quantitatively analyzed based on the value of the temperature factor in the temperature range of 70 to 85°C. The calculation results of the temperature factor of 12 paper cup samples show that the structure type of the cups is the most important parameter which strongly influences the thermal insulation performance of the paper cups.

Conflict of Interests

The authors declare that there is no conflict of interests regarding the publication of this paper.

Acknowledgments

Moreover, Zhiqiang Fang would like to acknowledge the financial support from Self-Determined and Innovative Research Funds of State Key Laboratory of Pulp and Paper-making Engineering (2015QN01) and China Postdoctoral Science Foundation (2015M570716).

References

- [1] H. P. S. Abdul Khalil, A. H. Bhat, and A. F. Ireana Yusra, “Green composites from sustainable cellulose nanofibrils: a review,” *Carbohydrate Polymers*, vol. 87, no. 2, pp. 963–979, 2012.
- [2] E. van der Harst and J. Potting, “A critical comparison of ten disposable cup LCAs,” *Environmental Impact Assessment Review*, vol. 43, pp. 86–96, 2013.
- [3] N. Kaarlo, *Paper Physics*, Paperi ja Puu Oy, 2008.
- [4] S. S. Woo, I. Shalev, and R. L. Barker, “Heat and moisture transfer through nonwoven fabrics part I: heat transfer,” *Textile Research Journal*, vol. 64, no. 3, pp. 149–162, 1994.
- [5] B. Farnworth, “Comments on ‘Heat transfer characteristics of nonwoven insulating materials,’” *Textile Research Journal*, vol. 57, pp. 615–616, 1987.
- [6] C. M. Pelanne, “Heat flow principles in thermal insulations,” *Journal of Building Physics*, vol. 1, no. 1, pp. 48–80, 1977.
- [7] M. Spinnler, E. R. F. Winter, R. Viskanta, and T. Sattelmayer, “Theoretical studies of high-temperature multilayer thermal insulations using radiation scaling,” *Journal of Quantitative Spectroscopy and Radiative Transfer*, vol. 84, no. 4, pp. 477–491, 2004.
- [8] K. Daryabeigi, “Heat transfer in high-temperature fibrous insulation,” *Journal of Thermophysics and Heat Transfer*, vol. 17, no. 1, pp. 10–20, 2003.
- [9] D. Kamran, “Analysis and testing of high temperature fibrous insulation for reusable launch vehicles,” in *Proceedings of the 37th Aerospace Sciences Meeting and Exhibit*, AIAA99-1044, Reno, Nev, USA, January 1999.
- [10] J. Schuhmeister, *Versuche über das wärmeleitungsvermögen der baumwolle, schafwolle und seide*, 1878.
- [11] W. J. Mantle and W. S. Chang, “Effective thermal conductivity of sintered metal fibers,” *Journal of Thermophysics and Heat Transfer*, vol. 5, no. 4, pp. 545–549, 1991.
- [12] C. Bankvall, “Heat-transfer in fibrous materials,” *Journal of Testing and Evaluation*, vol. 1, no. 3, pp. 235–243, 1973.
- [13] S. Baxter, “The thermal conductivity of textiles,” *Proceedings of the Physical Society*, vol. 58, no. 1, pp. 105–118, 1946.
- [14] R. K. Bhattacharyya, “Heat transfer model for fibrous insulations,” *Thermal Insulation Performance*, ASTM STP 718, 1980.
- [15] R. Arambakam, H. Vahedi Tafreshi, and B. Pourdeyhimi, “A simple simulation method for designing fibrous insulation materials,” *Materials and Design*, vol. 44, pp. 99–106, 2013.
- [16] M.-S. Jeng, R. Yang, D. Song, and G. Chen, “Modeling the thermal conductivity and phonon transport in nanoparticle composites using Monte Carlo simulation,” *Journal of Heat Transfer*, vol. 130, no. 4, Article ID 042410, 2008.
- [17] B.-M. Zhang, S.-Y. Zhao, and X.-D. He, “Experimental and theoretical studies on high-temperature thermal properties of fibrous insulation,” *Journal of Quantitative Spectroscopy and Radiative Transfer*, vol. 109, no. 7, pp. 1309–1324, 2008.
- [18] U. Leskovšek and S. Medved, “Heat and moisture transfer in fibrous thermal insulation with tight boundaries and a dynamical boundary temperature,” *International Journal of Heat and Mass Transfer*, vol. 54, no. 19–20, pp. 4333–4340, 2011.
- [19] J. Fan and X. Wen, “Modeling heat and moisture transfer through fibrous insulation with phase change and mobile condensates,” *International Journal of Heat and Mass Transfer*, vol. 45, no. 19, pp. 4045–4055, 2002.
- [20] Q. Y. Zhu, M. H. Xie, J. Yang, Y. Q. Chen, and K. Liao, “Influence of chitosan and porosity on heat and mass transfer in chitosan-treated porous fibrous material,” *International Journal of Heat and Mass Transfer*, vol. 55, no. 7–8, pp. 1997–2007, 2012.
- [21] P. Furmanski, “Influence of different parameters on the effective thermal conductivity of short-fiber composites,” *Journal of Thermoplastic Composite Materials*, vol. 4, no. 4, pp. 349–362, 1991.
- [22] A. L. Moustakas and S. H. Simon, “Optimizing multiple-input single-output (MISO) communication systems with general gaussian channels: nontrivial covariance and nonzero mean,” *IEEE Transactions on Information Theory*, vol. 49, no. 10, pp. 2770–2780, 2003.
- [23] W. L. McCabe, J. C. Smith, and P. Harriott, *Unit Operations of Chemical Engineering*, McGraw-Hill, New York, NY, USA, 1993.
- [24] A. Iioka, “Method for producing a heat-insulating paper container from a paper coated or laminated with a thermoplastic synthetic resin film,” Google Patents, 1984.

- [25] R. W. Hollis and D. Stamatiou, "Method of reinforcing a plastic foam cup," Google Patents, 2010.
- [26] R. E. Fredricks, M. A. Breining, W. R. Pucci et al., "Heat insulating paper cups," Google Patents, 2002.
- [27] A. Iioka, K. Ishii, and Y. Oguma, "Heat-insulating paper container and method for producing the same," Google Patents, 1996.
- [28] M. Thirumaleshwar, *Fundamentals of Heat and Mass Transfer*, Pearson Education India, 2009.

Research Article

Dynamics Analysis of the Melt Conveying Process in a Novel Extruder

Zan Huang^{1,2,3}

¹*School of Marine Engineering, Guangzhou Maritime Institute, Guangzhou, Guangdong 510725, China*

²*Department of Chemical Engineering, Hong Kong University of Science and Technology, Clear Water Bay, Kowloon, Hong Kong*

³*Center for Polymer Processing and Systems, HKUST Fok Ying Tung Research Institute, Nansha, Guangzhou, Guangdong 511458, China*

Correspondence should be addressed to Zan Huang; zhuanggz@aliyun.com

Received 23 August 2015; Revised 27 October 2015; Accepted 27 October 2015

Academic Editor: Matheus Poletto

Copyright © 2015 Zan Huang. This is an open access article distributed under the Creative Commons Attribution License, which permits unrestricted use, distribution, and reproduction in any medium, provided the original work is properly cited.

This study investigates dynamics of the melt conveying process in a novel extruder in which a polymer experiences a primarily elongational deformation field. The working principle of the novel extruder is completely different from that of conventional screw extruders. At the last stage of polymer processing in the proposed novel extruder, melt is conveyed through feeding and discharging processes. Here we present a mathematical model to analyze dynamics in the melt conveying process. Melt extrusion is primarily influenced by the position of vane chamber and the structural parameters of the novel extruder such as eccentricity.

1. Introduction

Polymer manufacturing involves melting and plasticizing material from glass to viscous states. During this process, the solid bed disappears completely and the polymer is fully melted. The role of a metering section is to further plasticize and homogenize the viscous polymer melt. At the end of the metering section, the melt is dispensed from the extruder headpiece at constant pressure and temperature.

Polymer melt flow in the metering section must abide by the laws of conservation of mass, momentum, and energy. To solve the corresponding equations of continuity, motion, and energy, the material parameters of the polymer must be defined by an appropriate constitutive equation. Because polymer melt generally behaves as a non-Newtonian fluid, a complex constitutive equation is required to accurately model the melt behavior. Because of this complexity, it is difficult to obtain an analytical solution for the complex flow field and geometric parameters of the extruder [1, 2]. To simplify the system, approximations are made which reduce the problem into less complex terms. A linear constitutive model or the equivalent or average Newtonian viscosity has been used to simplify the constitutive equation of the melt

[3, 4]. Alternatively, the melt flow in the metering section of a screw extruder can be considered as the linear superposition of drag flow and pressure flow by simplifying the flow field [5]. More recently, numerical simulations have been used to understand the melt conveying process [6–12]. In a dynamic polymer extruder, changes in the melt elasticity are more apparent when the flow is disturbed by the action of a vibrational field. Zhang and Qu [13] corrected the Tanner constitutive equation and established a dynamic model of the melt conveying process when exposed to a vibration force field.

In recent years, many scholars have proposed methods to reduce the power consumption of an extruder. For example, Qu et al. [14–16] introduced the pulsating electromagnetic force field in the extrusion process, which reduced overall power consumption. The novel vane extruder introduced in this study provides a reduction in extruder power consumption, which can be verified by experiments [17]. Qu et al. [18] have also studied the power consumption of the extrusion process in a vane extruder.

In this paper, an analytical model of polymer melt extrusion is established, including solving the velocity distribution,

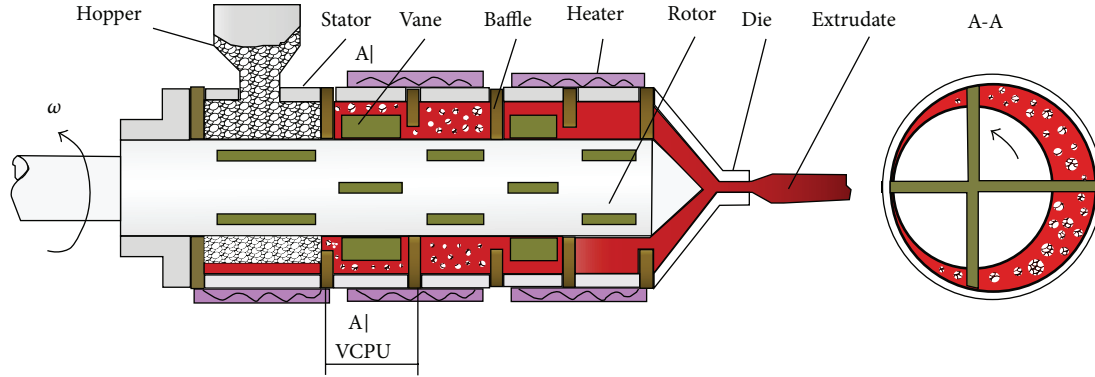


FIGURE 1: The schematic diagram of the novel extruder.

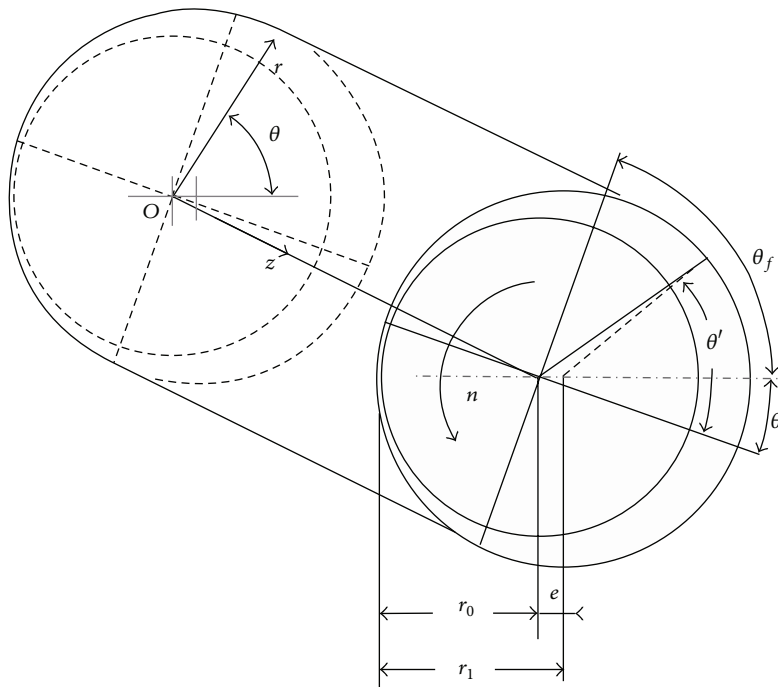


FIGURE 2: The cylindrical coordinate system in VCPU.

pressure gradient, extrusion flow rate, and dynamics of the melt flow field.

2. Description of the Melt Conveying Process in the Extensional Extruder

Figure 1 shows the internal structure of a vane extruder. As introduced by Qu et al. [19], a vane extruder includes several Vane Conveying and Plasticizing Units (VCPUs) throughout the chamber. Figure 2 shows the VCPUs in the cylindrical coordinate system (r, θ, z) , where the origin O is defined as the center of the rotor, r gives the radial position along the rotor shaft, θ is defined along the circumferential direction of the VCPUs where the rotation direction of the rotor is defined as positive, and z is the axial direction of the rotor where the positive direction is defined along the rotor shaft from the feed material baffle to the discharge material baffle. The main

geometric parameters of the VCPU system are (1) the outer radius of the rotor r_0 ; (2) the inner radius of the stator r_1 ; (3) the axial width of each VCPU W ; (4) the radial coordinate value of the point of the inner arc of the stator r_2 ; (5) the eccentricity e between the center of the rotor O and the center of the stator O_1 ; (6) the length of the vane Δr_v ; (7) the angular coordinate of the front vane θ_f ; (8) the angular coordinate of the rear vane θ_r .

According to Figure 2 and the cosine theorem, the inner arc of the stator and the length of the vane are related to the VCPU system geometry by

$$\begin{aligned} r_2(\theta) &= \sqrt{r_1^2 - e^2 \sin^2 \theta} + e \cos \theta, \\ \Delta r_v(\theta) &= e + e \cos \theta - \frac{e^2 \sin^2 \theta}{2r_1}. \end{aligned} \quad (1)$$

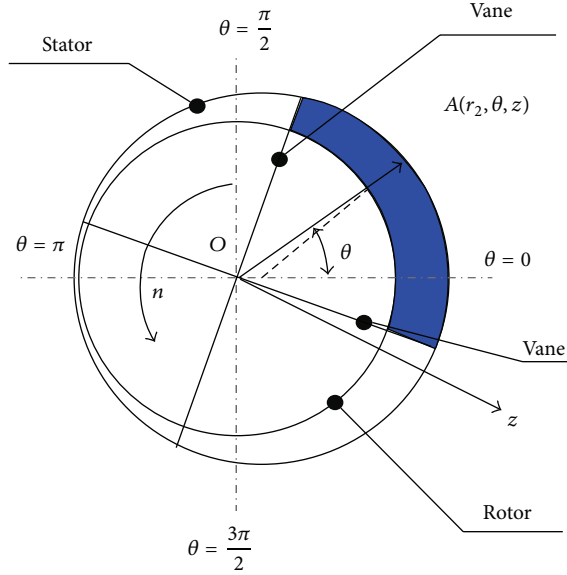


FIGURE 3: The melt conveying model in a chamber of VCPU.

A cross section of the melt conveying zone in the vane extruder is shown in Figure 3. To simplify the melt conveying process and allow for an analytical solution, the following assumptions are made:

- (i) The chamber is always filled with polymer melt, even when the volume changes with the rotation of the rotor.
- (ii) The melt in the vane chamber is always in isothermal laminar flow.
- (iii) The melt in vane chamber is incompressible.
- (iv) Leakage and the influence of the thickness of each vane and its geometry are neglected.
- (v) The influence of gravity is neglected.
- (vi) A Newtonian constitutive equation is used for the melt.

Using the above assumptions, the melt conveying model of the vane extruder can be analytically obtained.

Melt conveyance is examined in the melt-mixing zone of the fully filled chamber of the vane extruder. The Reynolds number was assumed to be much less than unity so that inertial effects are neglected. The governing equations for this situation are shown below.

Continuity Equation. Consider

$$\frac{1}{r} \frac{\partial v_\theta}{\partial \theta} + \frac{\partial v_z}{\partial z} = 0, \quad (2)$$

where r , θ , and z are cylindrical coordinate components, respectively; v_r , v_θ , and v_z are velocity components of r -direction, θ -direction, and z -direction.

Constitutive Equation. Consider

$$\tau = \mu \dot{\gamma}, \quad (3)$$

where τ is stress tensor; μ is viscosity coefficient dependent deformation rate; $\dot{\gamma}$ is rate of deformation tensor.

Motion Equations. Consider

$$\frac{\partial p}{\partial r} = -\frac{2\mu}{r^2} \frac{\partial v_\theta}{\partial \theta}, \quad (4)$$

$$\frac{1}{r} \frac{\partial p}{\partial \theta} = \mu \left[\frac{\partial}{\partial r} \left(\frac{1}{r} \frac{\partial}{\partial r} (r v_\theta) \right) + \frac{1}{r^2} \frac{\partial^2 v_\theta}{\partial \theta^2} \right], \quad (5)$$

$$\frac{\partial p}{\partial z} = \mu \left[\frac{1}{r} \frac{\partial}{\partial r} \left(r \frac{\partial v_z}{\partial r} \right) \right], \quad (6)$$

where p is pressure; r , θ , and z are cylindrical coordinate components, respectively; v_r , v_θ , and v_z are velocity components of r -direction, θ -direction, and z -direction; μ is viscosity coefficient dependent deformation rate. Furthermore, the boundary conditions are $v_z(r_0, \pi) = 0$ and $v_z(r_2, \pi/4) = 0$.

Equation (2) can be simplified to

$$\frac{\partial v_z}{\partial z} = -\frac{1}{r} \frac{\partial v_\theta}{\partial \theta}. \quad (7)$$

Taking the partial derivative of (7) with respect to z and assuming $\partial v_\theta / \partial z = 0$ gives

$$\frac{\partial^2 v_z}{\partial z^2} = -\frac{1}{r} \frac{\partial^2 v_\theta}{\partial \theta^2} = 0. \quad (8)$$

Melt velocity is assumed to vary linearly along the length of the extruder, $\partial v_z / \partial z = 0$. Thus, v_z can be defined as

$$v_z = f_1(r, \theta)z + f_2(r, \theta), \quad (9)$$

where f_1 and f_2 are only functions of r and θ .

Material enters the vane chamber at the origin of the z axis, $z = 0$; thus, the maximum axial velocity of melt occurs at the origin. In contrast, the velocity of the melt at the exit, $z = W$, in the most extreme case can be zero, $v_{z=W} = 0$. Substituting this boundary condition into (9) gives $f_2(r, \theta) = -f_1(r, \theta)W$. At the origin $z = 0$, the axial velocity of melt feeding into the vane chamber is $v_{z=0} = f_2(r, \theta) = -f_1(r, \theta)W$. Thus, (9) can be simplified to

$$v_z = v_{z0} \left(1 - \frac{z}{W} \right), \quad (10)$$

where W is the axial width of VCPU.

In contrast, the terminal end of the chamber discharges melt, so the axial velocity of melt at the terminal side is maximum, while at the origin, $z = 0$, the melt velocity is zero, $v_{z=0} = 0$. Substituting this boundary condition into (9), the following expression is obtained: $f_2(r, \theta) = 0$. The axial velocity of the melt at discharge from the vane chamber is $v_{z0} = f_1(r, \theta)W$. Thus, (9) can be further simplified to

$$v_z = v_{z0} \frac{z}{W}. \quad (11)$$

Assuming both sides of (4) and (5) are zero, and $\partial v_\theta / \partial z = 0$, the following expressions are obtained:

$$\begin{aligned} \frac{\partial^2 p}{\partial z \partial r} &= \frac{\partial}{\partial z} \left(-\frac{2\mu}{r^2} \frac{\partial v_\theta}{\partial \theta} \right) = 0, \\ \frac{1}{r} \frac{\partial^2 p}{\partial z \partial \theta} &= \frac{\partial}{\partial z} \left(\mu \left[\frac{\partial}{\partial r} \left(\frac{1}{r} \frac{\partial}{\partial r} (r v_\theta) \right) + \frac{1}{r^2} \frac{\partial^2 v_\theta}{\partial \theta^2} \right] \right) \\ &= 0. \end{aligned} \quad (12)$$

Examining (12), $\partial p / \partial z$ is independent of r and θ . Substituting (10) into (6) and rearranging give

$$\left(1 - \frac{z}{W}\right) \left[\frac{1}{r} \frac{\partial}{\partial r} \left(r \frac{\partial v_{z0}}{\partial r} \right) + \frac{1}{r^2} \frac{\partial^2 v_{z0}}{\partial \theta^2} \right] = \frac{1}{\mu} \frac{\partial p}{\partial z}. \quad (13)$$

In the geometry of a vane extruder, the circumferential distance is far greater than radial distance, and v_z is independent of θ ; that is, $\partial v_{z0} / \partial \theta = 0$. To solve for v_{z0} , we first examine the inlet, $z = 0$. Equation (13) can be simplified to

$$\frac{1}{r} \frac{\partial}{\partial r} \left(r \frac{\partial v_{z0}}{\partial r} \right) = \frac{1}{\mu} \frac{\partial p}{\partial z} \Big|_{z=0}. \quad (14)$$

The boundary conditions of (14) are (1) when $r = r_0$, $v_{z0} = 0$ and (2) when $r = r_2$, $v_{z0} = 0$.

Solving (14) gives

$$\begin{aligned} v_{z0} &= \frac{1}{4\mu} \left[(r^2 - r_0^2) - (r_2^2 - r_0^2) \frac{\ln r - \ln r_0}{\ln r_2 - \ln r_0} \right] \frac{\partial p}{\partial z} \Big|_{z=0}, \end{aligned} \quad (15)$$

where v_{z0} is the axial velocity of the melt at discharge from the vane chamber; p is pressure; μ is viscosity coefficient dependent deformation rate; r_2 is the radial coordinate value of the point of the inner arc of the stator; r_0 is the outer radius of the rotor; r and z are cylindrical coordinate component, respectively.

Substituting (15) into (10), the axial velocity v_z of melt flow in the vane chamber at the origin (feed location) is given by

$$\begin{aligned} v_z &= \frac{1}{4\mu} \left[(r^2 - r_0^2) - (r_2^2 - r_0^2) \frac{\ln r - \ln r_0}{\ln r_2 - \ln r_0} \right] \\ &\cdot \left(1 - \frac{z}{W}\right) \frac{\partial p}{\partial z} \Big|_{z=0}, \end{aligned} \quad (16)$$

where W is the axial width of VCPU and $(\partial p / \partial z)|_{z=0}$ can be obtained using the expression for volumetric flow rate:

$$Q = \iint v_{z0} r \, d\theta \, dr, \quad (17)$$

where Q is the rate of volume flow, $Q = dV/dt$; V is the volume of the vane chamber; and v_{z0} is the velocity of the melt entering the vane chamber.

Substituting (15) into (17) and rearranging give

$$\begin{aligned} \frac{1}{4\mu} \frac{\partial p}{\partial z} \Big|_{z=0} &\cdot \int_{\theta_r}^{\theta_f} \int_{r_0}^{r_2} \left[(r^2 - r_0^2) - (r_2^2 - r_0^2) \frac{\ln r - \ln r_0}{\ln r_2 - \ln r_0} \right] \\ &\cdot r \, dr \, d\theta = Q, \end{aligned} \quad (18)$$

where μ is viscosity coefficient dependent deformation rate; p is pressure; r and z are cylindrical coordinate components, respectively; θ_f is the angular coordinate of front vane; θ_r is the angular coordinate of rear vane; r_2 is the radial coordinate value of the point of the inner arc of the stator; r_0 is the outer radius of the rotor; Q is the rate of volume flow.

To simplify, the distance r_2 is defined as $r_2 \approx r_1 + (1/2)e(\cos \theta_f + \cos \theta_r)$, which can be substituted into (18):

$$\frac{\partial p}{\partial z} \Big|_{z=0} = \frac{4\mu Q}{k(\theta_r)}, \quad (19)$$

where

$$\begin{aligned} k(\theta_r) &= \frac{1}{4} (\theta_f - \theta_r) \left\{ - \left(r_1 + \frac{1}{2} e (\cos \theta_f + \cos \theta_r) \right)^4 \right. \\ &\left. + \frac{\left[(r_1 + (1/2) e (\cos \theta_f + \cos \theta_r))^2 - r_0^2 \right]^2}{\ln (r_1 + (1/2) e (\cos \theta_f + \cos \theta_r)) - \ln r_0} \right\}, \end{aligned} \quad (20)$$

where $k(\theta_r)$ is the function for simplification; θ_f is the angular coordinate of front vane; θ_r is the angular coordinate of rear vane; r_1 is the inner radius of the stator; r_0 is the outer radius of the rotor; e is the eccentricity between the center of the rotor and the center of the stator.

The same steps can be performed on the discharge process in the vane chamber, where the volumetric flow rate of melt discharge can be written as

$$Q = \iint v_{z0} r \, d\theta \, dr, \quad (21)$$

where Q is the rate of volume flow; v_{z0} is the axial velocity at the discharge point from the vane chamber; r and θ are cylindrical coordinate components, respectively.

At discharge, the volume of the chamber continues to shrink, so the volumetric flow rate is negative and the absolute value of Q must be used in (21).

Substituting (11) into (6) and setting $z = W$, the axial velocity of the melt at discharge is given by

$$\begin{aligned} v_{z0} &= \frac{1}{4\mu} \left[(r^2 - r_0^2) - (r_2^2 - r_0^2) \frac{\ln r - \ln r_0}{\ln r_2 - \ln r_0} \right] \frac{\partial p}{\partial z} \Big|_{z=W}. \end{aligned} \quad (22)$$

Substituting (22) into (21) gives the flow rate Q , which can then be substituted into (19). The pressure gradient of the melt flow along the z -axis at the discharge location is given by

$$\frac{\partial p}{\partial z} \Big|_{z=W} = -\frac{4\mu Q}{k(\theta_r)}, \quad (23)$$

where the value of $k(\theta_r)$ is given by (20).

Because the volume of the vane chamber varies periodically with the rotation of the rotor, there is a large change in chamber volume during the feeding process.

2.1. Axial Velocity

2.1.1. *Feeding Process* ($\pi/2 < \theta_r \leq 7\pi/4$). Substituting (19) into (16), the axial velocity v_z of the melt in the vane chamber at the inlet can be given by

$$v_z = \frac{Q}{k(\theta_r)} \left[(r^2 - r_0^2) - (r_2^2 - r_0^2) \frac{\ln r - \ln r_0}{\ln r_2 - \ln r_0} \right] \cdot \left(1 - \frac{z}{W} \right), \quad (24)$$

where r_2 is the radial coordinate of the point on the inner surface of the stator in the cylindrical coordinate system in which the origin is the center of the rotor and $r_2 = r_1 + e \cos \theta$. Here, r_1 is the inner radius of the stator, e is the eccentricity between the rotor and the stator, r_0 is the outer radius of the rotor, W is the axial width of the vane, and θ_r is the angular coordinate of the rear vane of the VCPU in the cylindrical coordinate system. In addition, Q is the volumetric flow rate of the vane chamber at the position θ_r . The value of Q is directly proportional to the speed of the rotor. The coefficient function $k(\theta_r)$ relates to the geometric parameters of the vane chamber and the position of vane.

2.1.2. *Discharge Process* ($-\pi/4 \leq \theta_r < \pi$). Substituting (22) and (23) into (11), the axial velocity v_z of melt in the vane chamber at the discharge point is given by

$$v_z = -\frac{Q}{k(\theta_r)} \left[(r^2 - r_0^2) - (r_2^2 - r_0^2) \frac{\ln r - \ln r_0}{\ln r_2 - \ln r_0} \right] \frac{z}{W}. \quad (25)$$

According to (24) and (25), the axial velocity v_z of melt in the VCPU is directly proportional to the speed of the rotor and is related to the geometric parameters of the vane chamber and the position of vane.

The elongational strain rate along the axis is defined in the cylindrical coordinate system in Figure 2 and can be calculated as

$$\dot{\gamma}_{zz} = 2 \frac{\partial v_z}{\partial z}, \quad (26)$$

$$= -\frac{2Q}{W \cdot k(\theta_r)} \left[(r^2 - r_0^2) - (r_2^2 - r_0^2) \frac{\ln r - \ln r_0}{\ln r_2 - \ln r_0} \right],$$

where $\dot{\gamma}$ is rate of deformation tensor; v_z is the velocity components of z -direction; r and z are the cylindrical coordinate components, respectively; r_0 is the outer radius of the rotor; r_2 is the radial coordinate value of the point of the inner arc of the stator; W is the axial width of VCPU; $k(\theta_r)$ is the function for simplification; Q is the rate of volume flow.

Note. The values of all parameters are identical to those given in (24) for the feeding process and to those given in (25) for the discharge process.

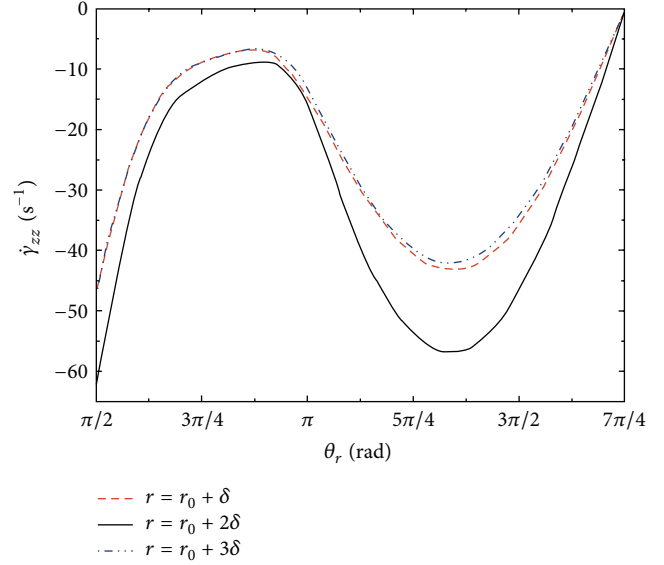


FIGURE 4: The axial tensile strain rate of melt moving in a chamber of VCPU: feed process.

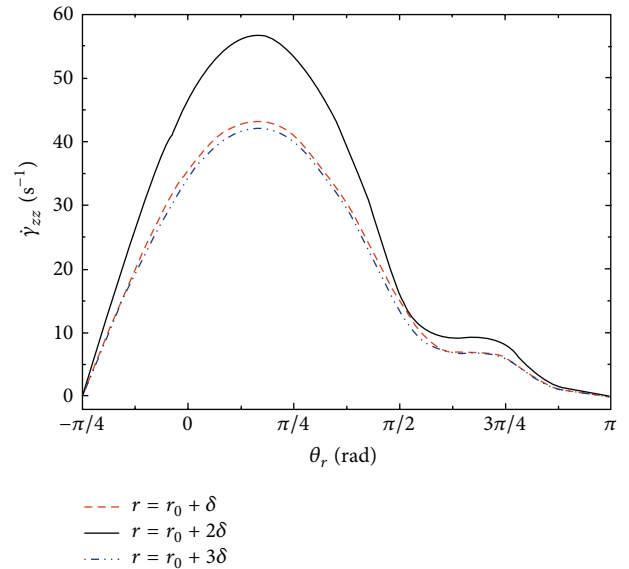


FIGURE 5: The axial tensile strain rate of melt moving in a chamber of VCPU: discharge process.

For example, $r_0 = 20$ mm, $r_1 = 23$ mm, $e = 3$ mm, $W = 35$ mm, and the rotation speed of the rotor $N = 60$ rpm.

The relationship of the axial elongational strain rate of melt moving in the chamber $\dot{\gamma}_{zz}$ and the circumferential position of the rear vane θ_r is shown in Figures 4 and 5.

3. Mathematical Model

3.1. *Governing Equations.* In Figures 4 and 5, the axial rate of strain of the melt $\dot{\gamma}_{zz} < 0$ at the inlet, but $\dot{\gamma}_{zz} > 0$. In brief, the axial strain rate is at a maximum for a given circumferential position, namely, $r = r_0 + 2\delta$, and others in inner arc surface

of stator or in outer arc surface of rotor are smaller; that is, $r = r_0 + \delta$ or $r = r_0 + 3\delta$, where δ is the dimensionless gap.

3.2. Circumferential Velocity

3.2.1. *Feeding Process.* Substituting (24) into continuity (2), the expression can be simplified:

$$\frac{\partial v_\theta}{\partial \theta} = \frac{Q \cdot r}{W \cdot k(\theta_r)} \left[(r^2 - r_0^2) - (r_2^2 - r_0^2) \frac{\ln r - \ln r_0}{\ln r_2 - \ln r_0} \right] \cdot (\theta - \theta_r). \quad (27)$$

The boundary conditions of melt circumferential velocity are as follows: (1) when $\theta = \theta_r$, $v_\theta = \omega r$; (2) when $r = r_0$, $v_\theta = \omega r_0$. Substituting these boundary conditions into (27), the circumferential velocity v_θ can be obtained:

$$v_\theta = \omega r + \frac{Q \cdot r}{W \cdot k(\theta_r)} \left[(r^2 - r_0^2) - (r_2^2 - r_0^2) \frac{\ln r - \ln r_0}{\ln r_2 - \ln r_0} \right] \cdot (\theta - \theta_r). \quad (28)$$

3.2.2. *Discharge Process.* Similarly, substituting (29) into continuity (2), the circumferential velocity v_θ matches the expression given by (28).

4. Results and Discussion

4.1. *Elongational Strain Rate in the Circumferential Direction.* The elongational strain rate in the circumferential direction is defined in the cylindrical coordinate system in Figure 2 and given below:

$$\dot{\gamma}_{\theta\theta} = \frac{2}{r} \frac{\partial v_\theta}{\partial \theta}, \quad (29)$$

$$\dot{\gamma}_{\theta\theta} = \frac{2Q}{W \cdot k(\theta_r)} \left[(r^2 - r_0^2) - (r_2^2 - r_0^2) \frac{\ln r - \ln r_0}{\ln r_2 - \ln r_0} \right]. \quad (30)$$

Note. The values of all parameters are identical to those given in (28) in both the feeding and the discharge processes.

For example, $r_0 = 20$ mm, $r_1 = 23$ mm, $e = 3$ mm, $W = 35$ mm, and the rotational speed of the rotor $N = 60$ rpm.

The relationship between the axial elongational strain rate of melt moving in a chamber of the VCPU $\dot{\gamma}_{\theta\theta}$ and the circumferential position of rear vane θ_r is shown in Figures 6 and 7.

In Figures 6 and 7, the circumferential strain rate of the melt $\dot{\gamma}_{\theta\theta} > 0$ at the inlet, but $\dot{\gamma}_{\theta\theta} < 0$. In brief, the value of the circumferential strain rate is maximum at any given circumferential position in the vane chamber, namely, $r = r_0 + 2\delta$, and others in inner arc surface of stator or in outer arc surface of rotor are smaller, namely, $r = r_0 + \delta$ or $r = r_0 + 3\delta$.

4.2. *Pressure Distribution in the Vane Extruder.* In the melt conveying section, the polymer is driven circumferentially

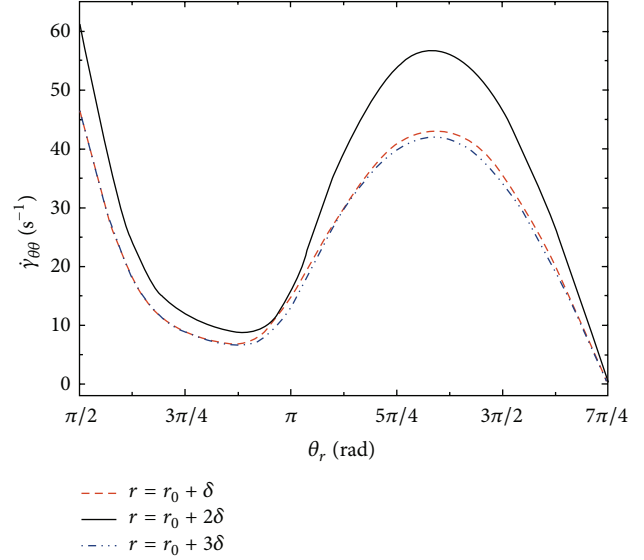


FIGURE 6: The circumferential tensile strain rate of melt moving in a chamber of VCPU: feed process.

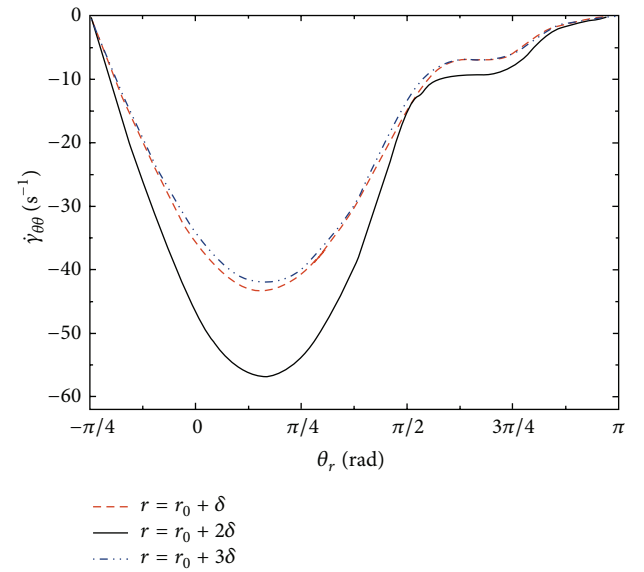


FIGURE 7: The circumferential tensile strain rate of melt moving in a chamber of VCPU: discharge process.

through the VCPU by a rear vane and motion of the rotor. In addition, the VCPU produces positive displacement of the melt, conveying it in the axial direction as the volume of the chamber changes periodically. The axial and circumferential velocity of the melt is different in every position in the vane extruder. Similarly, the axial and circumferential pressure in the melt vary continuously throughout the extruder.

4.2.1. *Pressure Distribution in the Axial Direction at the Inlet.* Substituting (24) into the motion equation (6) and simplifying give

$$\frac{\partial p}{\partial z} = \frac{4\mu Q}{k(\theta_r)} \left(1 - \frac{z}{W} \right), \quad (31)$$

where the values of all variables including Q and $k(\theta_r)$ are identical to those given in (6).

Because the volumetric rate along the axis $Q > 0$ and the coefficient function $k(\theta_r) < 0$, $\partial p/\partial z \leq 0$ at the inlet to the vane chamber. This means that the pressure within the vane chamber decreases gradually from the inlet to the outlet of the chamber. As a normal stress field in the axial direction is produced in the vane chamber, melt is conveyed forcibly forward.

The axial pressure difference from the inlet to a point in the vane chamber can be given by

$$\Delta p_z = - \int_0^z \frac{\partial p}{\partial z} dz, \quad (32)$$

where Δp_z is the pressure difference for z -direction.

Substituting (31) into (32), the following expression can be obtained:

$$\Delta p_z = \frac{2\mu Q}{k(\theta_r)} \left(\frac{z^2}{W} - 2z \right). \quad (33)$$

With $z = W$, the axial pressure difference from the inlet ($z = 0$) to the outlet is given by

$$\Delta p_z = - \frac{2\mu Q W}{k(\theta_r)}. \quad (34)$$

4.2.2. Pressure Distribution in the Circumferential Direction at the Inlet. Substituting (28) into the motion equation (6) and simplifying give

$$\frac{\partial p}{\partial \theta} = \frac{2\mu Q}{W \cdot k(\theta_r)} \left[4r^2 - \frac{r_2^2 - r_0^2}{\ln r_2 - \ln r_0} \right] (\theta - \theta_r), \quad (35)$$

where the values of all variables, including Q and $k(\theta_r)$, are identical to those given in (6).

Because the volumetric axial flow rate $Q > 0$ and the coefficient function $k(\theta_r) < 0$, $\theta - \theta_r \geq 0$, $4r^2 - (r_2^2 - r_0^2)/(\ln r_2 - \ln r_0) > 0$, and $\partial p/\partial \theta \leq 0$ in the entire range $\theta_r \leq \theta \leq \theta_f$ of the vane chamber. Thus, the circumferential pressure decreases gradually within the vane chamber from rear vane to front vane. The inner arc of the stator gradually moves away from the rotor so that negative pressure is produced in the front of the vane chamber along with the periodic volume expansion of the melt. The circumferential pressure difference from the edge of the chamber ($\theta = \theta_r$) to a point within the vane chamber is given by

$$\Delta p_\theta = - \int_{\theta_r}^{\theta} \frac{\partial p}{\partial \theta} d\theta, \quad (36)$$

where Δp_θ is the pressure difference for θ -direction.

Substituting (35) into (36) and setting $r = (r_0 + r_2)/2$ give

$$\Delta p_\theta = \frac{\mu Q}{W \cdot k(\theta_r)} \left[\frac{r_2^2 - r_0^2}{\ln r_2 - \ln r_0} - (r_0 + r_2)^2 \right] (\theta - \theta_r)^2. \quad (37)$$

At $\theta = \theta_f$, the circumferential pressure difference from the extreme side ($\theta = \theta_r$) to the front side is given by

$$\Delta p_\theta = \frac{\mu Q}{W \cdot k(\theta_r)} \left[\frac{r_2^2 - r_0^2}{\ln r_2 - \ln r_0} - (r_0 + r_2)^2 \right] (\theta_f - \theta_r)^2, \quad (38)$$

where θ_f and θ_r are the most front and the most rear circumferential coordinates, respectively. When $\pi \leq \theta_r \leq 7\pi/4$, $\theta_f - \theta_r = \pi/2$; when $\pi/2 < \theta_r < \pi$, $\theta_f - \theta_r = \theta_r - \pi/2$.

Synthesizing (30) and (37), the characteristic pressure function at the inlet is given by

$$p = p_i + \frac{2\mu Q}{k(\theta_r)} \left(2z - \frac{z^2}{W} \right) + \frac{\mu Q}{W \cdot k(\theta_r)} \left[(r_0 + r_2)^2 - \frac{r_2^2 - r_0^2}{\ln r_2 - \ln r_0} \right] \cdot (\theta - \theta_r)^2, \quad (39)$$

where p_i is the pressure at the edge of the vane chamber ($z = 0$, $\theta = \theta_r$).

A gap is produced due to the volume enlargement at the front vane in the vane chamber, and the final side of the chamber can be filled with melt. The pressure at the front of the vane in the vane chamber is therefore roughly equal to atmospheric pressure; that is, $p(\theta_f, W) = p_0$. Substituting into (36) gives

$$p_i = p_0 - \frac{2\mu Q W}{k(\theta_r)} - \frac{\mu Q \pi^2}{4W \cdot k(\theta_r)} \left[(r_0 + r_2)^2 - \frac{r_2^2 - r_0^2}{\ln r_2 - \ln r_0} \right], \quad (40)$$

where p_i is the pressure at the final side of the vane chamber; p_0 is the atmospheric pressure; μ is viscosity coefficient dependent deformation rate; Q is the rate of volume flow; W is the axial width of VCPU; $k(\theta_r)$ is the function for simplification; r_0 is the outer radius of the rotor; r_2 is the radial coordinate value of the point of the inner arc of the stator.

4.2.3. Pressure Distribution in the Axial Direction at the Outlet. Substituting (25) into the motion equation (6) and simplifying give

$$\frac{\partial p}{\partial z} = - \frac{4z\mu Q}{W \cdot k(\theta_r)}. \quad (41)$$

Substituting (41) into (32) gives

$$\Delta p_z = \frac{2\mu Q z^2}{W \cdot k(\theta_r)}. \quad (42)$$

At $z = W$, the axial pressure difference from the inlet to the outlet is given by

$$\Delta p_z = \frac{2\mu Q W}{k(\theta_r)}. \quad (43)$$

4.2.4. *Pressure Distribution in the Circumferential Direction at the Outlet.* The circumferential pressure differential expression is identical to (37).

Combining (43) and (37), the characteristic pressure function at the outlet of the vane chamber is given by

$$p = p_0 + \frac{2\mu Q(z - W)^2}{W \cdot k(\theta_r)} - \frac{\mu Q}{W \cdot k(\theta_r)} \left[(r_0 + r_2)^2 - \frac{r_2^2 - r_0^2}{\ln r_2 - \ln r_0} \right] \cdot (\theta - \theta_f)^2, \quad (44)$$

where p is the pressure; p_0 is the atmospheric pressure.

5. Conclusions

The above analysis supports a number of conclusions:

- (i) The polymer melt conveying process in the vane extruder is completely different from the process in conventional screw extruders.
- (ii) The pressure within the chamber is influenced by the location and volume within the chamber.
- (iii) The dynamics of melt conveyance in a vane chamber depend mostly on pressure to overcome viscous forces. Therefore, the power consumption of a vane extruder increases with pressure and viscosity within the chamber and is directly proportional to the speed of the rotor.

Nomenclatures

r, θ, z :	Cylindrical coordinate, mm, mm, mm
O :	The origin of the cylindrical coordinate system, that is, the center of the rotor
O_1 :	The center of the stator
r_0 :	The outer radius of the rotor, mm
r_1 :	The inner radius of the stator, mm
W :	The axial width of VCPU, mm
r_2 :	The radial coordinate value of the point of the inner arc of the stator, mm
e :	The eccentricity between the center of the rotor and the center of the stator, mm
Δr_v :	The extend length of vane, mm
θ_f :	The angular coordinate of front vane, rad
θ_r :	The angular coordinate of rear vane, rad
τ :	Stress tensor, N/cm ²
μ :	Viscosity coefficient dependent deformation rate
$\dot{\gamma}$:	Rate of deformation tensor, s ⁻¹
p :	Pressure, N/cm ²
v_r, v_θ, v_z :	Velocity components of r -direction, θ -direction, and z -direction, cm/s
f_1, f_2 :	Arbitrary functions for r and θ
Q :	The rate of volume flow

V :	The volume of vane chamber
v_{z0} :	The velocity of feeding melt at the inlet of the vane chamber
$k(\theta_r)$:	The function for simplification
N :	The rotational speed of the rotor, rpm
δ :	The dimensionless gap
$\Delta p_\theta, \Delta p_z$:	The pressure difference for θ -direction and z -direction
p_i :	The pressure at the final side of the vane chamber
p_0 :	The atmospheric pressure.

Conflict of Interests

The author declares that there is no conflict of interests regarding the publication of this paper.

Acknowledgments

The author wishes to acknowledge the Guangzhou Science and Technology Plan Project (201541) and the "Innovation and Strengthen University" Project of Guangzhou Maritime Institute (A330106, B510647) for financial support.

References

- [1] B. Yang and L. J. Lee, "Process control of profile extrusion using thermal method. Part I: mathematical modeling and system analysis," *Polymer Engineering & Science*, vol. 28, no. 11, pp. 697–707, 1988.
- [2] B. Yang and L. J. Lee, "Process control of profile extrusion using thermal method. Part II: closed loop control," *Polymer Engineering Science*, vol. 28, no. 11, pp. 708–717, 1988.
- [3] E. Broyer, C. Gutfinger, and Z. Tadmor, "Evaluating flows of non-Newtonian fluids by the method of equivalent Newtonian viscosity," *AIChE Journal*, vol. 21, no. 1, pp. 198–200, 1975.
- [4] M. V. Brusckhe and S. G. Advani, "Flow of generalized Newtonian fluids across a periodic array of cylinders," *Journal of Rheology*, vol. 37, no. 3, p. 479, 1993.
- [5] F. W. Kroesser and S. Middleman, "The calculation of screw characteristics for the extrusion of non-Newtonian melts," *Polymer Engineering & Science*, vol. 5, no. 4, pp. 230–234, 1965.
- [6] R. M. Griffith, "Fully developed flow in screw extruders. Theoretical and experimental study," *Industrial & Engineering Chemistry Fundamentals*, vol. 1, no. 3, pp. 180–187, 1962.
- [7] H. J. Zamodits, "Flow of polymer melts in extruders. Part I. the effect of transverse flow and of a superposed steady temperature profile," *Journal of Rheology*, vol. 13, no. 3, p. 357, 1969.
- [8] D. F. Dyer, "A numerical solution for the single-screw extrusion of a polymer melt," *AIChE Journal*, vol. 15, no. 6, pp. 823–828, 1969.
- [9] E. E. Agur and J. Vlachopoulos, "Numerical simulation of a single-screw plasticating extruder," *Polymer Engineering & Science*, vol. 22, no. 17, pp. 1084–1094, 1982.
- [10] C. D. Han, K. Y. Lee, and N. C. Wheeler, "An experimental study on plasticating single-screw extrusion," *Polymer Engineering & Science*, vol. 30, no. 24, pp. 1557–1567, 1990.
- [11] J. Brandao, E. Spieth, and C. Lekakou, "Extrusion of polypropylene. Part I. Melt rheology," *Polymer Engineering and Science*, vol. 36, no. 1, pp. 49–55, 1996.

- [12] C. Lekakou and J. Brandao, "Extrusion of polypropylene. Part II: process analysis of the metering zone," *Polymer Engineering & Science*, vol. 36, no. 1, pp. 56–64, 1996.
- [13] J. Zhang and J.-P. Qu, "Nonlinear viscoelasticity of polymer melts in electromagnetic vibration force field," *Nonlinear Analysis, Theory, Methods & Applications*, vol. 63, no. 5–7, pp. e977–e984, 2005.
- [14] J. P. Qu, "Study on the pulsating extrusion characteristics of polymer melt through round-sectioned die," *Polymer-Plastics Technology and Engineering*, vol. 41, no. 1, pp. 115–132, 2002.
- [15] W. Quan, J.-P. Qu, and H. Liang, "Effect of vibration parameters of electromagnetic dynamic plastics injection molding machine on mechanical properties of polypropylene samples," *Journal of Applied Polymer Science*, vol. 102, no. 2, pp. 972–976, 2006.
- [16] G. S. Zeng, C. Xu, Y. J. Liu, and J. Qu, "Hysteresis heat build-up and low temperature processing of polymer under the vibration force field," *Advanced Materials Research*, vol. 415–417, pp. 200–204, 2012.
- [17] J.-P. Qu, Z.-T. Yang, X.-C. Yin, H.-Z. He, and Y.-H. Feng, "Characteristics study of polymer melt conveying capacity in vane plasticization extruder," *Polymer-Plastics Technology and Engineering*, vol. 48, no. 12, pp. 1269–1274, 2009.
- [18] J.-P. Qu, X.-Q. Zhao, J.-B. Li, and S.-Q. Cai, "Power consumption in the compacting process of polymer particulate solids in a vane extruder," *Journal of Applied Polymer Science*, vol. 127, no. 5, pp. 3923–3932, 2013.
- [19] J.-P. Qu, G.-Z. Zhang, H.-Z. Chen, X.-C. Yin, and H.-Z. He, "Solid conveying in vane extruder for polymer processing: effects on pressure establishment," *Polymer Engineering & Science*, vol. 52, no. 10, pp. 2147–2156, 2012.

Research Article

An Investigation of the Effect of Chitosan on Isothermal Crystallization, Thermal Decomposition, and Melt Index of Biodegradable Poly(L-lactic acid)

Yan-Hua Cai and Li-Sha Zhao

Chongqing Key Laboratory of Environmental Materials & Remediation Technologies,
Chongqing University of Arts and Sciences, Yongchuan, Chongqing 402160, China

Correspondence should be addressed to Yan-Hua Cai; caiyh651@aliyun.com

Received 30 July 2015; Accepted 15 October 2015

Academic Editor: Heitor L. Ornaghi

Copyright © 2015 Y.-H. Cai and L.-S. Zhao. This is an open access article distributed under the Creative Commons Attribution License, which permits unrestricted use, distribution, and reproduction in any medium, provided the original work is properly cited.

Biodegradable chitosan (CS) was introduced into another biodegradable poly(L-lactic acid) (PLLA) to prepare the PLLA/CS composites, and the effect of CS on thermal behavior and melt index of PLLA was investigated using modern testing technologies including optical depolarizer, thermogravimetric analysis instrument, and melt index instrument. The relevant testing results showed that both crystallization temperature and CS concentration affected the isothermal crystallization behavior of PLLA. Compared to neat PLLA, the $t_{1/2}$ of PLLA/5% CS decreased from 2991.54 s to the minimum value 208.76 s at 105°C. However, the $t_{1/2}$ of PLLA/CS composites in high crystallization temperature zone was different from that in low crystallization temperature zone. The increase of CS concentration and heating rate made the thermal decomposition temperature of PLLA/CS composites shift to higher temperature. The melt index results indicated that 3% CS made the fluidity of PLLA become better.

1. Introduction

Chitosan (CS) with the advantage of being nontoxic, as a very valuable biodegradable and biocompatible material, has numerous applications in biomedical science [1, 2], materials science [3], waste water treatment [4], inhibitors [5], and so forth. The work about in vitro antioxidant activity of CS scaffold materials indicated that the concentration and molecular weight of CS significantly affected the free radical scavenging ability, and the optimal concentration was 0.2 mg/mL and the carboxymethyl chitosan possessed higher scavenging ability [6]. Pandele and his colleagues prepared the CS/graphene oxide films using solution blending technology. And the addition of 6% graphene oxide made Young's modulus and tensile strength values exceed those of nacre by about 60 and 20%, and a high cell proliferation rate for the composite films with high graphene oxide content was confirmed by biocompatibility assays [7]. In the aspect of adsorbent, 8-hydroxyquinoline-2-carboxaldehydechitosan (CSHQ) Schiff base derived from CS and 8-hydroxyquinoline carboxaldehyde were synthesized to remove copper from aqueous

media. The experimental results suggested that CSHQ would be a promising adsorbent for water treatment, and the adsorption of Cu(II) onto CSHQ Schiff base depended on the PH value. Meantime, those results also showed that the Cu(II) adsorption process onto CSHQ obeyed the Langmuir isotherm model well [8]. To improve interfacial adhesion, the CS was used to be as a coupling agent, and the effects of CS with different addition amounts and particle sizes on the thermal properties of polyvinyl chloride/wood flour composites were investigated. The addition of 30 phr CS with the particle size of 180–220 mesh could elevate thermal properties of polyvinyl chloride/wood flour composites [9]. In addition, Wei and his colleagues constructed poly(ethylene oxide)/CS environmentally friendly composites, and these composites processed excellent mechanical properties, thermal stabilities, and shape-memory behavior, with the increase of poly(ethylene oxide) content; Young's modulus and maximum tensile strength exhibited a decrease, but the elongation at break presented an increase [10].

Poly(L-lactic acid) (PLLA) is also typical biodegradable thermoplastic polymer materials as CS. Furthermore, with

the development of science technology, PLLA has been applied in many fields such as food packaging, automobile, and electronic industry [11–13]. However, there exist some disadvantages including low crystallization degree and slow crystallization rate to restrict the application in more fields. Thus, many related literatures were reported to improve these drawbacks. To improve the crystallization ability of PLLA, Yang et al. [14] investigated the synergistic effect of poly(ethylene glycol) and graphene oxides on the crystallization behavior of PLLA. The results illustrated that poly(ethylene glycol) could improve the chain mobility of PLLA, and graphene oxides acted as the effective nucleation agent to accelerate the crystallization rate of PLLA, respectively. Furthermore, simultaneous addition of both poly(ethylene glycol) and graphene oxides could cause a synergistic effect to improve the crystallization ability of PLLA. Similarly, Chen et al. [15] also confirmed that graphene oxides exhibited nucleation effect for PLLA crystallization. However, the report showed that the presence of the graphene oxides accelerated the thermal degradation of PLLA and resulted in the decrease of PLLA molecular weight.

In this paper, biodegradable CS was introduced into another biodegradable PLLA to prepare the PLLA/CS composites, and the effect of CS on thermal decomposition, isothermal crystallization, and the fluidity of PLLA was investigated. The relevant results may make PLLA/CS exhibit a promising application in biodegradable materials.

2. Experiment

2.1. Materials. Poly(L-lactic acid) (2002D) was purchased from Nature Works LLC (USA). Chitosan was obtained from Mianyang Rongsheng Chemical Reagents Company in Sichuan province in China.

2.2. Preparation of PLLA/CS Composites. PLLA and CS were dried for 24 h before blending, and the blending process of PLLA and CS was similar to that of our previous paper [16].

2.3. Test

2.3.1. Isothermal Crystallization Measurement. Isothermal crystallization of PLLA/CS composites was carried out by GJY-III optical depolarizer (Donghua University, China) in the region from 100°C to 120°C.

2.3.2. Thermal Decomposition. The Q500 thermogravimetric analysis (TGA) (TA Instruments-Waters LLC, USA) was used to investigate the thermal decomposition behavior with different heating rate under air flow (50 mL/min).

2.3.3. Melt Index. The fluidity of PLLA and PLLA/CS composites was measured by melt index instrument (Beijing Guance Testing Instrument Co., Ltd., China), the measurement temperature was 180°C, and load is 10 Kg.

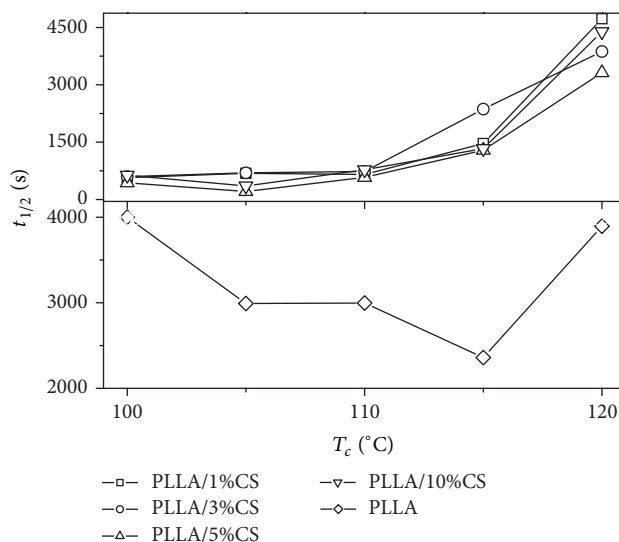


FIGURE 1: The $t_{1/2}$ of PLLA and PLLA/CS at different crystallization temperature.

3. Results and Discussion

3.1. Thermal Behavior of PLLA/CS Composites. Isothermal crystallization behavior of PLLA/CS composites was investigated. It is observed from Figure 1 that the addition of CS makes the half time of overall crystallization $t_{1/2}$ of PLLA significantly decrease, which indicates that CS can serve as the nucleating agent for PLLA. What is more, it is also clear that both crystallization temperature and CS concentration affect the isothermal crystallization behavior of PLLA. Particularly, the $t_{1/2}$ of PLLA is significantly affected by CS concentration in low-temperature section. Upon the addition of 5% CS, compared to the neat PLLA, the $t_{1/2}$ of PLLA decreases from 2991.54 s to the minimum value 208.76 s at 105°C. In contrast, this phenomenon is different in high-temperature section (above 115°C); what is worse, the addition of CS makes the $t_{1/2}$ of PLLA increase, and the $t_{1/2}$ of the most PLLA with CS is longer than that of the neat PLLA; the reason is that the increasing of movement ability of PLLA molecular chain in high-temperature section makes PLLA not obtain regular structure. At the same time, this phenomenon also indicates that the crystallization temperature is one of the most crucial factors for crystallization process of PLLA.

In addition, Figure 1 also indicates that different CS concentration can exhibit different crystallization behavior; the trend of influence of CS concentration on the crystallization behavior of PLLA is the addition of CS can make the $t_{1/2}$ of PLLA decrease, and upon the addition of 5% CS, the $t_{1/2}$ appears as the minimum value.

The isothermal crystallization kinetics of PLLA/CS composites were described using Avrami equation. It is very clear that the relationship of $\log[-\ln(I_{\infty} - I_t)/(I_{\infty} - I_0)]$ versus $\log t$ is linear (see Figure 2), which indicated that Avrami equation is viable for describing the crystallization process of PLLA and PLLA/CS composites.

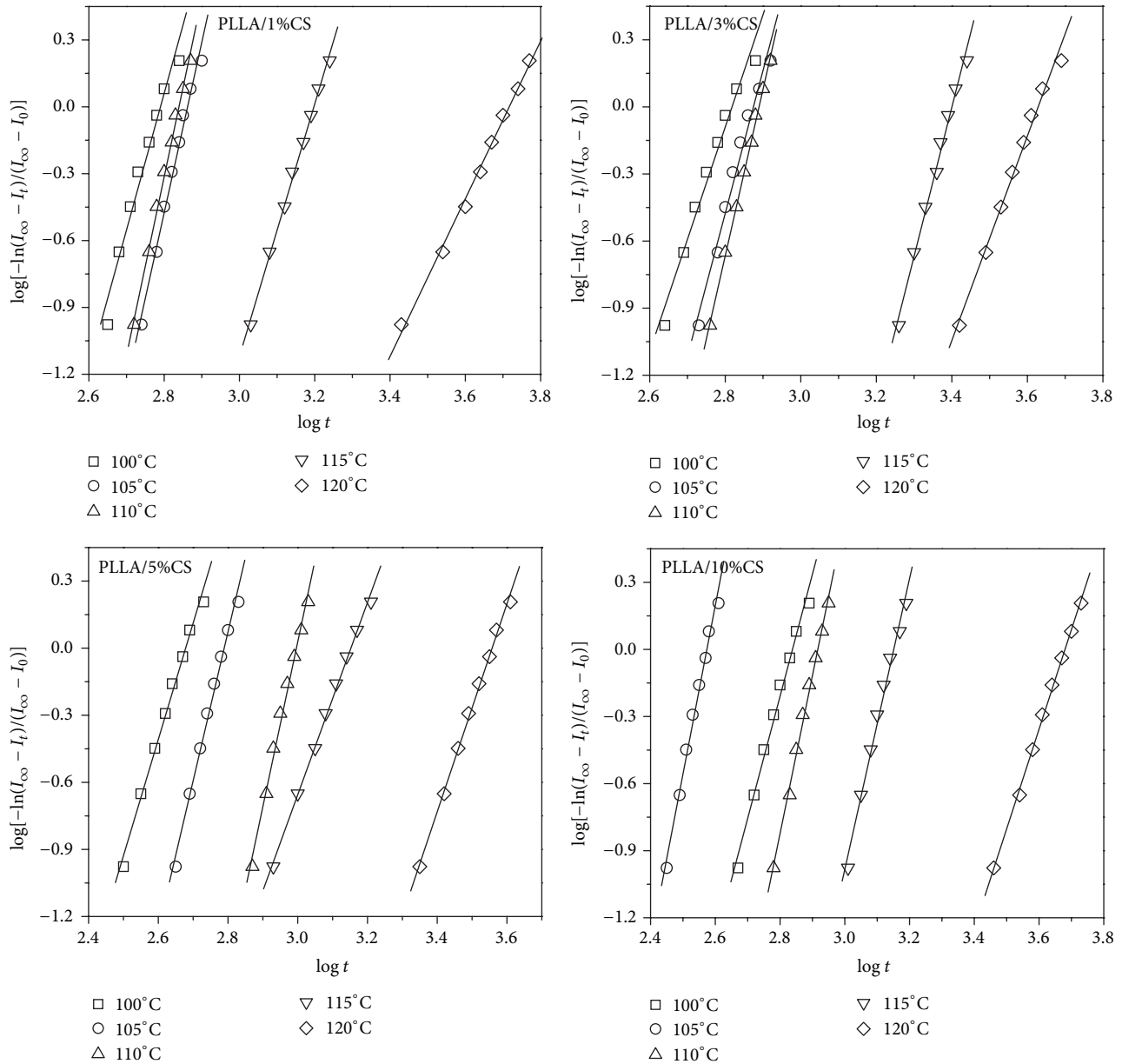


FIGURE 2: The Avrami plots for PLLA/CS composites at different temperature.

The thermal decomposition of PLLA with different CS concentration was shown in Figure 3. As shown in Figure 3, the onset thermal decomposition temperature (T_0) of PLLA/CS composites increases from 345.2°C to 347°C with increasing of CS content from 1% to 5%, and the thermal decomposition temperature is also affected by heating rate at the same CS content. Figure 4 shows the effect of the heating rate on the thermal decomposition temperature of PLLA/10% CS composites. The thermal decomposition trend of PLLA/10% CS composites at different heating rate is similar, and the T_0 of PLLA/10% CS composites increases with an increase of heating rate, resulting from the thermal inertia,

and the T_0 at heating rate of 3, 5, 10, 15, and 20°C/min are 326.9°C, 335°C, 350.7°C, 354°C, and 355.8°C, respectively.

3.2. Melt Index of PLLA/CS Composites. It is well-known that the addition of additive can affect the fluidity of polymer. Here, the melt index of PLLA/CS composites was investigated to reveal the influence of CS on the fluidity of PLLA. The dates from Figure 5 show that the melt mass flow rate (MFR) increases with increasing of CS content, and MFR appears as the maximum value upon the addition of 3% CS, which indicates that 3% CS can make the fluidity of PLLA become better. However, the change trend of MFR of PLLA/CS

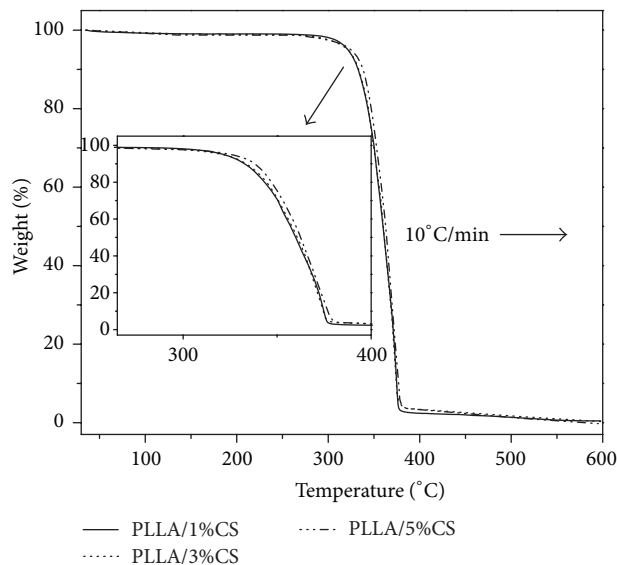


FIGURE 3: The thermal decomposition of PLLA with different CS at a heating rate of 10°C/min.

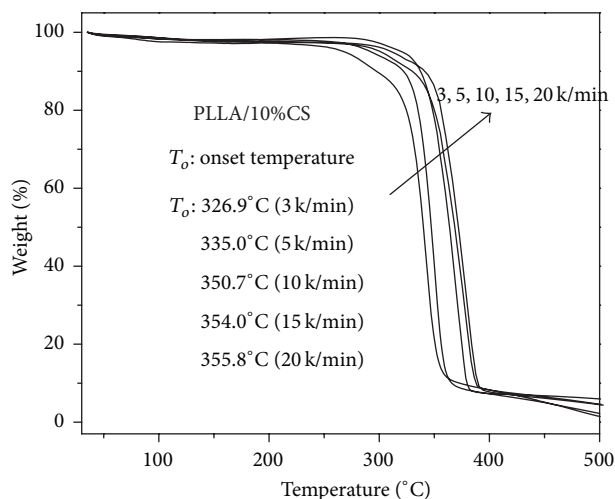


FIGURE 4: The thermal decomposition of PLLA/10% CS at different heating rate.

composites is irregular; this phenomenon suggested that influence of CS on the fluidity of PLLA is very complicated; on the other hand, this phenomenon may result from the accuracy of measure instrument.

4. Conclusion

The isothermal crystallization behavior, thermal decomposition, and the fluidity of PLLA with different CS content were investigated, and isothermal crystallization behavior showed that CS could serve as the nucleating agent for PLLA, and 5% CS made the $t_{1/2}$ of PLLA exhibit the minimum value at 105°C. The dates from thermal decomposition experiment suggested that the onset thermal decomposition temperature T_o of PLLA/CS composites increased with increasing of CS

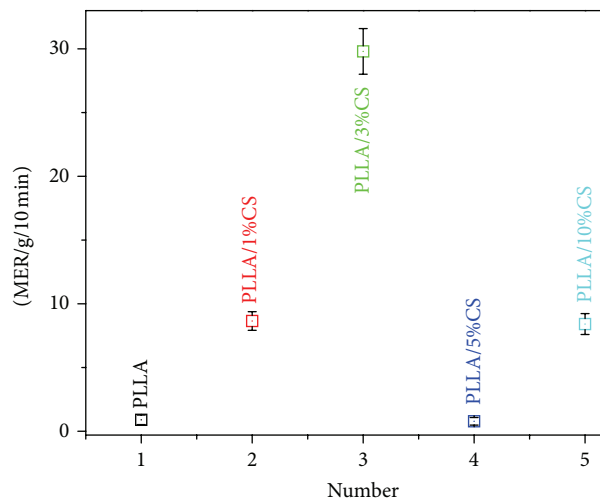


FIGURE 5: The effect of CS content on MFR of PLLA.

content. In addition, the heating rate also affected the T_o . The melt index of PLLA/CS composites indicated that 3% CS made the fluidity of PLLA become better, but the influence trend of CS on the fluidity of PLLA was very complicated.

Conflict of Interests

The authors declare that there is no conflict of interests regarding the publication of this paper.

Acknowledgments

This work was supported by National Natural Science Foundation of China (Project no. 51403027), Natural Science Foundation Project of CQ CSTC (Project no. cstc2012jjA50001), Foundation of Chongqing Municipal Education Commission (Project no. KJ131202), and Chongqing University of Arts and Sciences (Project no. R2013CH11).

References

- [1] S. Vimal, S. Abdul Majeed, G. Taju et al., "Chitosan tripolyphosphate (CS/TPP) nanoparticles: preparation, characterization and application for gene delivery in shrimp," *Acta Tropica*, vol. 128, no. 3, pp. 486–493, 2013.
- [2] A. Islam, T. Yasin, and I. U. Rehman, "Synthesis of hybrid polymer networks of irradiated chitosan/poly(vinyl alcohol) for biomedical applications," *Radiation Physics and Chemistry*, vol. 96, pp. 115–119, 2014.
- [3] X. Xia, Z. Zheng, Y. Zhang, X. Zhao, and C. Wang, "Synthesis of Ag-MoS₂/chitosan nanocomposite and its application for catalytic oxidation of tryptophan," *Sensors and Actuators B: Chemical*, vol. 192, pp. 42–50, 2014.
- [4] G. Crini and P.-M. Badot, "Application of chitosan, a natural aminopolysaccharide, for dye removal from aqueous solutions by adsorption processes using batch studies: a review of recent literature," *Progress in Polymer Science*, vol. 33, no. 4, pp. 399–447, 2008.

- [5] M. Li, J. Xu, R. Li et al., "Simple preparation of aminothiurea-modified chitosan as corrosion inhibitor and heavy metal ion adsorbent," *Journal of Colloid and Interface Science*, vol. 417, pp. 131–136, 2014.
- [6] H. Li, Q. Xu, Y. Chen, and A. Wan, "Effect of concentration and molecular weight of chitosan and its derivative on the free radical scavenging ability," *Journal of Biomedical Materials Research Part A*, vol. 102, no. 3, pp. 911–916, 2014.
- [7] A. M. Pandele, S. Dinescu, M. Costache et al., "Preparation and in vitro, bulk, and surface investigation of chitosan/graphene oxide composite films," *Polymer Composites*, vol. 34, no. 12, pp. 2116–2124, 2013.
- [8] D. H. K. Reddy and S.-M. Lee, "Synthesis and characterization of a chitosan ligand for the removal of copper from aqueous media," *Journal of Applied Polymer Science*, vol. 130, no. 6, pp. 4542–4550, 2013.
- [9] K. Xu, K. Li, T. Zhong, L. Guan, C. Xie, and S. Li, "Effects of chitosan as biopolymer coupling agent on the thermal and rheological properties of polyvinyl chloride/wood flour composites," *Composites Part B: Engineering*, vol. 58, pp. 392–399, 2014.
- [10] H. Wei, F. Zhang, D. Zhang, Y. Liu, and J. Leng, "Shape-memory behaviors of electrospun chitosan/poly(ethylene oxide) composite nanofibrous membranes," *Journal of Applied Polymer Science*, vol. 132, no. 37, pp. 42532.1–42532.9, 2015.
- [11] D. Longano, N. Ditaranto, N. Cioffi et al., "Analytical characterization of laser-generated copper nanoparticles for antibacterial composite food packaging," *Analytical and Bioanalytical Chemistry*, vol. 403, no. 4, pp. 1179–1186, 2012.
- [12] M. Y. Jo, Y. J. Ryu, J. H. Ko, and J.-S. Yoon, "Effects of compatibilizers on the mechanical properties of ABS/PLA composites," *Journal of Applied Polymer Science*, vol. 125, no. 2, pp. E231–E238, 2012.
- [13] V. Kumar, A. Dev, and A. P. Gupta, "Studies of poly(lactic acid) based calcium carbonate nanocomposites," *Composites Part B: Engineering*, vol. 56, pp. 184–188, 2014.
- [14] J.-H. Yang, Y. Shen, W.-D. He et al., "Synergistic effect of poly(ethylene glycol) and graphene oxides on the crystallization behavior of poly(L-lactide)," *Journal of Applied Polymer Science*, vol. 130, no. 5, pp. 3498–3508, 2013.
- [15] H.-M. Chen, X.-C. Du, A.-S. Yang et al., "Effect of graphene oxides on thermal degradation and crystallization behavior of poly(L-lactide)," *RSC Advances*, vol. 4, no. 7, pp. 3443–3456, 2014.
- [16] Y.-H. Cai, "Effects of barium sulfate on thermal behavior of poly(L-lactic acid)," *Asian Journal of Chemistry*, vol. 25, no. 4, pp. 2170–2172, 2013.